THE EFFECTS OF PARTICLE SHAPE, SIZE, AND INTERACTION ON COLLOIDAL GLASSES AND GELS

BY

RYAN C. KRAMB

DISSERTATION

Submitted in partial fulfillment of the requirements
for the degree of Doctor of Philosophy in Chemical Engineering
in the Graduate College of the
University of Illinois at Urbana-Champaign, 2010

Urbana, Illinois

Doctoral Committee:

Professor Charles F. Zukoski, Chair
Professor Kenneth S. Schweizer
Professor Jennifer A. Lewis
Assistant Professor Nathan D. Price

Abstract

Using multiple step seeded emulsion polymerization reactions, colloid particles of tunable shape are synthesized from polystyrene. In all, four particle shapes are studied referred to as spheres (S), heteronuclear dicolloids (hDC), symmetric homonuclear dicolloids (sDC), and tricolloids (TC). Two size ranges of particles are studied with approximate diameters in the range of 200-300nm and 1.1-1.3μm. The solvent ionic strength is varied from 10^{-3}M to 1M resulting in particle interaction potentials that range from repulsive to attractive. The effect of anisotropic shape is found to increase the glass transition volume fraction (ϕ_g) in good agreement with activated naïve Mode Coupling Theory (nMCT) calculations. Differences in ϕ_g and the linear elastic modulus (G_0') due to particle shape can be understood in terms of the Random Close Packed volume fraction (ϕ_{RCP}) for each shape; $\phi_{RCP}-\phi_g$ is a constant. In addition, a reentrant phase diagram is found for S and sDC particles with a maximum in the fluid state volume fraction found at weakly attractive interaction potential, in agreement well with theoretical calculations. Nonlinear rheology and yielding behavior of repulsive and attractive spheres and anisotropic particles are examined and understood in terms of barriers constraining motion. The barriers are due to interparticle bonds or cages constraining translational or rotational motion. Yield stress has similar volume fraction dependence as G_0' and a similar framework is used to understand differences due to particle shape and interaction. For larger particles, the effects of shape and interaction are studied with respect to dynamic yielding and shear thickening. The dynamic yield stress is found to increase with volume fraction while the stress at thickening is constant. The intersection of these indicates a possible jamming point below ϕ_{RCP}.

Dedicated to my son, Tobin

Acknowledgements

I would like to thank my advisor Prof. Charles F. Zukoski. He has been my main source of guidance throughout my graduate research experience. His tireless effort and devotion to his work is an inspiration.

I would like to acknowledge my family for all their encouragement. My parents supported my education through my bachelor's degree. Without them behind me, this would not be possible. My wife, Tiffany, has been the most important and influential person in my life for years and her support through nearly five years of graduate school has been vital. Tobin, my son, has brought an incredible amount of joy to my life and it is to him that I dedicate this work.

Thanks also goes to the Zukoski research group who make working in the lab an enjoyable experience. In addition, I would like to thank Kenneth Schweizer and Rui Zhang for helpful theoretical discussions and Jordan Taylor for assistance with particle synthesis.

This material is based upon work supported by the U.S. Department of Energy, Division of Materials Sciences under Award No. DE-FG02-07ER46471, through the Frederick Seitz Materials Research Laboratory at the University of Illinois at Urbana-Champaign. Research for this publication was carried out in part in the Frederick Seitz Materials Research Laboratory Central Facilities, University of Illinois, which are partially supported by the U.S. Department of Energy under grants DE-FG02-07ER46453 and DE-FG02-07ER46471.

Table of Contents

Chapter 1 Overview

1.1 Introduction

Colloidal suspensions represent a class of materials that offer a nearly unrivaled degree of customizability. It is this incredible variability found in colloid systems that make them so ubiquitous in natural systems, valuable in industrial products, and the subject of much research. In addition, experimental colloidal systems are invaluable as models for studying atomic systems.[1] This is because the space and time scales associated with these systems are more tractable than with particles of atomic size. At the same time, recent advances in tuning colloid particle shape and interaction, as discussed here, allow for closely matched analogous properties that provide insight into the behavior of atoms and molecules.

While colloids must by definition contain particles with at least one dimension in the size range of 1nm-1mm, nearly all other aspects of the system can be chosen to suit the application. For example, the materials that make up the colloid particles can be made from polymers (e.g. polystyrene and polymethyl methacralate) and ceramics (e.g. silica, and aluminia) as two of the most common sources, but also include such materials as blood cells, proteins, clays, ink and paint pigments, oil droplets, and surfactant micelles.[2] In addition to the particle materials, other examples of system variables that can be altered are the choice of solvent, the size of particles (to some extent), the interaction of the particles, and the particle shape. The continuous medium in which the particles are dispersed is most often water due to its availability and cost, but this is not always the liquid used. In many industrial applications a polymer melt is used to disperse colloid particles. This is known as a composite material where addition of particles

results in enhanced mechanical properties over the pure polymer. Other solvents are chosen for their mechanical properties (e.g. high or low viscosity), dielectric properties, hydrophobicity, as well as other considerations.

Often the choice of solvent is governed by the desire to tune the interaction between the particles. For example a solvent may be chosen where the index of refraction matches that of the particles which results in an elimination of van der Waals attractive forces so that other interactions can be studied. The different types of interactions commonly found in colloid research are 1) attractions caused by depletion resulting from the addition of a nonadsorbing polymer to the solvent, 2) attractions caused reducing the solvent quality for polymer molecules on the surface of the particles (e.g. lowering the temperature), 3) the previously mentioned van der Waals attractive forces, 4) electrostatic repulsive or attractive forces due to charges on the surface of the particles, 5) volume exclusion due to non interpenetrating particles and/or stabilizing surface molecules.

The simplest theoretical colloid system is one in which the particle shape is spherical and the interactions are only volume exclusion. Systems that fit this description are known as hard spheres and have been the subject of extensive research. The behavior of hard spheres has been well characterized after many decades of experimental, theoretical, and simulation work.[3-8] As the volume fraction, ϕ, of particles is increased, hard spheres undergo state changes. At elevated particle densities, long range diffusion can appear to cease when observed for manageable time scales. The states or phases where this occurs are referred to as arrested states. For hard spheres these included glasses, jammed or random close packed, and crystals. For attractive particles, another arrested state, a gel, is possible at lower particles densities.

If the size polydispersity of the hard spheres is below about 7%, the system can crystallize.[8] A separation of fluid and crystal phases begins at a volume fraction of 0.49 and by 0.55 the particles will have crystallized.[3] The volume fraction of a suspension of crystallized particles can be increased and the particles will remain ordered up to a volume fraction of 0.74, which is the mathematical maximum packing fraction for spheres, and form a face centered cubic (fcc) structure.[9]

If crystallization is avoided, for example by increasing polydispersity above 7% or by concentrating very quickly so that crystals do not have time to nucleate and grow, a nonequilibrium phase known as a glass can be formed. A glassy state for hard spheres is usually reported to begin at a volume fraction (ϕ_{glass}) of 0.58.[10] For this state, the structure of the particles remains disordered like that of a fluid, but the number density of particles has increased so that on observable time scales, particles behave as though they are trapped by the cage of neighboring particles around them. According to theories such as full Mode Coupling Theory and activated naïve Mode Coupling Theory, the ideal glass transition volume fraction is below 0.58. The onset of localization for MCT occurs at ~0.52,[11] while for nMCT activated dynamics appears at 0.43.[12]

MCT and activated nMCT, which will be discussed in later chapters as it applies to the experimental systems described in this thesis, rely on equilibrium structure factor information to predict dynamical behavior. The theories predict a crossover volume fraction, ϕ_c, where localization begins. This localization results from interactions with neighboring particles. The power of MCT lies in its ability to predict the location of the cross over volume fraction and the existence of two time scales in the glassy state – diffusion out of cages and diffusion within the cages of nearest neighbors. Originally it

was thought that above the glass transition predicted by MCT, all long range diffusive motion stopped. There is clear experimental evidence that this is not the case and activated nMCT was developed to account for these discrepancies. Activated nMCT relies on nMCT predictions of elastic modulus but predicts a dynamical potential that restricts particle motion. Long range diffusion and stress relaxation require diffusion over the entropic barrier produced by interactions with neighboring particles. The model predicts that the application of stress lowers the barrier to long range diffusion such that the hopping time is reduced with increasing stress. At a particular stress the barrier height is decreased to zero. This is called the absolute yield stress. MCT and nMCT predict that above the cross over volume fraction there will be a frequency range over which the material will look solid like $G'>G''$ in the linear elastic limit. As the volume fraction is raised G_0' increases and diverges at RCP. Activated nMCT predicts the decay in G' with increasing stress above the linear limit and predicts G' drops catastrophically at the absolute yield stress. This yield stress is predicted to diverge at RCP. Following activated nMCT, at the cross over volume fraction the suspension dynamics is weakly influenced by caging as the dynamical potential barrier is low. This indicates that the glass transition volume fraction is a kinetic measure of arrest such that the characteristic time to relax stress approaches the time scale of the measurement. As a result, while activated nMCT predicts glassy moduli at all volume fractions above ϕ_c, experimentally the glass transition will be observed as $\phi_c<\phi_{glass}<\phi_{RCP}$, although the specific value of ϕ_{glass} will depend on the instrumentation used and the measurement time scales.

Although difficult in practice, the disordered glass phase can be concentrated with removal of solvent or increased pressure just as the crystal phase can, until an upper limit

of ~0.64 is reached (ϕ_{RCP})[13]. This volume fraction limit is known as random close packing (RCP) or maximally random jammed (MRJ) and is most often seen in larger, granular particles which do not usually undergo a glass transition.[14] Granular states are made up of particles where thermal motion is absent. As a result, activated motion is absent and glassy dynamics is not seen. The differences between Brownian and non-Brownian suspensions become important in very dense states as ϕ_{glass} and ϕ_{RCP} are approached. ϕ_{RCP} is the highest volume fraction for a disordered state. Beyond this value, some crystallization and ordering is necessary.[15] A schematic state diagram indicating the approximate volume fraction of each of the four arrested states is shown in Figure 1.1. The diagram is adapted from the review paper of Zaccarelli.[1]

A different but related jammed state is often seen when dense suspensions are flowing. This is known as shear thickening and may seem contradictory since the solid like properties characteristic of a jammed state are only seen when stress is applied and the suspension is under flow. Understanding of the mechanism of shear thickening and the properties that influence shear thickening behavior have been areas of interest in colloid science for decades and research in this topic remains active today.[16-28] Some studies have shown that the onset of shear thickening is associated with an order-disorder phase transition,[24] but the most widely accepted current theory is that shear thickening is due to the formation of hydroclusters, transient concentration fluctuations that are driven and sustained by the flow field.[29] These clusters are formed when the hydrodynamic forces from shear overcome the stochastic Brownian forces. The result is seen macroscopically as a rise in viscosity. A different type of shear thickening occurs when force bearing chains of connected particles percolate across the rheometer gap.[30] This is

known as discontinuous shear thickening. Experimentally, as the stress applied to the sample is increased, the shear rate appears to remain constant. Another difference between continuous and discontinuous shear thickening is the normal force on the rheometer tool. Hydroclusters and continuous thickening produce negative first normal stress differences as the plates in the instrument are pulled together. In discontinuous thickening, there is a positive normal stress difference and the plates are pushed apart.[25]

Adding to the complexity to the discussions on shear thickening phenomena seen experimentally is the diversity in the nature of the rise in viscosity or the relationship between shear rate and applied shear stress. Many shear thickening fluids see a gradual rise in the slope of stress vs shear rate to values above one in the shear thickening region. The slope then becomes steeper as volume fraction is increased.[19] Here the thickening is continuous and smooth. Other systems undergo discontinuous shear thickening where the shear rate reaches a critical value and cannot go any higher.[22] On the stress vs shear rate plot, the data will become vertical at this critical value of shear rate. In most systems where discontinuous thickening occurs, it is seen only at the highest volume fractions and is preceded by continuous thickening at lower concentrations. Finally, in some cases when extremely high stresses can be applied, a system will oscillate between a jammed or thickened state and one where flow is possible through slip.[25] Dramatic increases in the measured viscosity of the system as well as increases in the normal force are observed under these conditions.

1.2 Delaying Arrest by Tuning Particle Interaction and Shape

In addition to the academic interests, there are numerous industrial products that can be classified as a suspension or dispersion at some point in their production. The formation of an arrested state in the production or processing of these products can be extremely detrimental and cause significant damage to the product itself as well as piping, instrumentation, and pumps. Because of this, understanding the causes of particle arrest and the system properties that influence it as well as the ability to make general guidelines for avoiding arrest is of great importance to many scientists and engineers. Previous work with glassy and shear thickening systems combined with recent advances in particle synthesis techniques have given confidence in the ability to design a system that delays the onset of arrested dynamics either under static conditions or under shear when compared to the standard model colloid system – hard spheres.

The literature on glassy dynamics of colloid suspensions indicates that through the tuning of particle interactions it is possible to achieve glass transition volume fractions above 0.58 for spheres.[31, 32] The maximum in ϕ_{glass} occurs under conditions that are weakly attractive and was demonstrated theoretically for hard core particles experiencing short range attractive potentials[32] and for experimentally with depletion induced interactions.[31] Nonmonotonic changes in the glass transition boundary with strength of attraction is referred to as reentrant state behavior. This means that moving from hard spheres to weak attractions initially increases ϕ_{glass}. However, further increases to attraction strength cause gelation and arrest at lower volume fractions. A small re-entrant-type indentation in the arrested dynamics curve of Figure 1.1 shows what this might look like in a colloid system. Based on the above work, one of the goals of this

project was to expand the experimental systems where reentrant phase behavior is seen to include attractions caused by the ubiquitous van der Waals force. A second system property that has been shown to influence the onset of arrest is the particle shape. The effect of changing the shape of granular particles on their packing was demonstrated by Donev and coworkers by pouring marbles and M&M's into a large round bottom flask. They found that the spherical marbles reached packing fractions of ~0.64, very close to the value for RCP discussed earlier. Spheroidal shaped M&M's on the other hand could be packed to ~0.68, significantly higher than for the marbles.[14] Other simulation and experimental studies have shown that the degree of anisotropy, typically described as an aspect ratio has a nonmonotonic effect on the packing of particles. Typically a maximum in the packing density is found at an aspect ratio of 1.4-1.6.[33, 34] However, being able to see the effect of shape on ϕ_{RCP} for a colloid system would require increasing the volume fraction above the glass transition, which is often difficult experimentally. The work suggests that modest deviations from spherical shape can delay particle arrest to higher volume fractions with implications that similar effects may be possible with smaller colloid particles.

Theoretical work from Yatsenko and Schweizer using activated naïve Mode Coupling Theory (nMCT) recently predicted that hard particles consisting of two fused spheres separated by a fraction of the sphere diameters have higher ideal glass transition volume fractions than isotropic spheres.[35, 36] Their studies are in agreement with previous studies of Goetz and coworkers who predict similar properties.[37] Yatsenko and Schweizer predict that a suspension of particles with a length to sphere diameter ratio of ~1.4 have the highest ϕ_{glass}. L/D ratios higher than this reversed the trend in ϕ_{glass}, and by

L/*D*~2 the glass transition volume fraction was approximately that of the spheres. Both the experimental work by Donev et al and the theoretical work by Yatsenko and Schweizer demonstrate that arrest can be delayed by changing particle shape, and also give some indication that the glass transition and RCP may be linked in some way as both values are affected in a qualitatively similar way by changes in particle shape.

By taking what was learned about of how changes to particle interaction and shape influence the behavior of dense suspensions and the onset of particle arrest, this the work described in this thesis was designed to simultaneously study both effects in the same system. Questions such as – 'will weakly attractive, moderately nonspherical particles maintain fluid-like properties at densities higher than a system with only one of those characteristics?' are answered. In addition, the project seeks to find how two differeniate between particle arrest through vitrification and through random close packing and to draw conclusions about how these phenomena are related. Finally, the influence of particle interaction and shape on arrest during flow, i.e. shear thickening, are studied.

This thesis describes the experimentally work performed to answer these questions. In Chapter 2 there is a discussion on the synthesis techniques implemented for creating the particles used in the project as well as a summary of how the particles are characterized and prepared for experiments. The location of ϕ_{glass} and the elasticity of glassy suspensions containing four particle shapes under conditions that are effectively hard are discussed in Chapter 3. In addition experiments are compared to theoretical predictions using nMCT. Chapter 4 discusses the re-entrant phase diagram found for spheres and dicolloid particles and the effects of interparticle attractions due to truncated

van der Waals forces. In Chapter 5, the effects of particle shape on the yielding and flow behavior of hard particles is discussed, while in Chapter 6 the effects of varying the particle interaction are included. Yielding and shear thickening of larger sphere and dicolloid particles is described in Chapter 7, and a summary is given in Chapter 8.

1.3 Figures

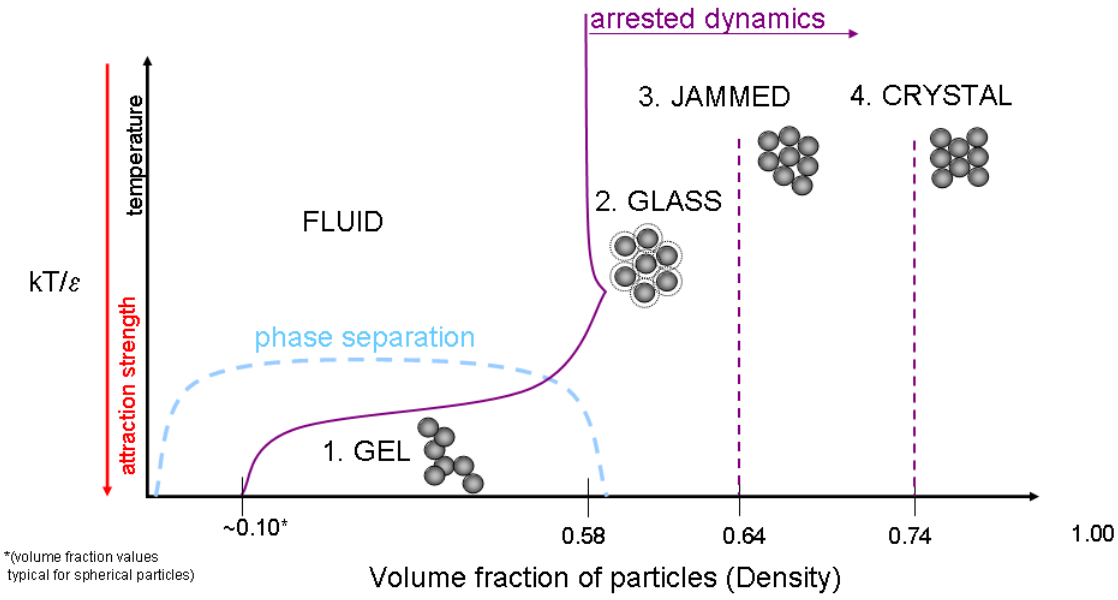

Figure 1.1. Schematic phase diagram showing common arrested states and the typical experimentally-observed volume fraction where they are occur. Increasing particle interaction is shown as going down on the y-axis as in the original diagram from Zaccarelli.[1]

1.4 List of References

[1] Zaccarelli, E., *J. Phys: Condens. Matter*, **2007**, 19, 323101.
[2] Lewis, J.A., *J. Amer. Ceram. Soc*, **2000**, 83, 2341.
[3] Bryant, G., S.R. Williams, L. Qian, I.K. Snook, E. Perez, and F. Pincet, *Phys. Rev. E*, **2002**, 66(6), 060501.
[4] Gopalakrishnan, V. and C.F. Zukoski, *Ind. Eng. Chem. Res.*, **2006**, 45(21), 6906.
[5] Rintoul, M.D. and S. Torquato, *J. Chem. Phy.*, **1996**, 105(20), 9258.
[6] van Blaaderen, A. and P. Wiltzius, *Science*, **1995**, 270.
[7] van Megen, W. and S.M. Underwood, *Phys. Rev.*, **1994**, 49(5), 4206.
[8] Sciortino, F. and P. Tartaglia, *Advances in Physics*, **2005**, 54(6), 471.
[9] Russel, W.B., D.A. Saville, and W.R. Schowalter, *Colloidal Dispersions*. 1989, Cambridge, UK: Cambridge Universtiy Press.
[10] Pusey, P.N. and W. van Megen, *Nature*, **1986**, 320.
[11] Bengtzelius, U., W. Gotze, and A. Sjolander, *J. Phys. C: Solid State Physics*, **1984**, 17(33), 5915.
[12] Schweizer, K.S. and E.J. Saltzman, *J. Chem. Phys.*, **2003**, 119(2), 1181.
[13] Torquato, S., T.M. Truskett, and P.G. Debenedetti, *Phys. Rev. Lett.*, **2000**, 84(10), 2064.
[14] Donev, A., I. Cisse, D. Sachs, E.A. Variano, F.H. Stillinger, R. Connelly, S. Torquato, and P.M. Chaikin, *Science*, **2004**, 303(5660), 990.
[15] Scott, G.D. and D.M. Kilgour, *J. Phys. D.: Appl. Phys.*, **1969**, 2(6), 863.
[16] Barnes, H.A., *J. of Rheol.,* **1989**, 33(2), 329-366.
[17] Bender, J.W. and N.J. Wagner, *Journal of Colloid and Interfacial Science*, **1995**, 172, 171.
[18] Bender, J.W. and N.J. Wagner, *J. Rheol.*, **1996**, 40(5), 899.
[19] Brown, E. and H.M. Jaeger, *Phys. Rev. Lett*, **2009**, 103, 086001.
[20] Chow, M.K. and Z.C. F., *J. Rheol.*, **1994**, 39(1), 15-32.
[21] Chow, M.K. and C.F. Zukoski, *J. Rheol.*, **1995**, 39(1), 33.
[22] Egres, R.G. and N.J. Wagner, *J. Rheol.*, **2005**, 49(3), 719.
[23] Fagan, M.E. and C.F. Zukoski, *J. Rheol.*, **1997**, 41(2), 373.
[24] Hoffman, R.L., *Journal of Rheology*, **1998**, 42(1), 111.
[25] Larsen, R.J., J.-W. Kim, C.F. Zukoski, and D.A. Weitz, *Phys. Rev. E*, **2010**, 81, 011502.
[26] Lee, Y.S. and N.J. Wagner, *Rheol. Acta.*, **2003**, 42, 199.
[27] Maranzano, B.J. and N.J. Wagner, *J. Chem. Phys.*, **2001**, 114(23), 10514.
[28] Maranzano, B.J. and N.J. Wagner, *J. Rheol.*, **2001**, 45(5), 1205.
[29] Wagner, N.J. and J.F. Brady, *Physics Today*, **2009**.
[30] Holmes, C.B., M.E. Cates, M. Fuchs, and P. Sollich, *J. of Rheol.*, **2005**, 49(1), 237.
[31] Pham, K.N., A.M. Puertas, J. Bergenholtz, S.U. Egelhaaf, A. Moussaid, P.N. Pusey, A.B. Schofield, M.E. Cates, M. Fuchs, and W.C.K. Poon, *Science*, **2002**, 296(5565), 104.
[32] Bergenholtz, J. and M. Fuchs, *Phys. Rev. E*, **1999**, 59(5), 5706.
[33] Sherwood, J.D., *J. Phys. A: Mathematical and General*, **1997**, 30(24), L839.

[34] Sacanna, S., L. Rossi, A. Wouterse, and A.P. Philipse, *J. of Phys.: Cond. Matt.* **2007**, 19(37), 376108.
[35] Yatsenko, G. and K.S. Schweizer, *J. Chem. Phys.*, **2007**, 126.
[36] Yatsenko, G. and K.S. Schweizer, *Phys. Rev. E*, **2007**, 76, 014505.
[37] Götze, W., *J. Phys.: Cond. Matt.*, **1999**, 11.

Chapter 2 Particle Synthesis and System Characterization

2.1 Introduction

Synthesis techniques that create polystyrene particles offer a wide range of particle sizes in the colloidal scale going from about 10nm to a few microns in diameter.[1-3] For the studies discussed here, two recipes were selected that result in spherical seed particles that are ~200-250nm[4] and 800nm-1μm[5] in which emulsion polymerization is utilized. This process uses a free radical source to initiate the polymerization of a monomer in a non-soluble solvent. For these reactions, the styrene monomer and water (small particles) or water/methanol (large particles) are mixed and potassium persulfate is used to initiate the polymerization in both cases.

For the smaller particles the synthesis takes place in the presence of a surfactant, sodium dodecyl sulfate (SDS), which acts to stabilize the growing polymer droplets suspended in the water. Using SDS in the reaction vessel creates particles that are smaller than if no surfactant is used in the synthesis. The surface tension between water and the hydrophobic polymer particles is lowered by adsorbing surfactant to the particle surface. Because of this, smaller droplets are able to remain separate and avoid combining into larger droplets despite a larger surface area to volume ratio. In the recipe for ~900nm particles, surfactant-free emulsion polymerization is used. With no surfactant on the droplet surface, small droplets combine to form more stable larger sizes. However, changing only the presence of SDS in the reaction results in particles that are approximately a factor of 2-3 larger than the smaller particles used here.[6] Because a larger size difference was needed to observe significant changes in material properties, a second variation in the recipes was needed to further increase in particle diameter. This

second alteration to the small particle recipe is to use methanol in addition to water as the solvent. Methanol is miscible in both water and styrene and therefore increases the stable droplet size and allows for final particles near 1μm in diameter.

The seed particles were then used in second emulsion polymerization reaction in which they are swelled with additional styrene monomer. The added styrene is then also polymerized and depending on the crosslinking density in the seed particle, results in shapes ranging from a single sphere to multiple fused spheres with length to diameter (*L/D*) ratios of up to 1.6. The work by Mock et al. shown in Figure 2.1 demonstrates some of the possible shapes possible using this two step emulsion polymerization technique.[4] In addition, Figure 2.2 shows a schematic diagram of the swelling and lobe formation process for a dicolloid paricle.

Because the swelling and polymerization steps can potentially be repeated indefinitely, it may be possible to create particles with more than two lobes. This would require crosslinking each new lobe with DVB, and was attempted using multiple combinations of crosslinking densities in the seed and lobe parts of dicolloid particles. One such successful reaction was performed creating a three lobed tricolloid particle that will be discussed in detail in the following sections.

For the particles used in this study, the following shapes were synthesized. Small particles: spheres (S) (*L/D* = 1), heteronuclear dicolloids (hDC) (*L/D* = 1.1), symmetric homonuclear dicolloids (sDC) (*L/D* = 1.3), and tricolloids (TC). Large particles: spheres, and symmetric homodicolloids (*L/D* = 1.17). The specific reaction conditions that lead to each shape will be discussed in the Section 2.2. Particle size and shape characterization will be discussed in Section 2.3, while a discussion of the technique used to concentrate

the particles, coat them with a stabilizing surfactant layer, and vary the particle interaction through changing the solvent ionic strength will be discussed in Sections 2.4 and 2.5

2.2 Particle Synthesis

The first step in creating the series of spherical and nonspherical small particles is to synthesize ~210nm spherical seed particles. These seed particles were synthesized in a 5L round-bottom flask immersed in a constant temperature water bath. A poly-tetraflouroethylene coated blade attached to a rotating glass bar was used for stirring. Initially 3.75g of SDS (Bio-Rad, electrophoresis purity reagent grade) was dissolved in 3000mL of deionized water. The water was allowed to reach a steady state temperature of 80°C and 350mL of styrene monomer (Sigma-Aldrich, 99% purity grade) was added. For the dicolloid seeds, the DVB was dissolved into the styrene added in this step. The function of DVB is to crosslink the growing polystyrene chains during the polymerization reaction which is necessary for the separation and lobe formation in the subsequent step. The solution was stirred at 80°C for one hour at a vigorous speed. 11.7g of potassium persulfate initiator (Fisher Scientific 99.5% purity grade) dissolved in 560mL of water was then added, and the reaction was allowed to proceed for 24 hours. The resulting seed particles were nearly identical: 210nm in diameter (± 3.2nm) for the S seeds, 211nm (± 1.5nm) for the hDC, sDC, and TC seeds.

The swelling and second polymerization reactions are identical for both the S and sDC particles, with the difference in final particle shape determined by the presence of DVB in the seed particles. Here, 880mL of the seed particle solution was poured into a

5L round bottom flask along with 620mL of a 0.1M potassium hydroxide (KOH) solution, 2.5g of SDS, and 2.4g of azobisisobutyronitrile (AIBN) dissolved in 130mL of new styrene. The flask was stirred at room temperature for 24 hours. When the swelling was complete, 5mL of methacrylic acid and 40g of hydroquinone dissolved in 500mL of the KOH solution were added to the vessel and the temperature was elevated to 70°C. The reaction proceeded for 24 hours. The final reaction consisted of ~2000mL of particles at approximately 7% by volume.

The hDC particles were created by under-swelling the 2% DVB seed particles with styrene. Under-welling of the seed particle results in a daughter lobe that is slightly smaller than the original seed, and the effect is a nonsymmetrical particle shape. Instead of using 130mL of monomer in the swelling step, 80mL was used. This also necessitated a decrease of the amount of SDS to 1.54g, AIBN to 1.48g, methacrylic acid to 3.07g, and hydroquinone to 24.6g. All other reaction conditions and times were identical. The reaction produced ~2000mL of hDC particles at 7% by volume.

The TC particles were synthesized in a smaller 500mL flask. This reaction used a batch of sDC in which the daughter lobe was also crosslinked with 2% DVB. Because the polymerization of daughter lobe is initiated with AIBN and not potassium persulfate, the surface of this lobe is more hydrophobic than the seed particle surface. This requires that either acrylic acid or vinyl acetate be added to the surface of the sDC seed particles prior to the third swelling/reaction step. The method described by Mock et al. was used to incorporate vinyl acetate to the surface of the particles[4] and then the swelling and polymerization reaction was carried out using 10% of the quantities of reactants used in the S and sDC synthesis. The result was ~200mL of ~7% TC particles.

2.3 Particle Size and Degree of Anisotropy

The size and shape of the particles was determined with the use of a scanning electron microscope (SEM Hitachi S4700). After cooling of the synthesis reaction vessel to room temperature a single drop of sample was placed on a copper sample grid (SPI supplies, Formvar coated). Images were taken at 30,000 – 50,000X magnification. And ImageJ software was used to measure ~100 representative particles to obtain the average particle diameters and lengths of other dimensions. The spheres had a mean diameter of 270nm (±1.6nm) while the dicolloids had a mean long axis length of 330nm (±2.2nm) and a mean short axis length of 250nm (±2.1nm) as measured by scanning electron microscopy (SEM Hitachi S4700). The aspect ratio of the dicolloids, length divided by sphere diameter, is L/D = 1.3. The hDC particles were measured to have a large lobe diameter of 241 (±15nm), with the smaller lobe ~0.8 that of the larger and a long axis length of 273 (±9nm). The TC particles contain three similar spheres fused in a triangular shape. The diameter of these overlapping spheres is 300 (±25nm) with a separation bond length (l_b) of 0.45D. Figure 2.2 shows an example of the SEM images taken for each particle shape for the small particles, while Figure 2.3 shows the large particles.

Accuracy of the SEM measurements was confirmed by dynamic light scattering using a Brookhaven Instruments fiber optic quasi-elastic light scattering (FOQELS) device. The FOQELS device uses a 20mW HeN laser to create a beam of 638.2nm wavelength light. The software calculates particle sizes in dilute (<1% by volume) solutions by measuring the intensity of light scattered off the particles and fitting the correlation function to theoretical values for spheres of a particular size.

2.4 Concentrating using Dialysis and Addition of Nonionic Surfactant ($C_{12}E_6$) to Particle Surface

After synthesis the particles are dialyzed against a polyethylene glycol (20,000 molecular weight, Sigma) in deionized water solution with approximately 30g-50g of PEG and 3L of water to remove unwanted electrolytes, hydroquinone, and oligomers. The dialysis process also concentrates the particles by drawing water out from the dialysis tubes. Once the volume fraction of particles in the tube reached approximately 0.35-0.40, 15-25mL portions of the solution were transferred to a 50mL centrifuge tube containing 0.338g of a nonionic surfactant, hexaethylene monododecyl ether ($C_{12}E_6$) (Sigma). This molecule was chosen based on the work of Partridge[2] to stabilize the particles and truncate the van der Waals attraction. The length of this molecule, and therefore half the distance of closest particle separation at full coverage, was found to be ~4nm by Partridge and can be seen in the schematic drawing of this molecule in Figure 2.3. The $C_{12}E_6$ critical micelle concentration in water is approximately 8 x 10^{-5}M.[2, 7, 8] The structure of the surfactant molecule is shown in Figure 2.2. This layer sets the minimum surface-to-surface separation where the van der Waals forces from the polystyrene cores are operative to be ~8nm. Finally, a bulk solution of either 0.01, 0.05, 0.1, 0.5, 1.0, or 5.0M sodium chloride (Fischer Scientific, crystalline) dissolved in deionized water was added such that the final concentration of $C_{12}E_6$ was 0.03M, the ionic strength of the solution varied from 0.001M to 1.0M and the total volume in the tube was 25mL. The tubes were then centrifuged at 6000rpm (small particles) or 2000rpm (large particles) for one hour intervals and the supernatant removed until further centrifuge cycles produced no removable supernatant. The g-forces achieved in the

centrifuge are approximately 4000g and 1333g depending on the size of the particles and rotational speed. The volume fraction of particles at this stage ranged from 0.55 – 0.65 and became the bulk particle solution to be diluted for rheological experiments.

2.5 Characterizing Surface Potential and Tuning Interaction through Ionic Strength

The surface charge of the particles in the presence of surfactant was measured by the zeta potential (Brookhaven Instruments Phase Analysis Light Scattering) at the edge of the surfactant monolayer for the small and large particles, as seen in Table 2.1. Since $a\kappa>100$, the Smoluchoski theory equation is used to convert electrophoretic mobility to zeta potential.

As mentioned in Chapter 1, the van der Waals attractive force remains constant for each particle size as this is determined with the Hammaker coefficient of the particle in solvent, the diameter of the particles, and the distance of separation. The equation of calculating the contribution of the van der Waals force to the total particle interaction potential was given in Equation 1.1. The contribution of the electrostatic repulsive forces to the total potential is a function of the solvent ionic strength and this can be found in Equation 1.2. At low ionic strengths the repulsive forces dominate over the van der Waals forces resulting in an interaction potential that is repulsive at all separation distances. For the small particles, a completely repulsive total potential is found for ionic strengths below ~10^{-2}M. For large particles this occurs at ionic strengths below ~10^{-3}M. At the other extreme, high ionic strengths screen the electrostatic charge of the particles to the point that the total potential has a deep attractive minimum near the surface of the

surfactant layer. For small particles, at ionic strengths above ~0.5M, the van der Waals attractions dominate the potential at all distances and cause an attractive minimum of ~$3k_BT$ to be seen. The large particles have a deeper attractive minimum at high ionic strengths due to the increase in size. Here, attraction strengths >$10k_BT$ are found at 0.5M. Even at slightly lower ionic strengths, strongly attractive local minimums are found despite their location away from the surfactant surface. For example at 0.1M a minimum of ~$5k_BT$ is seen at a distance of ~5nm beyond the surfactant layer. At intermediate ionic strengths, (0.03-0.3M for small particles, 0.003-0.01M for large particles) the total potential ranges from one that can be described as effectively hard with a small increase in particle diameter to account for the separation distance where the repulsive total potential has dropped to a negligible value (typically $1k_BT$) to one that has a weak local attractive minimum of <$5k_BT$. It is in this intermediate range that most of the work described here was performed. Figures 2.4 and 2.5 show calculations for the total interaction potential at various ionic strengths for the small and large particles respectively.

2.6 Figures and Tables

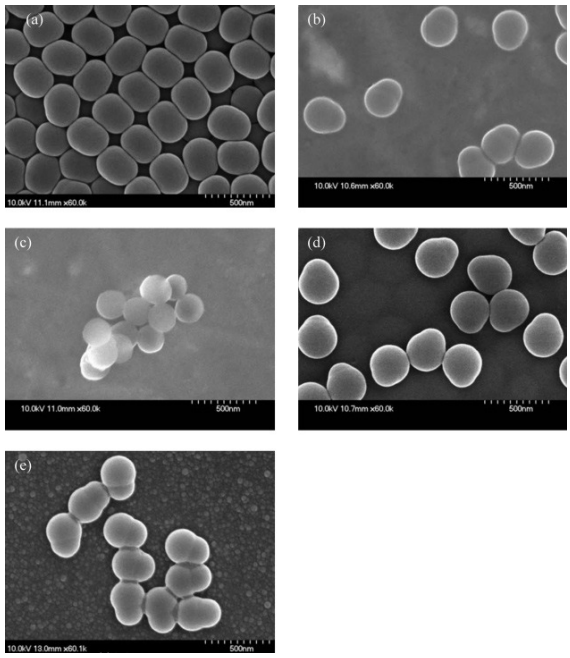

Figure 2.1. Potential particle shapes made using multiple step emulsion polymerization from Mock et al.[4]

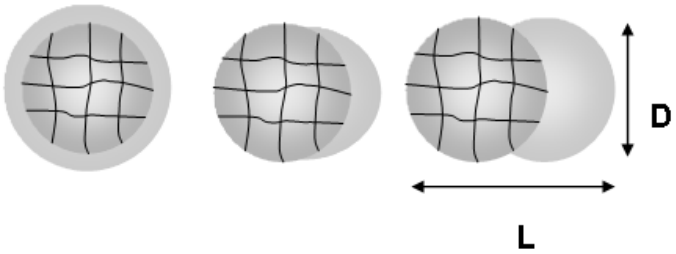

Figure 2.2. Schematic diagram of the process of swelling a crosslinked seed particles (first image), phase separation during polymerization (second image), and final symmetric dicolloid particle (third image).

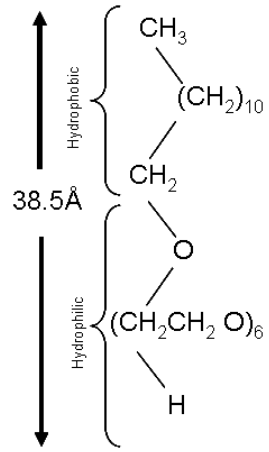

Figure 2.3. Chemical structure of the surfactant molecule $C_{12}E_6$. The length of the molecule determines the distance of closest separation and therefore the truncation distance for van der Waals force calculations for fully covered particles.

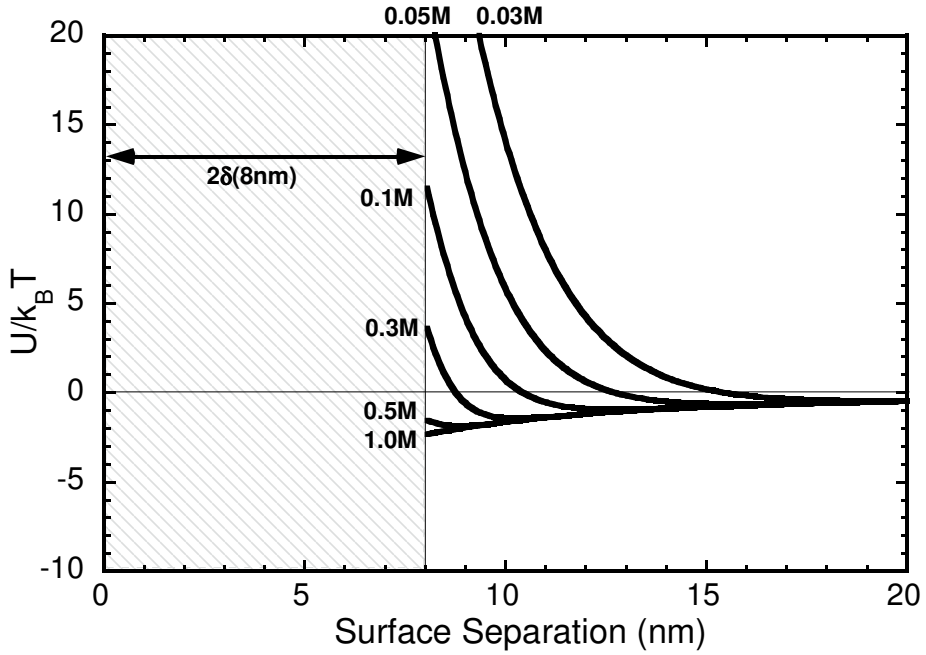

Figure 2.4. Calculation of the total interparticle potential energy for the small particles used in this work at ionic strengths of 0.03, 0.05, 0.1, 0.3, 0.5 and 1.0M

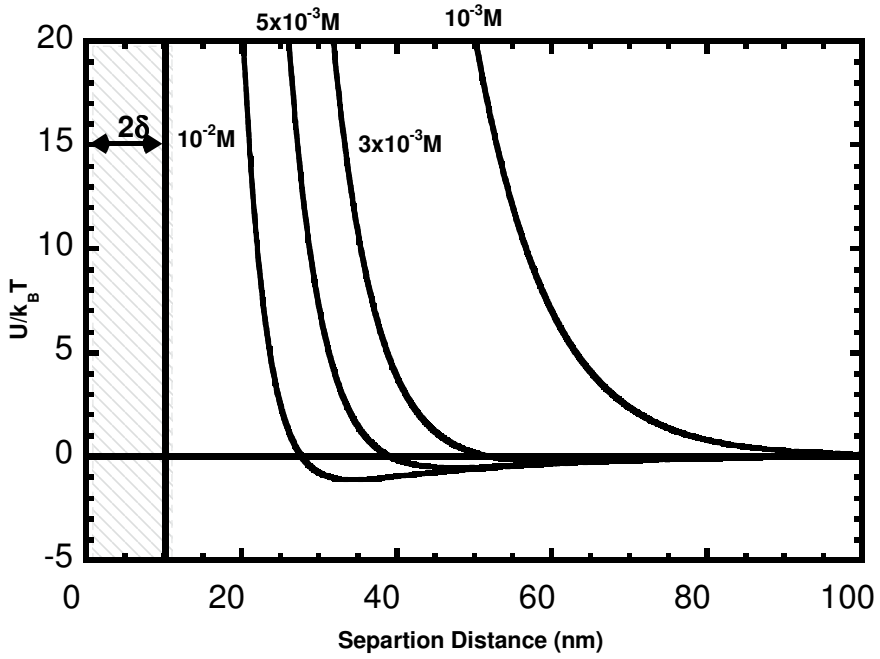

Figure 2.5. Calculation of the total interparticle potential energy for the large particles used in this work at ionic strengths of 10^{-3}, $3x10^{-3}$, $5x10^{-3}$, 10^{-2}M.

Table 2.1. Surface Potential Measurements

Small Particles D~270nm			
Ionic Strength (M)	Zeta Potential Measurements (mV)	Uncertainty	κD
0.03	-20.6	±1.6	156
0.05	-15.9	1.6	201
0.1	-11.8	10.5	285
0.3	-8.7	31.7	493
0.5	-2.7	4.4	636
Large Particles D~1200nm			
0.001	-68.8	±3.4	126
0.003	-41.6	4.0	219
0.005	-	-	283
0.01	-45	15	400
0.03	-27.4	9.0	693
0.05	-42.2	20	894
0.1	-15.0	2.2	1265

Table 2.1. Surface (zeta) potential of small and large particles at various ionic strengths.

2.7 List of References

[1] Goodwin, J.W., J. Hearn, C.C. Ho, and R.H. Ottewill, *Colloid and Polymer Sci.*, **1974**, 252, 464.

[2] Partridge, S.J., *Rheology of Cohesive Sediments*, in *Dept. of Physical Chemistry*. 1985, Bristol University.

[3] Hawkett, B., D. Napper, and R. Gilbert, *J. Chem. Soc. Faraday Trans. 1*, **1980**, 76, 1323.

[4] Mock, E.B., H. De Bruyn, B. Hawkett, R. Gilbert, and C. Zukoski, *Langmuir*, **2006**, 22.

[5] Homola, A.M., M. Inoue, and A.A. Robertson, *J. App. Polymer Sci.*, **1975**, 19, 3077-3086.

[6] Kramb, R.C. and C.F. Zukoski, *Langmuir*, **2008**, 24(14), 7565–7572.

[7] Corkhill, J.M., J.F. Goodman, and S.P. Harrold, *Trans. Faraday Soc.*, **1964**, 60, 202.

[8] Hough, D.B. 1973, Bristol University.

Chapter 3 Glass Formation and Shear Elasticity in Dense Suspensions of Hard Anisotropic Particles

3.1 Introduction

Colloid science has historically been based on spherical particles that interact via diverse attractive and repulsive forces.[1] Recently, the field has begun to undergo a paradigm shift towards nonspherical and/or chemically heterogeneous (e.g., Janus) particles of modest shape anisotropy.[2-4] These more complex objects hold great promise as a new class of soft materials based on "molecular colloids" that can self-assemble into unique structures and form kinetically arrested glasses or gels of tunable viscoelasticity. A qualitatively new feature is the effect of particle orientation on packing and coupled translation-rotation dynamics.

Both ideal mode coupling theory (MCT)[5-11] and computer simulations[12, 13] find shape anisotropy deeply modifies the onset of glass formation. For uniaxial hard objects, a remarkable non-monotonic variation with aspect ratio of the kinetic arrest volume fraction is predicted.[5, 8, 9, 14] For symmetric dicolloids composed of two overlapping hard spheres (diameter D) separated by a bond length l_b, the kinetic arrest volume fraction is predicted to exhibit a "maximally fluidic" state when the aspect ratio $L/D=1+(l_b/D)\sim1.4$.[5, 8] Intriguingly, a similar non-monotonic variation of the jamming volume fraction of granular ellipsoids and spherocylinders has been discovered in simulations and experiments.[15, 16] MCT predicts the glassy shear modulus of hard dicolloids depends strongly on particle shape, but an underlying universality of the volume fraction dependence exists based on the dynamic crossover volume fraction, ϕ_c.[5, 14]

Despite the significant theoretical progress, quantitative and systematic experiments that probe the slow dynamics of dense Brownian suspensions of nonspherical colloids are largely nonexistent. This chapter presents the first detailed measurements of kinetic arrest and elasticity in suspensions of tunably repulsive nonspherical colloids, and compares the results with their chemically identical spherical analogs. Much prior work has been performed on the latter systems, especially model hard sphere suspensions. Many, but not all, ensemble-averaged aspects of hard sphere glassy dynamics are well described by ideal MCT based on the confining cage concept and continuous cooperative motions.[7, 17, 18] However, confocal microscopy[19] and simulations[20, 21] find particle trajectories display intermittent large amplitude hopping events. Very recent experiments[22] have established the dominance of activated dynamics well below random close packing (RCP). Such phenomena are not captured by ideal MCT, but are accurately described by the nonlinear Langevin equation theory (NLE) as a consequence of barrier hopping.[23, 24] How particle shape affects the rare activated hopping process is of broad interest.

3.2 Experimental

Experimental systems have been designed to directly test recent theoretical predictions that address four issues: (i) the role of aspect ratio and higher order shape anisotropy on the *kinetic* arrest volume fraction, ϕ_g, (ii) the magnitude and volume fraction dependence of the shear modulus as a function of particle shape, (iii) possible universality of the elastic response, and (iv) possible connection between the dynamic crossover and RCP volume fractions, ϕ_c and ϕ_{RCP}.

Surfactant-based emulsion polymerization methods[25-27] are employed to create four particle shapes: sphere (S) with D~270 ±4nm, symmetric homonuclear dicolloid (sDC) of aspect ratio ~1.3 with D~250 ±5nm, heteronuclear dicolloid (hDC) of aspect ratio ~1.1 and sphere diameter ratio ~1.2, and a tricolloid (TC) composed of three equal size overlapping spheres of dimensions D~300 ±25nm with l_b~0.45. The synthesis approach of ref. [25] was employed in which crosslinked polystyrene seed particles (D~211 ±3nm) are swollen with additional styrene monomer, and the added styrene polymerized. Phase separation results in the formation of nonspherical particles closely described as overlapping spheres. By controlling the seed particle crosslinking density and ratio of styrene added in each step, one can achieve various degrees of overlap with the mother and daughter particles as seen in panels (a-c) of the inset of Figure 3.1. With proper manipulation of the surface properties after each step, a tricolloid shape has been synthesized via a three-step reaction as shown in panel (d). In characterizing these particles a characteristic single colloid volume parameter V^* is defined as: D^3 (S), D^2L (hDC), DL^2 (sDC), and Dbh (TC) where b and h are the base and height of a triangle inscribing the particle.

The physical behavior of suspensions of different shapes is compared at constant chemistry. Interparticle interactions were rendered repulsive and short range by stabilizing particles with a monolayer of the nonionic surfactant $C_{12}E_6$ in an aqueous salt solution at ionic strengths of [I]=0.03M, 0.05M and 0.1M. Classic DVLO calculations were performed using a Hamaker constant of $3.1k_BT$ with a minimum separation distance of the polystyrene surfaces of 8nm (which is twice the thickness of the $C_{12}E_6$ surfactant, 2δ) and electrophoretically-derived electrostatic surface potentials.[26, 27] The resulting

sphere-sphere interparticle potentials are shown in Figure 3.1. An effective hard diameter (and corresponding effective volume fraction where accounting for short range Coulomb repulsions allows the definition of an effective hard core volume fraction: $\phi_{eff}=\phi(V^*_{eff}/V^*)$, where V^*_{eff} is: $(D_{eff})^3$, $D_{eff}^2 L_{eff}$, $D_{eff}L_{eff}^2$ and $D_{eff}b_{eff}h_{eff}$, where $D_{eff}=D+\Delta$, $L_{eff}=L+\Delta$, $b_{\text{eff}}=b+\Delta$ and $h_{eff}=h+\Delta$, for spheres, heteronuclear dicolloids, homonuclear dicolloids, and tricolloids, respectively) is estimated as the distance at which the repulsion is $1k_BT$. The total increase in particle diameter from the combined effects of surfactant and electrostatic repulsive separation are Δ~14.00nm at 0.03M, 11.55nm at 0.05M, and 9.85nm at 0.1M.

Oscillatory shear mechanical measurements were employed to determine the frequency-dependent elastic (G') and viscous (G'') moduli in the linear response regime. In the generalized Maxwell model spirit, a relaxation time, τ, is defined as when $G'=G''$, which is well known to correlate closely with other measures of glassy relaxation such as the single particle or collective density fluctuation relaxation time on the local confining cage length. As illustrated in the inset of Figure 3.2, a kinetic arrest volume fraction, ϕ_g, is determined based on data at 1 Hz, corresponding to a vitrification criterion of $\tau(\phi_g) \equiv 2\pi$ s. The experimental uncertainty for volume fraction reported in Figure 3.2 (and all other figures and the table) is ±0.005.

3.3 Results and Discussion

Table 3.1 presents the kinetic glass volume fractions of the four particle shapes at several ionic strengths. For the most repulsive system ([I]=0.03M), ϕ_g increases from 0.475 for the sphere to 0.606 for the tricolloid, with the homonuclear and heteronuclear

dicolloids in between. Hence, a remarkably large delay of kinetic vitrification and emergence of elasticity occurs upon introducing shape anisotropy, qualitatively consistent with theory [5,8]. For fixed particle shape, ϕ_g generally increases with ionic strength. This trend is partially, but not fully, understandable as a decreasing effective particle diameter as Coulomb repulsion is more screened. More importantly, ionic strength is a secondary variable that does not modify the overall consequences of nonspherical particle shape. The main panel of Figure 3.2 shows the corresponding elastic moduli as a function of volume fraction at fixed [I]=0.03M. The raw data directly demonstrates that the onset of kinetic vitrification is strongly particle shape dependent and *G'* grows as roughly an exponential function of volume fraction. Moreover, the slopes are not very sensitive to particle shape, a feature that (as discussed below) suggests the construction of a master curve is possible.

How can one understand these experimental observations? The only theoretical approach to date that has addressed dicolloid and tricolloid shapes, non-hard-core repulsions, and shear elasticity is the center-of-mass (CM) version of naïve Mode Coupling Theory (CM-nMCT) and barrier hopping NLE theory.[5, 14] The equations to determine the ideal mode coupling transition at ϕ_c (dynamic crossover), mean barrier hopping time, τ, and shear modulus are given in the literature.[5, 14] The site-site RISM integral equation theory with the Percus-Yevick closure is employed to compute the required equilibrium correlation functions.[28] Calculations for both the hard core potential and the specific soft repulsions in Figure 3.1 have been performed. The Brownian "short time" scale, τ_s, is required to compute absolute relaxation times, and is determined from knowledge of the primary particle size, solvent viscosity, and (near)

contact value of the interparticle $g(r)$.[5, 23, 24] For all systems the estimate τ_s~0.1 s is employed; quantitative uncertainty in this value has very little consequences since it enters as a prefactor in the activated relaxation time.

CM-nMCT calculations yield ϕ_c=0.432, 0.474, and 0.508 for the hard core sphere, homonuclear dicolloid, and tricolloid, respectively. This ordering agrees with the experimental *kinetically-defined* glass transition volume fractions, but the absolute magnitudes are significantly smaller. The latter is expected since ϕ_c denotes only a dynamic crossover to activated hopping controlled motion.[23, 24]. Table 1 presents the theoretical kinetic arrest volume fractions, ϕ_g. Good *a priori* (no fitting) agreement with experiment is obtained for both the shape and ionic strength dependence trends; quantitatively, the theory overpredicts ϕ_g. Although ideal MCT describes a dynamic crossover, the physics that determines it is closely correlated with the barrier heights and hopping controlled transport, as previously emphasized.[5, 14, 23, 24]

Is there an underlying universal behavior of the elastic modulus data in Figure 3.2? Prior theoretical work[5, 14] for hard core dicolloids suggests the answer is yes if the shear modulus is nondimensionalized by the particle volume V^* defined above, and a reduced volume fraction variable is introduced which quantifies the distance from the ideal MCT dynamic crossover, (ϕ/ϕ_c)-1. Theoretical calculations are re-plotted in this doubly reduced fashion in Figure 3.3, and an excellent collapse is obtained. Performing the same re-plotting exercise for the experimental data (all shapes, several ionic strengths where the effective hard particle volumes are used to scale the modulus and volume fraction) also results in a remarkably good collapse as seen in the main frame of Figure 3.3. Note that the ϕ_c used is determined from the CM-nMCT theory. Hence, the

suggestion[5, 14] that the relevant fundamental stress level involves the single particle volume, and the relevant volume fraction is the distance from the ideal MCT crossover, is well confirmed. The quantitative differences between the slope of the theory and experiment curves is not understood, and may reflect inadequacies of the RISM structural input to the dynamical theory at very high concentrations.

The approach to jamming is now considered. For hard spheres, it has been analytically shown that the NLE theory predicts[29] $G' \propto g^2(D) \propto (\phi_{RCP} - \phi)^{-4}$ as RCP is approached. This motivates a double logarithmic plot of the experimental modulus data versus $(\phi_{RCP} - \phi)^{-1}$. The inset of Figure 3.3 presents results for all particle shapes, including the hard sphere data of ref. [30] for which ϕ_{RCP}=0.66 a value also adopted here. The RCP volume fraction of nonspherical particles was adjusted to achieve maximum data collapse with the result: ϕ_{RCP}=0.70 (hDC), 0.72 (sDC), and 0.74 (TC). The increase of ϕ_{RCP} with particle asymmetry is physically reasonable. Figure 3.3 shows an excellent data collapse can be obtained, and the effective slope of the logarithmic plot is well described by the theoretical prediction as shown by the dashed line.

Finally, is there any relation between the two extreme volume fractions of this hard particle glass physics problem: ϕ_c and ϕ_{RCP}? Using the experimentally deduced value for the latter, and the CM-nMCT value for the former, the ratio is nearly constant: $\phi_{RCP} / \phi_c : 1.50 \pm 0.04$. This suggests a connection between the onset of glassy activated dynamics and granular jamming. The theoretical calculations of *G'* have also been analyzed in the above fashion, and a good collapse is obtained (not shown) with best fit

values: ϕ_{RCP}=0.66 (sphere), 0.715 (dicolloid), 0.757 (tricolloid). The latter are surprisingly close to those deduced from the experimental data collapse exercise.

3.4 Conclusion

In conclusion, first combined experimental-theoretical study of kinetic vitrification and elasticity in dense suspensions of repulsive nonspherical colloids has been performed. Modest shape anisotropy strongly delays the onset of kinetic arrest and emergence of elasticity. The shear modulus grows roughly exponentially with volume fraction, and a theoretically-inspired universal master plot can be achieved for all shapes and repulsion strengths based on the concepts of an effective hard core diameter, particle volume as the relevant parameter for stress storage, and distance from the ideal MCT crossover as the relevant measure of crowding. Power law scaling and collapse of the modulus data at very high concentrations is achieved in accord with the theoretical suggestion.[5, 14] All the experimental behavior is well described by the recently developed mode coupling and activated barrier hopping theories for nonspherical colloids. In future work, the effect of particle shape on attraction-driven kinetic arrest, gel-like elasticity, and re-entrant cage melting [31] in chemically homogeneous and patchy colloidal suspensions will be studied.

3.5 Figures and Tables

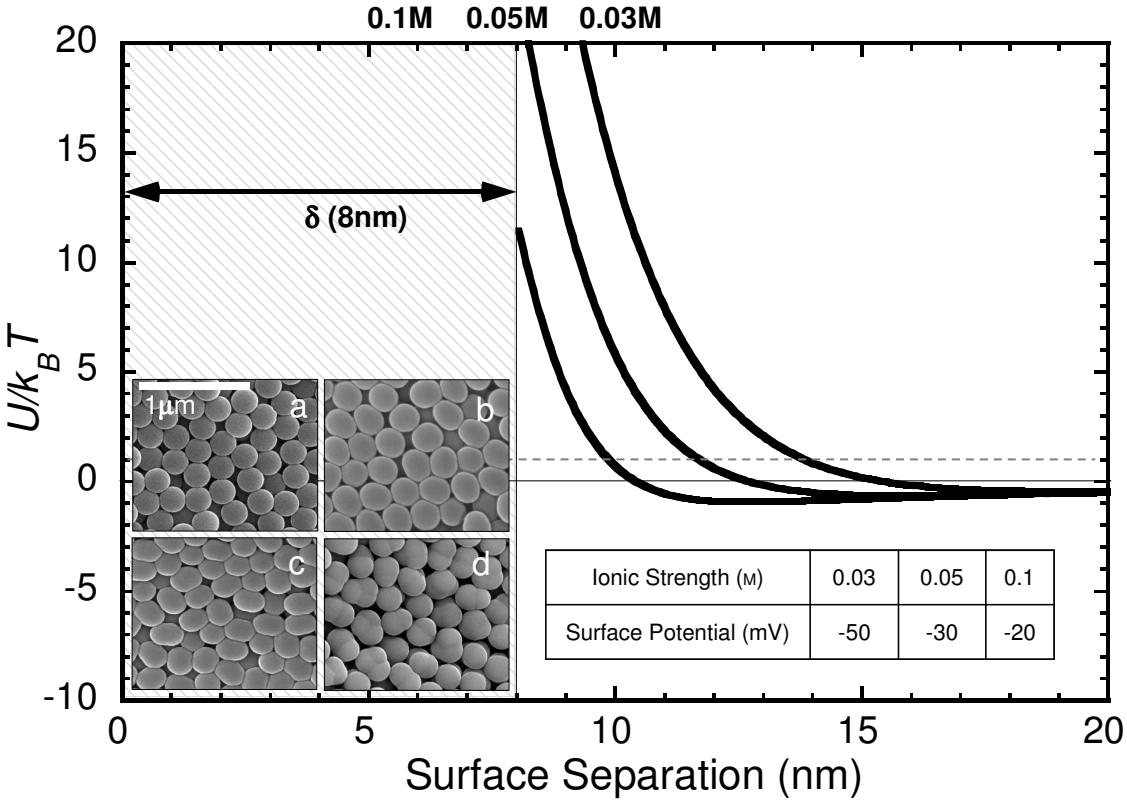

Figure 3.1 Pair interaction potentials determined by summation of van der Waals, electrostatic and surfactant-induced forces for ionic strengths of 0.03M, 0.05M, 0.1M. The horizontal dashed line is drawn at $1k_BT$, and defines the distance used for Δ and D_{eff}. (Inset) SEM micrographs of dense packing of the four particle shapes studied: S (a), hDC (b), sDC (c), and TC (d).

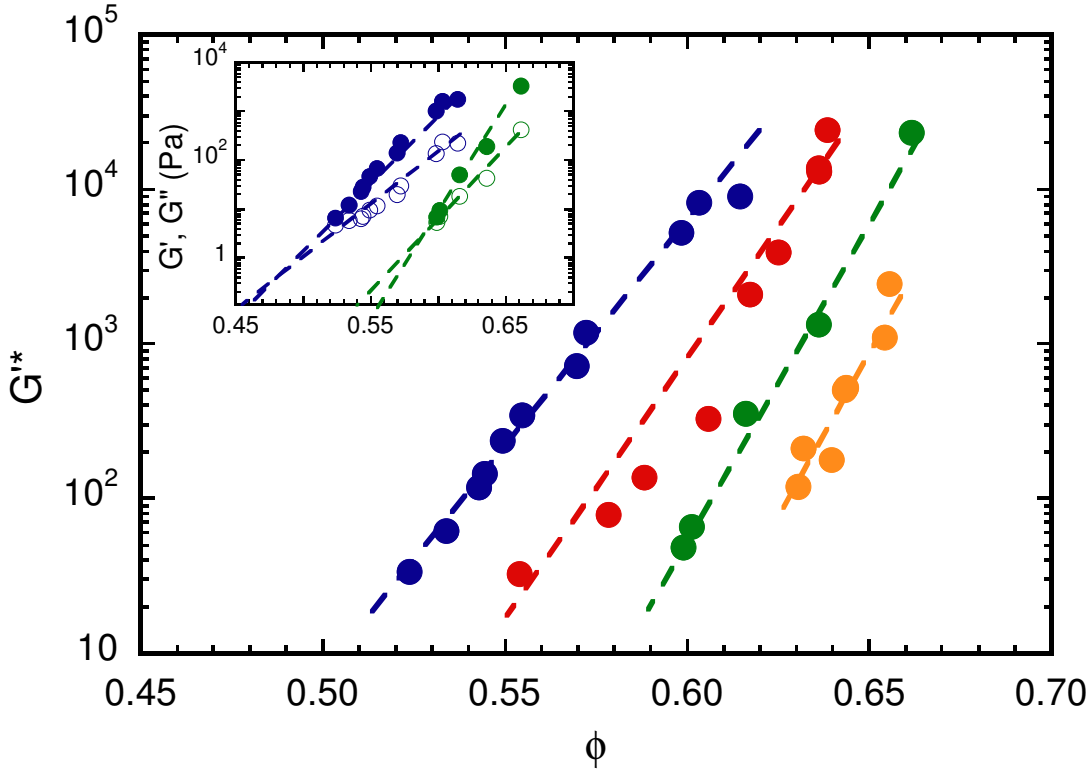

Figure 3.2 Dimensionless elastic shear modulus, *G'**, as a function of volume fraction for the four shapes at an ionic strength of 0.03M (S-blue, hDC-red, sDC-green, TC-orange). (Inset) Method used to determine experimental kinetic glass transition volume fraction, ϕ_g.

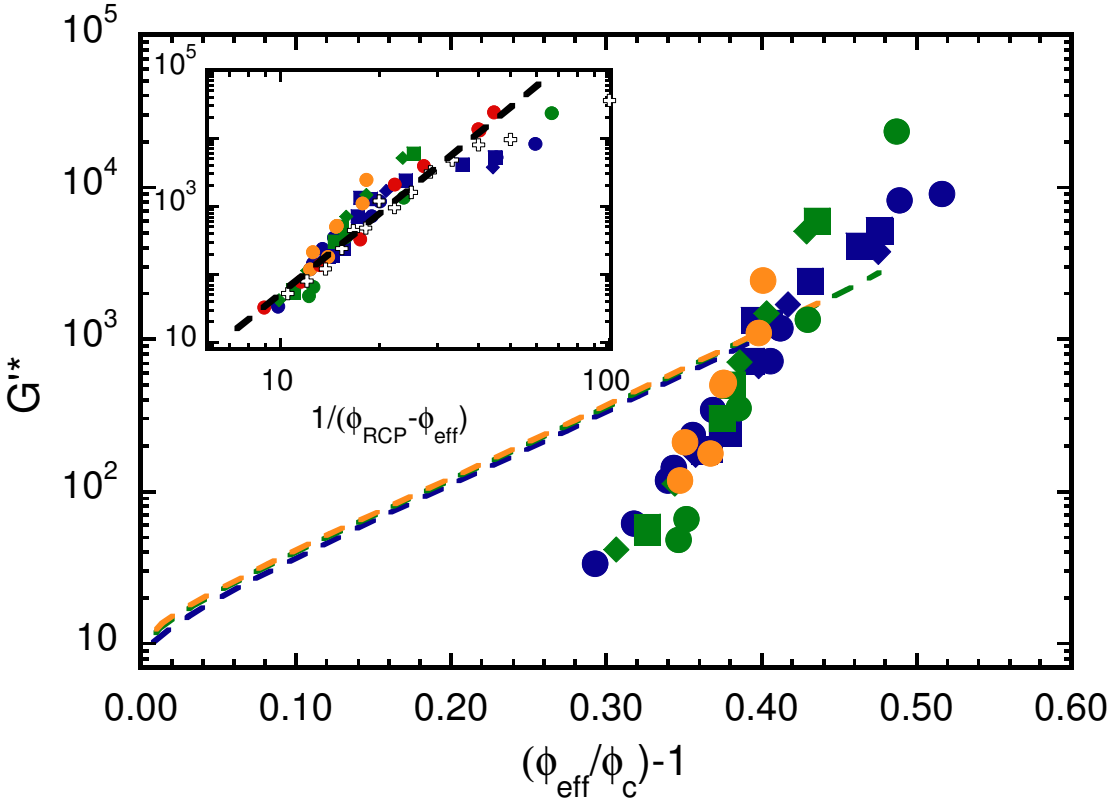

Figure 3.3 Collapse of experimental *G'** data based on the volume fraction scaling (ϕ_{eff}/ϕ_c)-1. Theory (dashed curve) and experimental data (points) are shown for S (blue), sDC (green), hDC (red), and TC (orange) and for ionic strengths of 0.03M (circles), 0.05M (squares), and 0.1M (diamonds). (Inset) *G'** plotted as a function of $1/(\phi_{RCP}-\phi_{eff})$. Hard sphere colloid data from ref. [29] is shown as open points. A dashed line of slope 4 is drawn indicating the theoretically predicted dependency.

Shape	Ionic Strength	$\phi_{g(exp)}$	$\phi_{g(theory)}$
S	0.03	0.475	0.545
	0.05	0.482	0.558
	0.1	0.525	0.564
hDC	0.03	0.551	
sDC	0.03	0.589	0.601
	0.05	0.584	0.614
	0.1	0.603	0.618
TC	0.03	0.606	0.645

Table 3.1 Experimental and theoretical values (not done for heteronuclear dicolloid) of the kinetic glass transition volume fraction of the four particle shapes at three ionic strengths.

3.6 List of References

[1] Russel, W.B., D.A. Saville, and W.R. Schowalter, *Colloidal Dispersions*. 1989, Cambridge, UK: Cambridge Universtiy Press.
[2] Glotzer, S.C. and M.J. Solomon, *Nat. Mat.*, **2007**, 6(7), 557.
[3] van Blaaderen, A., *Nature* **2006**, 439(7076), 545.
[4] Jiang, S., Q. Chen, M. Tripathy, E. Luijten, K.S. Schweizer, and S. Granick, *Adv. Mat.*, **2010**,.
[5] Yatsenko, G. and K.S. Schweizer, *J. Chem. Phys.*, **2007**, 126.
[6] Pfleiderer, P., K. Milinkovic, and T. Schilling, *Europhysics Letters*, **2008**(1), 16003.
[7] Götze, W. and L. Sjörgen, *Rep. Prog. Phys*, **1992**, 55, 241.
[8] Chong, S.-H. and W. Götze, *Phys. Rev. E*, **2002**, 65(4), 041503.
[9] Letz, M., R. Schilling, and A. Latz, *Phys. Rev. E*, **2000**, 62(4), 5173.
[10] Zhang, R. and K.S. Schweizer, *Phys. Rev. E*, **2009**, 80, 011502.
[11] Tripathy, M. and K.S. Schweizer, *J. Chem. Phys.* **2009**, 130(24), 244906.
[12] De Michele, C., R. Schilling, and F. Sciortino, *Phys. Rev. Lett. L*, **2007**, 98(26), 265702.
[13] Moreno, A.J., S.-H. Chong, W. Kob, and F. Sciortino, *J. Chem. Phys.*, 123, 204505.
[14] Yatsenko, G. and K.S. Schweizer, *Phys. Rev. E*, **2007**, 76, 014505.
[15] Donev, A., I. Cisse, D. Sachs, E.A. Variano, F.H. Stillinger, R. Connelly, S. Torquato, and P.M. Chaikin, *Science*, **2004**, 303(5660), 990-993.
[16] Sacanna, S., L. Rossi, A. Wouterse, and A.P. Philipse, *Journal of Physics: Condensed Matter*, **2007**(37), 376108.
[17] van Megen, W. and S.M. Underwood, *Phys. Rev. E J1 - PRE*, **1994**, 49(5), 4206 LP - 4220.
[18] Götze, W., *J. Phys.: Cond. .Matt.*, **1999**, 11.
[19] Weeks, E.R. and D.A. Weitz, *Phys. Rev. Letters*, **2002**, 89.
[20] Kumar, S.K., G. Szamel, and J.F. Douglas, *J. Chem. Phys.*, **2006**, 124, 214501.
[21] Brumer, Y. and D.R. Reichman, *Phys. Rev. E*, **2004**, 69, 041202.
[22] Brambilla, G., D.E. Masri, M. Pierno, L. Berthier, L. Cipelletti, G. Petekidis, and A.B. Schofield, *Phys. Rev. Lett.*, **2009**, 102, 085703.
[23] Schweizer, K.S., *Curr. Op. Coll. Inter. Sci.*, **2007**, 12, 297.
[24] Schweizer, K.S. and E.J. Saltzman, *J. Chem. Phys.*, **2003**, 119(2), 1181
[25] Mock, E.B., H. De Bruyn, B. Hawkett, R. Gilbert, and C.F. Zukoski, *Langmuir*, **2006**, 22.
[26] Partridge, S.J., *Rheology of Cohesive Sediments*, in *Dept. of Physical Chemistry*. 1985, Bristol University.
[27] Kramb, R.C. and C.F. Zukoski, *Langmuir*, **2008**, 24(14), 7565.
[28] Chandler, D. and H.C. Andersen, *J. Chem. Phys.*, **1972**, 57, 1930.
[29] Schweizer, K.S., *The Journal of Chemical Physics*, **2007**, 127(16), 164506.
[30] Koumakis, N., A.B. Schofield, and G. Petekidis, *Soft Matter*, **2008**, 4, 2008.

[31] Pham, K.N., A.M. Puertas, J. Bergenholtz, S.U. Egelhaaf, A. Moussaid, P.N. Pusey, A.B. Schofield, M.E. Cates, M. Fuchs, and W.C.K. Poon, *Science*, **2002**, 296(5565), 104.

Chapter 4 Reentrant Phase Behavior and the Effects of Attractions on Shear Elasticity

4.1 Introduction

Great excitement has been recently generated by computer simulation studies which reveal unique clustering arrangements and long range order of particles with anisotropic shape and/or interaction potentials.[1-4] In parallel, there have been numerous reports of the synthesis of nanoparticles and colloids with anisotropic shape.[4-13] Simulations suggest that when chemically heterogeneous or "patchy" particles experience a limited number of attractive interactions there is a large reduction of the critical temperature for liquid-gas type of phase separation.[1] In addition, microscopic theory and simulation find particle shape anisotropy can strongly modify the onset of nonequilibrium glassy states including a striking nonmonotonic dependence of the vitrification volume fraction on the degree of anisotropy of dumbbells,[14-17] triatomics,[18] spherocylinders,[18, 19] and ellipsoids-of-revolution.[20, 21] Similar nonmonotonic variation has been observed for the jamming packing fraction of hard granular ellipsoids and spherocylinders.[22, 23]

At the moment, simulation and theory are well ahead of experimental confirmation in advancing understanding of suspensions of structurally and/or chemically anisotropic particles. Experimental advances have been limited by two major hurdles. First, synthetic methods for producing large quantities of uniform anisotropic particles are in their infancy. Because the synthetic methods result in particles that are either not uniform or are relatively scarce, exploration of the large array of configurations and bulk properties associated with shape and interaction energy anisotropy have been limited. Until methods are developed that consistently produce uniform particles with reliable anisotropy in large quantities, progress will be slow. Second, even when such particles

can be synthesized in large quantities, methods for characterizing the strength of the anisotropic interactions are poorly developed.

Progress in developing a predictive theoretical understanding requires accounting for shape and interaction energy anisotropy in ways that are mathematically tractable. Recent advances have been reported based on the microscopic ideal mode coupling theory (MCT) framework[15] for shape anisotropic hard particles. For example, MCT has been used to make predictions of the influence of shape anisotropy on the kinetic arrest or glass transition that accounts for both center-of-mass and orientational degrees of freedom.[14, 20] Quantitative predictions are possible due to the development of theoretical methods to describe the structure of isotropic fluids. However, the full MCT of nonspherical particles[14, 20] is mathematically and computationally complex such that it has seen limited application to the vast array of particle shapes and pair potentials now possible to realize experimentally. Moreover, recent advances suggest the MCT glass or gel transition is a dynamical crossover marking the onset of collective dynamics.[15, 24] The enormous power of MCT and its extensions lies in its ability to define the volume fraction where this crossover takes place and changes in elasticity and relaxation times as volume fraction is increased above the crossover volume fraction. Due to the complexity of the original MCT, design rules that can guide the experimentalist in choosing particle shape or interaction energy to achieve desired properties largely do not exist.

Here the experimental results are presented of a coordinated experimental and theoretical approach aimed at developing these designing rules for suspensions of weakly anisotropic particles composed of fused spheres of equal size that are often called (homo) dicolloids.

4.2 Experimental

For a quantitative comparison between experiment and theory interaction energy parameters are required. These one chooses based on experimental values for the zeta potential, the Debye Huckel decay length set by the ionic strengths and a van der Waals attraction for spheres with a Haymaker coefficient of $3.1k_BT$ with a minimum surface to surface separation of 8nm due to adsorbed surfactant. Best fits to these interactions are done with a double Yukawa pair potential of the form

$$\frac{U(r)}{k_BT} = -\frac{AD}{r}\exp\left(-\frac{D}{\lambda_a}\left(\frac{r}{D}-1\right)\right)+\frac{BD}{r}\exp\left(-\kappa D\left(\frac{r}{D}-1\right)\right)$$

Where A is the contact value of the truncated van der Waals attraction, $2.3k_BT$, and the decay length, $\lambda_a = 0.025D$ while B is set at the contact value of the electrostatic repulsion based on the zeta potential, as measured by electrophoresis, and the decay length is $1/\kappa$ where κ is the Debye Huckel parameter. The values used in the calculations for each ionic strength are shown in Table 4.1 and the accuracy of the Yukawa fits is shown in Fig. 4.1 where the total interaction energy for each ionic strength is plotted along with the results of the calculation using the fit parameters.

The particles used in this work were synthesized using a modified version of the seeded emulsion polymerization technique from Mock et al.[8] The seeds used to make the spherical particles contained no divinylbenze (DVB) crosslinker, while the seeds used for the dicolloids contained 2% DVB (Aldrich, 55% mixture of isomers tech. grade) by weight. The seeds were otherwise identical and synthesized by surfactant stabilized polymerization of styrene with SDS as the surfactant. Both sets of seed particles were synthesized in 5L round bottom flasks immersed in a constant temperature water bath. A

poly-tetraflouroethylene coated blade attached to a rotating glass bar was used for stirring. Initially 3.75g of SDS was dissolved in 3000mL of deionized water. The water was allowed to reach a steady state temperature of 80°C and 350mL of styrene monomer (Sigma-Aldrich, 99% purity grade) was added. For the dicolloid seeds, the DVB was dissolved into the styrene added in this step. The solution was stirred at 80°C for one hour at a vigorous speed. 11.7g of potassium persulfate initiator (Fisher Scientific 99.5% purity grade) dissolved in 560mL of water was then added, and the reaction was allowed to proceed for 24 hours. The resulting seed particles were nearly identical: 210nm in diameter (± 3.2nm) for the sphere seeds, 211nm (± 1.5nm) for the dicolloid seeds.

The particles were then swollen with additional styrene monomer at a mass ratio of 2:1 (swelling styrene to seed particle mass). For this swelling step, 880mL of the seed particle solution was poured into a 5L round bottom flask along with 620mL of a 0.1M potassium hydroxide (KOH) solution, 2.5g of SDS, and 2.4g of azobisisobutyronitrile (AIBN) dissolved in 130mL of additional styrene. The flask was stirred at room temperature for 24 hours. When the swelling was complete, 5mL of methacrylic acid and 40g of hydroquinone dissolved in 500mL of the KOH solution were added to the vessel and the temperature was elevated to 70°C. The reaction proceeded for 24 hours. The resulting final particles can be seen in the inset of Figure 4.1. The spheres had a mean diameter of 270nm (±1.6nm) while the dicolloids had a mean long axis length of 330nm (±2.2nm) and a mean short axis length of 250nm (±2.1nm) as measured by scanning electron microscopy (SEM Hitachi S4700). The aspect ratio of the dicolloids, length divided by sphere diameter, is L/D = 1.3. Accuracy of the SEM measurements was

confirmed by dynamic light scattering using a Brookhaven Instruments fiber optic quasi-elastic light scattering (FOQELS) device.

After synthesis the particles are dialyzed against a polyethylene glycol (20,000 molecular weight, Sigma) in deionized water solution with approximately 30g-50g of PEG and 3L of water to remove unwanted electrolytes and oligomers. The dialysis process also concentrates the particles by drawing water out from the dialysis tubes. Once the volume fraction of particles in the tube reached approximately 0.35-0.40, 15-25mL portions of the solution were transferred to a 50mL centrifuge tube containing 0.338g of the surfactant $C_{12}E_6$. The $C_{12}E_{6,}$ coats the surface of the particles and results in a bound steric layer 4 nm thick.[25] This layer sets the minimum surface-to-surface separation where the van der Waals forces from the polystyrene cores are operative to be 8nm. By working with particles of diameter D = 200-300 nm, the maximum well depth at contact of the surfactant coated particles is 1-5k_BT. Finally, a bulk solution of either 0.1M, 0.5M 1.0M or 5.0M sodium chloride (Fischer Scientific, crystalline) dissolved in deionized water was added such that the final concentration of $C_{12}E_6$ was 0.03M, the ionic strength of the solution varied from 0.03M to 1.0M and the total volume in the tube was 25mL. The tubes were then centrifuged at 6000 rpm for one hour intervals and the supernatant removed until further centrifuge cycles produced no removable supernatant. The volume fraction of particles at this stage ranged from 0.55 – 0.65 and became the bulk particle solution to be diluted for rheological experiments.

At low ionic strength (<0.01M), the surface charges are not significantly screened and the particles experience long range repulsive forces. These conditions prevent dense packing and encourage ordering of the particles at low concentrations. The soft repulsion

also blurs the differences between the two particle shapes.[26] The goal is to investigate hard core and attractive interactions where shape differences will be accentuated. As a result, it is chosen to work at higher salt concentrations. At ionic strengths of 0.03M-0.1M, the surface charges are moderately screened. The Debye screening length is ~1-2nm and the resulting pair potentials resemble those of hard particles but with slightly larger dimensions than the surfactant coated particles. At ionic strengths near 0.3M where the Debye screening length is 0.5nm or smaller, a weak attractive minimum in the pair potential emerges. Finally, at the highest ionic strengths (>0.5M), essentially all surface charges are screened and an attractive well depth of 3-5k_BT is established. Particles rapidly aggregate and, at high enough volume fractions, form gels. These features are demonstrated in Figure 4.1 where the pair potentials are shown calculated using a Hamaker coefficient of 3.1k_BT and particle surface potentials of -20, -16, -12 and -8, -3, and <-1mV for [I]=0.03, 0.05, 0.1, 0.3, 0.5, and 1.0M respectively. The surface potentials were derived from electrophoresis measurements. Particle surface potentials were independent of particle shape.

Confirmation that approximate "hard" pair interaction conditions have been reached at 0.03M is made by measuring the viscosity of suspensions of spheres and dicolloids as a function of ionic strength at a volume fraction of 0.3, as seen in Fig. 4.2. At low to moderate volume fractions (i.e., below ϕ_c determined by nMCT) where localization does not occur, repulsions and attractions will both increase viscosity above the hard interaction values.[27] Above ϕ_c attractions have been shown to result in viscosities below the hard interaction values.[28] The minimum in viscosity in Fig. 4.2 is

viewed to be the point where the particles are optimally hard, which occurs at ionic strengths of 0.02-0.05M.

Rheological measurements including viscosities and moduli were obtained using a Bohlin C-VOR rheometer with a cup and bob geometry. The bob is a made from roughened titanium with a diameter of 14mm and a gap size of 0.7mm with a sample volume of 3mL. Temperature was maintained with a constant temperature water bath at 30 ± 0.5°C.

The following protocol was used to obtain measurements from the rheometer. 3.2mL of the highly concentrated bulk suspension from the centrifuge tube was transferred to the rheometer cup. 0.2mL was then removed and the mass was measured in a 20mL scintillation vial. The vial was then placed in an oven at 110°C to remove water from the solution. The dried weight was measured after 24 hours and the weight fraction of polystyrene was calculated (taking into account remaining salt in the vial). This was converted into a volume fraction using reported densities of polystyrene (1.05g/mL), and measured values of water containing NaCl. The remaining 3mL of sample in the cup was used for the experiments.

A solvent trap was placed around the shaft of the bob limiting water evaporation and volume fraction increases during experiment runs. However, even with the solvent trap in place, total experimental time longer than 30 minutes for any one sample was avoided as changes in mechanical properties were observed after this length of time.

The sample was presheared at a rate of $50s^{-1}$ for 2 minutes. The elastic and viscous moduli were measured as a function of applied stress at a frequency of 1Hz for

the first experiment for each sample. The modulus measured in the plateau of this stress sweep is the value reported for each volume fraction in the figures of the results section.

After the first set of experiments at a specified ionic strength, the bob was cleaned and any sample remaining on the bob was discarded. The sample remaining on the cup however was kept in order to conserve materials and allow an adequate number of volume fractions to be studied. Approximately 2.5 – 2.8mL of the previous sample typically remained in the rheometer cup after this initial experiment. To this, an additional 0.1mL of a solution containing 0.03M $C_{12}E_6$ and dissolved NaCl (at the same ionic strength as the sample already in the cup) was added. Finally, a small amount of the bulk particle solution from the centrifuge tube was added until the total volume in the cup again reached 3.2mL. The process for measuring volume fraction was the repeated for this sample. The effect of this material-conserving dilution process was that the volume fraction for the new sample decreased by about 0.01-0.02% from the previous sample. The entire process was then repeated again, lowering the volume fraction each time, until a plateau in the elastic modulus could not be observed at even the lowest stresses of the stress sweep experiment discussed below.

4.3 Results and Discussion

For each ionic strength, a stress sweep is preformed on the sample measuring elastic and viscous modulus (*G'*, *G"*). At small stresses, a plateau, linear response modulus is observed. All subsequent references to *G'* and *G"* refer to this plateau value of the modulus which is used to determine the state diagram of the system.

Following a Maxwell body construction, for each ionic strength, one defines a system with a relaxation time of 2πs as occurring when $G'=G''$. For larger volume fractions, the relaxation time is longer than the experimental time and the system displays solid-like properties. As a result this is used as the criteria for determining the experimental kinetic glass transition volume fraction (ϕ_g). The procedure for locating the volume fraction where $G'=G''$ at 1Hz is outlined in Fig. 4.3. In this figure, G' and G'' are plotted for S and sDC at ionic strengths of 0.03M and 0.3M. $G'(\phi)$ and $G''(\phi)$ are fit to exponential functions and equation is extrapolated to $G'=G''$. Limited frequency sweeps were made to investigate the frequency dependence of the modulus. As shown in Fig. 4.4 one sees that for spheres at an ionic strength of 0.03M (ϕ_g= 0.48) as volume fraction is increased, the characteristic relaxation time moves rapidly to long times as volume fraction rises above ϕ_g. For all values of G' reported here, ϕ/ϕ_g>1.1 and an experimental frequency of 1Hz falls within the glassy plateau.

Figure 5 shows a summary plot for ϕ_g for spheres and dicolloids at the five ionic strengths used in the stress sweep experiments. Both spheres and dicolloids show reentrant behavior where the glass transition boundary moves first to higher volume fractions and then to lower volume fractions with increasing ionic strength. This behavior is reminiscent of the reentrant behavior seen in depletion attraction systems and indicates that weak attractions results in greater particle mobility in dense suspensions of both particle shapes where as strong attractions reduce particle mobility and enhance the modulus.

Using parameters in Table 4.1, $S(q)$ is determined for the dicolloids and spheres as a function of volume fractions and ionic strength. From these equilibrium structure

factors, the cross over volume fraction is determined. These values are plotted as dashed lines in Fig. 4.5. The predicted values of ϕ_c display the same qualitative behavior as the experimental ϕ_g's showing reentrant behavior and with small shape anisotropies predicted to delay the onset of glassy dynamics. The quantitative off set can be understood in two ways. First, naïve Mode Coupling Theory is known to under predict ϕ_c compared to full Mode Coupling Theory. Secondly and more importantly, as opposed to predicting an idealized glass transition at ϕ_c, the implementation of nMCT in conjunction with the nonlinear Langevien equation indicates that ϕ_c marks the onset of cooperative dynamics and for $\phi > \phi_c$, relaxation times grow. Methods to calculate the relaxation time from the NLE nMCT model are discussed in detail in references[24, 29] and are implemented here to predicted the volume fractions where the suspensions will show relaxation times of 2πs, which corresponds to the experimental conditions. Relaxation times of 1s and 50s are also shown in Fig. 4.5. As expected, the experimentally defined kinetic glass transition occurs at volume fractions above ϕ_c.

The agreement between experiment and theory is nearly quantitative. The theory predicts both the effects of moderate particle shape anisotropy as well as the reentrant shape of the state diagram as the particle interaction potential moves from repulsive to attractive. The remarkable nonmonotonic variation of the dynamic crossover (nMCT) volume fraction with aspect ratio previously theoretically predicted for hard dicolloids[14, 17] remains valid for soft repulsive colloids and for the kinetic glass transition boundaries. Figure 4.5 shows that introducing modest particle anisotropy dramatically delays the onset of vitrification. To place this result in context it is noted the random close packing or maximally random jammed volume fraction of hard spheres is ~0.64.[22]

In addition to the viscous to elastic crossover, the stress sweep experiments allow one to examine the absolute values of the elastic shear modulus, *G'* as a function of volume fraction. This can also be compared to theoretical predictions from nMCT, as the theory has the ability to calculate zero shear moduli using the double Yukawa potentials from above as input.

Figure 4.6 shows *G'** (*G'* made dimensionless by either D^3/k_BT in the case of spheres or L^2D/k_BT for dicolloids),[17] as a function of volume fraction for each experimental sample on a log-linear scale. At each ionic strength, *G'* for the dicolloids lies below that of the spheres. This shows that not only is the onset of vitrification delayed with shape anisotropy, but a glass made of dicolloids will be weaker than a glass of spheres at the same volume fraction.

Based on previous theoretical work,[17-19] it is predicted that for particles experiencing hard core interactions, rescaling the volume fraction on the distance from ϕ_c (i.e. ϕ/ϕ_c-1) will result in collapse of the data making *G'* independent of shape. Since one cannot measure ϕ_c experimentally, and supported by the accuracy of the predictions of ϕ_g, the nMCT predictions for ϕ_c are used as shown previously in Figure 4.5.

The results of the rescaling are shown in Fig. 4.7 along with the nMCT calculations for *G'**. For the repulsive conditions, the shape collapse previously predicted only for hard particles holds. The sphere and dicolloid data for 0.03M nearly superimpose. This is also what is predicted from the nMCT calculations using the double Yukawa potentials as can be seen in the solid and dashed curves for these conditions. However, the theoretical collapse fails for 0.1M with the predictions for spheres below that of dicolloids. This trend is reversed at 0.5M as the theory predicts a return of

collapse. Although the experiments do not show collapse at 0.5M, the trend predicted by the theory relative to 0.1M is correct. The relative change in position due to shape as ionic strength is increased matches the experiments.

Since the sphere and dicolloid experimental data from the three lower ionic strengths superimpose (which was predicted initially only for hard interactions), these can be considered "effectively hard" particles. The difference between the repulsive conditions can be eliminated if one adjusts the size of the particles to take into consideration the increased diameter due to the electrostatics. For this, a surface to surface distance Δ is defined where the particles experience a pair repulsion of magnitude $1k_BT$, and define $D_{eff}=D+\Delta$, $L_{eff}= L+\Delta$ and $\phi_{eff}=\phi(1+\Delta)^3$. The rescaling of volume fraction then becomes (ϕ_{eff}/ϕ_c^H-1) where ϕ_c^H is the localization volume fraction for hard particles (spheres or dumbbells). The result is shown in Fig. 4.8 along with the nMCT predictions for all hard dicolloids independent of aspect ratio. Indeed all points fall nearly on the same curve thus confirming the assumption that particles experiencing partially screened electrostatic repulsions and truncated van der Waals attractions can be modelled as hard.

The experimental results confirm three major predictions from the NLE nMCT: 1) the shape of the state diagram and location of ϕ_g, 2) the effects of ionic strength on the elastic shear modulus, and 3) the collapse of the data for effectively hard conditions when volume fraction is scaled on $(\phi_{eff}/\phi_c^H)-1$. However, the dependence of G'^* on (reduced) volume fraction has *not* been confirmed. The theory under predicts the exponent (γ) for $G'^* \sim(\phi/\phi_c-1)^\gamma$. This is not surprising. Data measured at ω = 1Hz is reported while the theory calculates a modulus that will be correct only for the zero frequency limit. The materials will reach terminal viscous behavior for frequencies $\omega > 2\pi/\tau_{hop}$. With

increasing volume fraction τ_{hop} increases rapidly such that only for sufficiently large ϕ/ϕ_c will the recorded modulus approximate the zero frequency modulus. With increasing measurement frequency, one expects the modulus to grow towards the theoretical values. Unfortunately, due to instrument limitations, experiments at higher frequencies were not possible with this system.

4.4 Conclusion

An experimental system has been designed to probe how the weak shape anisotropy of uniaxial particles and variable particle interaction impacts phase behavior, slow dynamics, and kinetic vitrification of dense suspensions. The introduction of shape anisotropy dramatically delays the onset of the glass formation, as predicted theoretically. Tuning the particle interaction from repulsive to near hard to attractive reveals reentrant phase behavior. While reentrant phase behavior has been demonstrated in other systems, this is the first using truncated van der Waals forces and electrostatics as the source of attractions and the first to show that the reentrancy phenomenon is also found in suspensions of nonspherical particles. This is a potentially revolutionary finding for those concerned with delaying particle arrest: both weak shape anisotropy and weak particle attractions have additive contributions to increasing the glass transition volume fraction of a suspension.

4.5 Figures and Tables

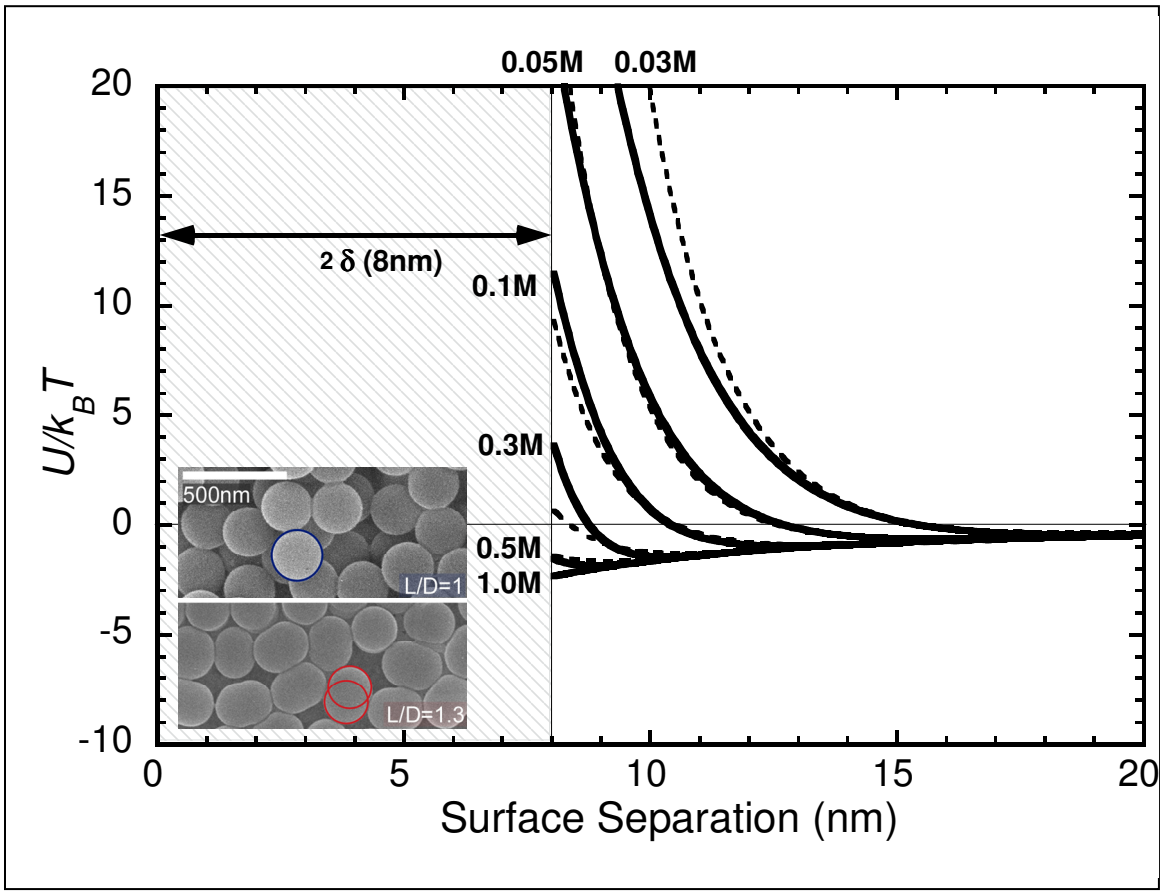

Figure 4.1. Calculations for particle pair interaction energies for full van der Waals + electrostatic forces (solid curves) and double Yukawa fits (dashed curves) (Inset) SEM micrographs of the sphere and dicolloid particles

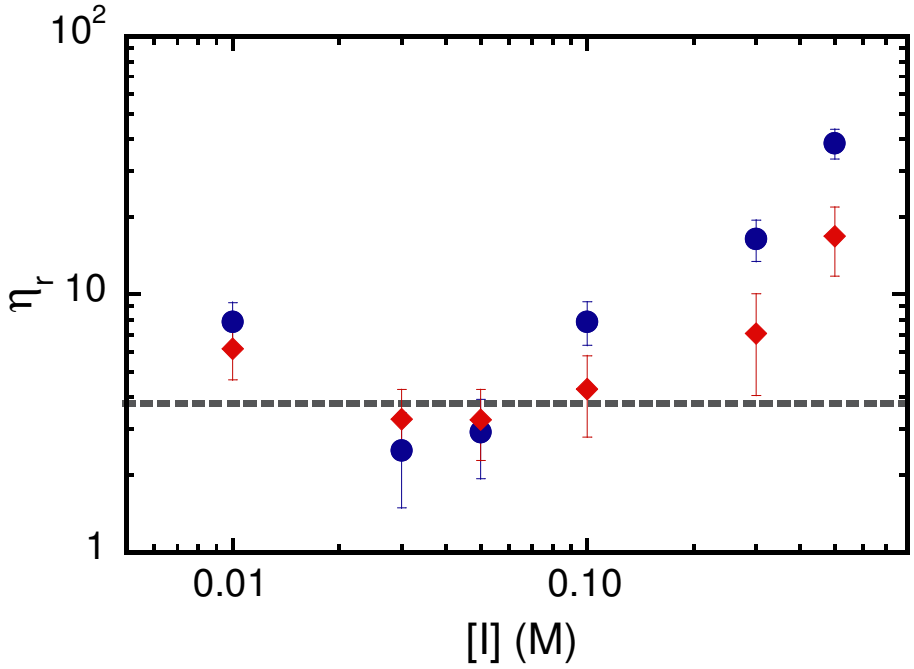

Figure 4.2. Low shear rate viscosities of suspensions of sphere (blue) and dicolloid (red) particles at ionic strengths from 0.01 – 0.5M and $\phi \approx 0.30$. A minimum is reached at ~0.02-0.05M indicating approximately hard core interactions. Hard sphere viscosity at $\phi = 0.3$ is shown as a dashed line. [30]

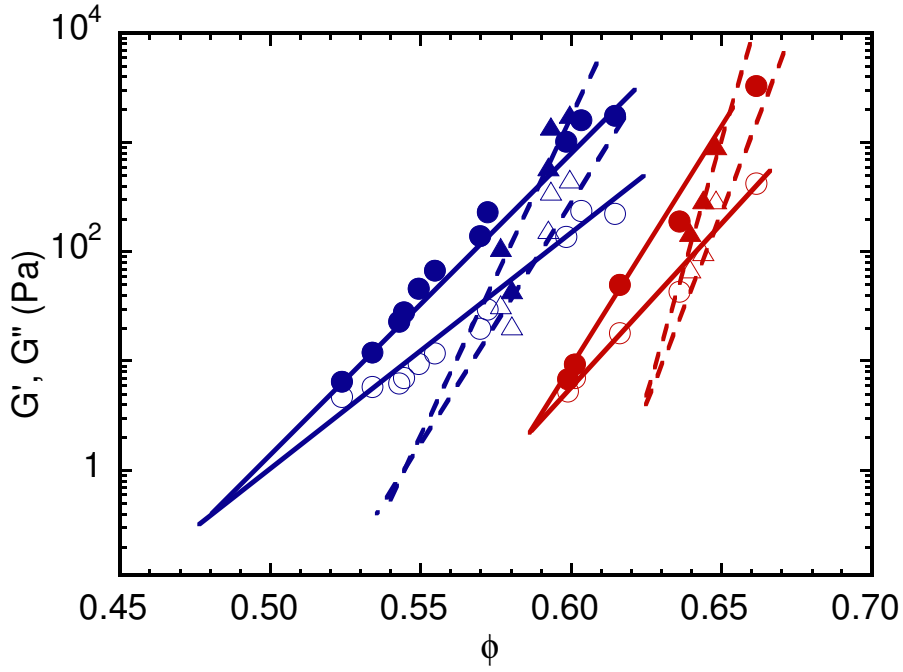

Figure 4.3. Procedure for determining ϕ_g. $G'(\phi)$ (solid points) and $G''(\phi)$ (open points) are plotted for S (blue) and sDC (red) at ionic strengths of 0.03M (circles) and 0.3M (triangles) and 1Hz.

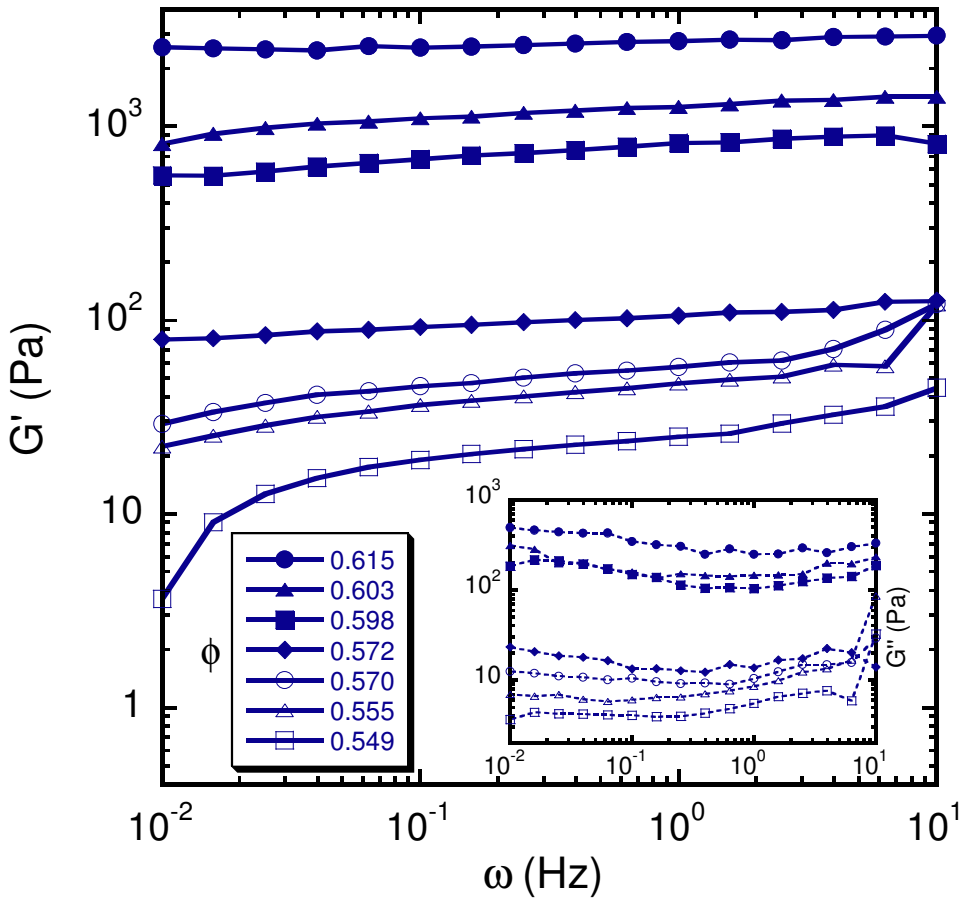

Figure 4.4. (main panel) $G'(\omega)$ for spheres at 0.03M and volume fractions $>\phi_g$ demonstrating observance of a glassy plateau in the frequency range near 1Hz. (inset) $G''(\omega)$ for same conditions.

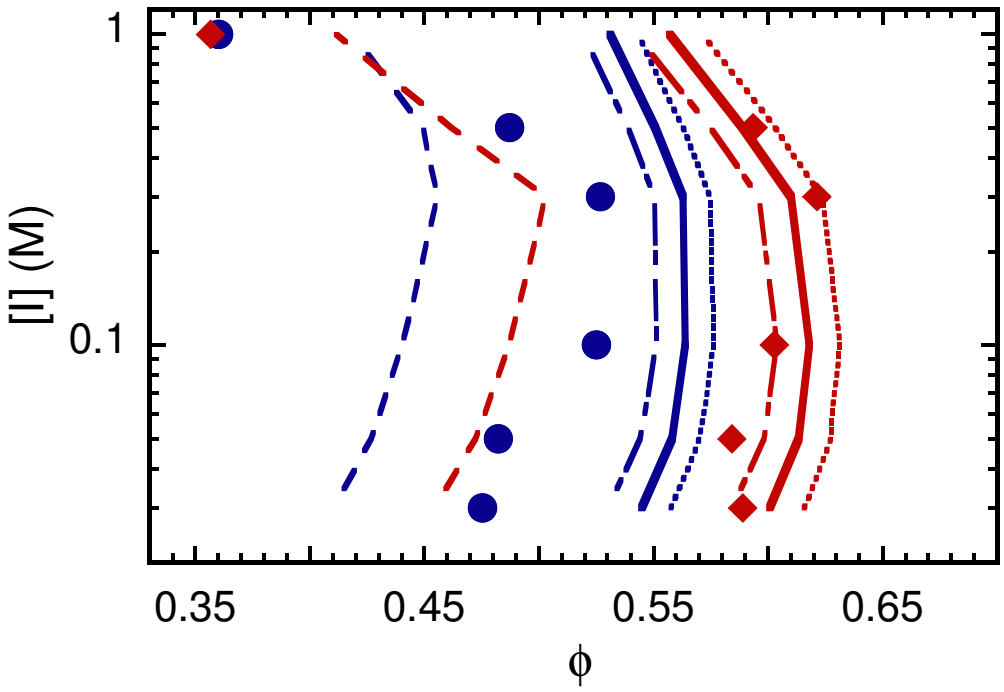

Figure 4.5. State diagram showing ϕ_g for S (blue) and sDC (red). Experimental ϕ_g is shown as points. NLE nMCT calculations for ϕ_c is shown in dashed curve. NLE nMCT calculations for kinetic ϕ_g are shown using τ = 1s (dash-dot), 2πs (solid), 50s (dot).

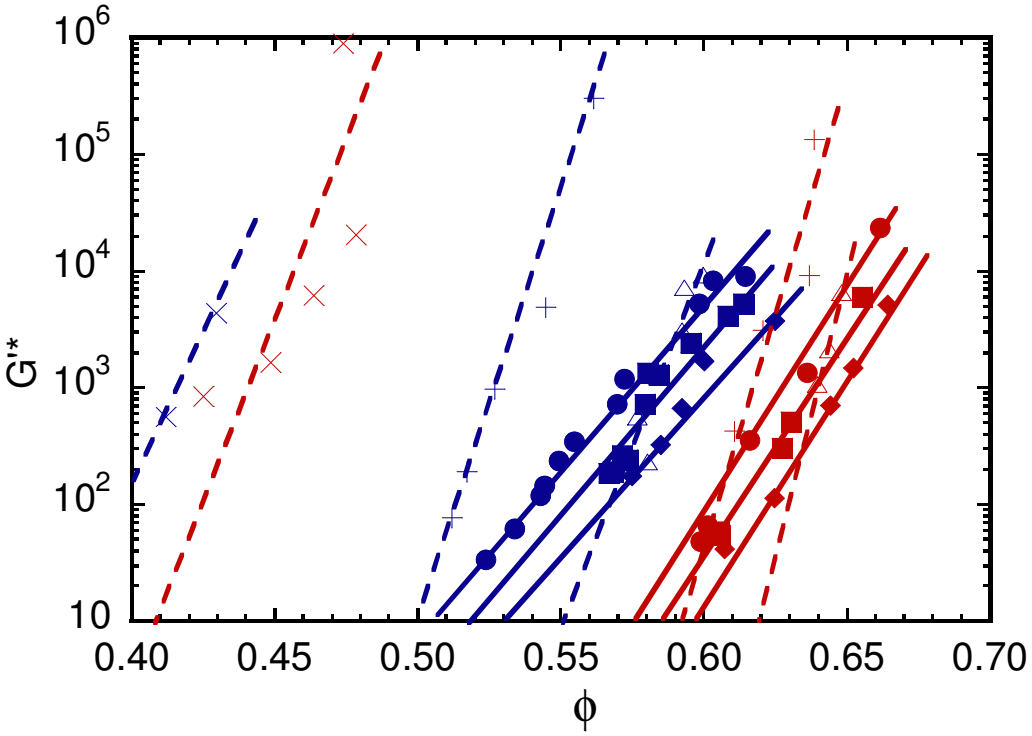

Figure 4.6. Measured low shear dimensionless elastic modulus of spheres (blue) and dicolloids (red) at ionic strengths of 0.03 (circles), 0.05 (squares), 0.1 (diamonds), 0.3 (open triangles), 0.5 (plus), 1.0 (x's). Lines are drawn to guide the eye to each set of data at a single ionic strength. Solid lines/closed points represent repulsive conditions while dashed lines/ open points represent attractive conditions.

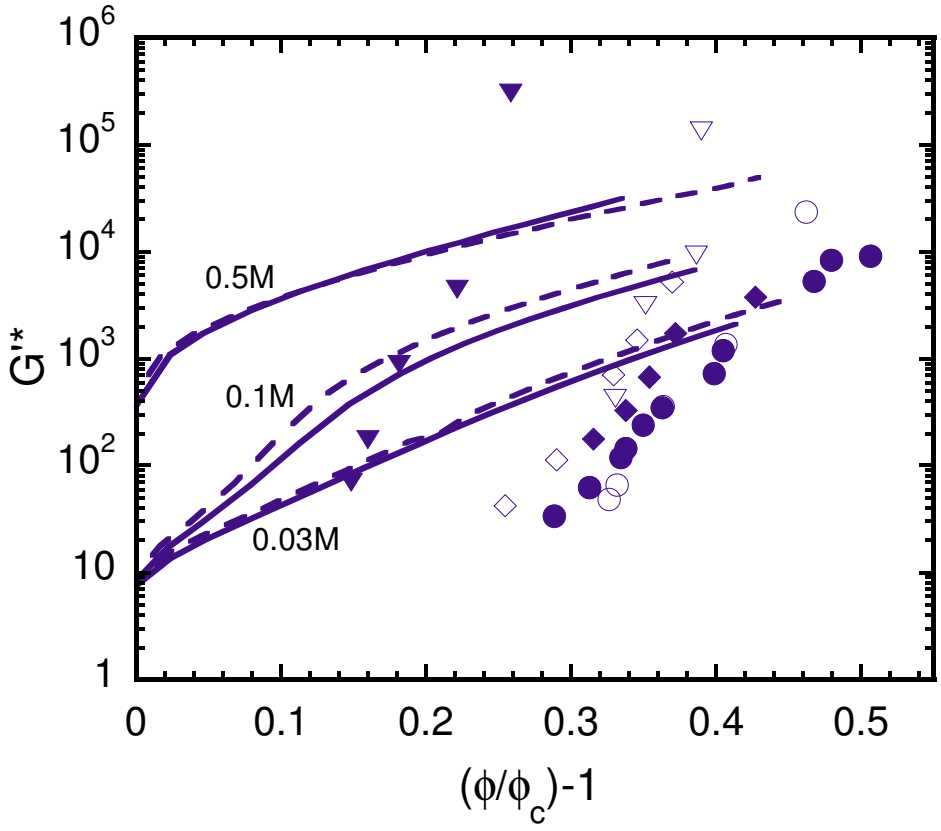

Figure 4.7. *G'** as a function of reduced volume fraction for spheres (closed points) and dicolloids (open points) at ionic strengths of 0.03 (circles), 0.1 (diamond), and 0.5M (triangles). Curves indicate nMCT predictions for *G'** for spheres (solid) and dicolloids (dash).

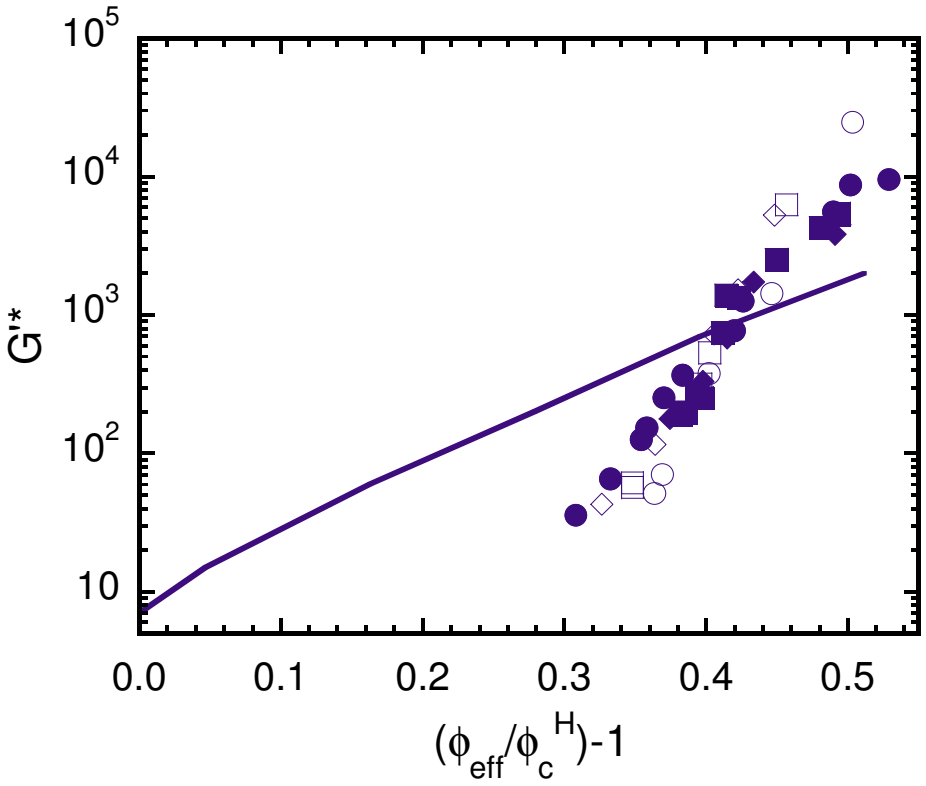

Figure 4.8. *G'** as a function of reduced *effective* volume fraction for only repulsive conditions: 0.03 (circles), 0.05M (squares), 0.1 (diamonds). All ionic strengths and particle shapes collapse onto a single universal curve. Hard particle theory is shown as a solid curve.

Ionic Strength (M)	B (k_BT)	κ (1/ Å)
0.03	79	0.06
0.05	32	0.07
0.1	14	0.08
0.3	3.6	0.093
0.5	1.1	0.1
1.0	<0.1	0.2

Table 4.1. Parameters used for Yukawa fits to electrostatic contribution to the particle interaction energies.

Ionic Strength (M)	ϕ_c S	ϕ_c sDC
0.03	0.410	0.454
0.05	0.427	0.472
0.1	0.440	0.487
0.3	0.456	0.503
0.5	0.449	0.462
1.0	0.419	0.412

Table 4.2. NLE nMCT calculations of ϕ_c for S and sDC

4.6 List of References

[1] Bianchi, E., J. Largo, P. Tartaglia, E. Zaccarelli, and F. Sciortino, *Phys. Rev. Lett.* **2006**, 97(16), 168301.

[2] Sciortino, F., E. Bianchi, J.F. Douglas, and P. Tartaglia, *J. Chem. Phys.*, **2007**, 126(19), 194903.

[3] Zhang, Z.L. and S.C. Glotzer, *Nano Lett.*, **2004**, 4(8), 1407.

[4] Glotzer, S.C. and M.J. Solomon, *Nat. Mat.*, **2007**, 6(7), 557.

[5] Dendukuri, D., K. Tsoi, T.A. Hatton, and P.S. Doyle, *Langmuir*, **2005**, 21(6), 2113.

[6] Fujibayashi, T. and M. Okubo, *Langmuir*, **2007**, 23(15), 7958.

[7] Kim, J.-W., R. Larsen, and D.A. Weitz, *Adv. Mat.*, **2007**, 19.

[8] Mock, E.B., H. De Bruyn, B. Hawkett, R. Gilbert, and C.F. Zukoski, *Langmuir*, **2006**, 22.

[9] Sheu, H., E.-A. M.;, and J. Vanderhoff, *J. Polym. Sci., Part A: Polym. Chem.*, **1990**, 28.

[10] Snoeks, E., A. van Blaaderen, T. van Dillen, C.M. van Kats, M.L. Brongersma, and A. Polman, *Adv. Mat.*, **2000**, 12(20), 1511.

[11] Yang, S.M., S.H. Kim, J.M. Lim, and G.R. Yi, *J. Mat. Chem.*, **2008**, 18(19), 2177.

[12] Zerrouki, D., B. Rotenberg, S. Abramson, J. Baudry, C. Goubault, F. Leal-Calderon, D.J. Pine, and M. Bibette, *Langmuir*, **2006**, 22(1), 57.

[13] Keville, K.M., E.I. Franses, and J.M. Caruthers, *J. Coll. Inter. Sci.*, **1991**, 144(1), 103.

[14] Chong, S.-H. and W. Götze, *Phys. Rev.*, **2002**, 65(4), 041503.

[15] Götze, W. and L. Sjörgen, *Rep. Prog. Phys*, **1992**, 55, 241.

[16] Chong, S.-H., A.J. Moreno, F. Sciortino, and W. Kob, *Phys. Rev. Lett.*, **2005**, 94, 215701.

[17] Yatsenko, G. and K.S. Schweizer, *J. Chem. Phys.*, **2007**, 126.

[18] Yatsenko, G. and K.S. Schweizer, *Phys. Rev. E*, **2007**, 76, 014505.

[19] Yatsenko, G. and K.S. Schweizer, *Langmuir*, **2008**, 24, 7474.

[20] Letz, M., R. Schilling, and A. Latz, *Phys. Rev. E*, **2000**, 62, 5173.

[21] DeMichelle, C., R. Schilling, and F. Sciortino, *Phys. Rev. Lett*, **2007**, 98, 265702.

[22] Donev, A., I. Cisse, D. Sachs, E.A. Variano, F.H. Stillinger, R. Connelly, S. Torquato, and P.M. Chaikin, *Science*, **2004**, 303(5660), 990-993.

[23] Williams, S.R. and A.P. Philipse, *Phys. Rev. E*, **2003**, 67, 051301.

[24] Schweizer, K.S., *Cur Opin. Coll. Inter. Sci.*, **2007**, 12, 297.

[25] Partridge, S.J., *Rheology of Cohesive Sediments*, in *Dept. of Physical Chemistry*. 1985, Bristol University.

[26] Mock, E.B. and C. Zukoski, *J. Rheol.*, **2007**, 51, 541.

[27] Krieger, I.M., *Adv. Coll. Inter. Sci.*, **1972**, 3(2), 111.

[28] Gopalakrishnan, V. and C.F. Zukoski, *Ind. Eng. Chem. Res.*, **2006**, 45(21), 6906.

[29] Schweizer, K.S. and E.J. Saltzman, *J. Chem. Phys.*, **2003**, 119(2), 1181-1196.

[30] Cheng, Z., J. Zhu, P.M. Chaikin, S.-E. Phan, and W.B. Russel, *Phys. Rev. E*, **2002**, 65(4), 041405.

Chapter 5 Nonlinear Rheology and Yielding in Dense Suspensions of Hard Anisotropic Colloids

5.1 Introduction

Over the past decade a deep understanding of the dynamics of dense suspensions of spherical colloidal particles has been developed.[1, 2] Of interest here are volume exclusion glasses that are observed on increasing volume fraction in suspensions of particles experiencing repulsive interactions that do not crystallize. Dense glassy and gelled systems have seen intense study due to their importance in a vast array of products including foams, slurries, pastes, inks, adhesives, emulsions, and granular assemblies.[3] Many advances in product formulation have been enabled through insights gained by studying model systems where particle size and strength of attraction can be controlled.[4] A great deal of work experimental has focused on changes in properties as glassy and gelled regions are approached where theories have been developed to predict volume fraction and strength of attraction dependence of relaxation times and linear storage/elastic and loss/viscous moduli.[5-12] The vast majority of this work has investigated uniform spherical particles.

At low applied stresses, for time scales shorter than those associated with the longest relaxation time of the system, soft glassy phases behave like a solid and store stress elastically. As the deformation of the glass is driven beyond a critical value of stress (strain), known as the yield stress, τ_y, (strain, γ_y), the suspension relaxes stress more rapidly until the suspension relaxation time is shorter than the experimental time and the system behaves like a viscous liquid.[3] In this chapter the focus is on suspension behavior at stresses near the yield point. Of particular interest is the onset of nonlinear behavior where glasses start to flow.

There are a variety of experimental methods used to characterize the onset of flow resulting in a variety of definitions of the yield stress and yield strain for the same suspension. Even for a given experimental set-up, these definitions give rise to different numerical values but typically show the same qualitative behavior as system parameters such as volume fraction are varied. For example, in the stress sweep experiments used here to characterize yielding, the sample is deformed with increasing stress (strain) at a fixed frequency. At low stresses (strains) the system responds in a linear manner thus showing linear storage and loss moduli, G_0' and G_0'' respectively. With further increases in stress the elastic modulus decreases and falls below the viscous modulus. For some systems with increasing stress, the loss modulus passes through a maximum. Based on stress (strain) sweep experiments of this type, three common definitions of yield are used[4, 5, 13]: i) The perturbative yield point is defined as the stress and corresponding strain the elastic modulus (G') falls to 90% of its low stress plateau value.[14] ii) An absolute yield point is defined as the point where $G'=G''=G_x$. At this point, using concepts of a Maxwell element, such the suspension relaxation time has decreased to below that of the experimentally imposed time scale. As a result, the stress (strain) where $G' = G''$ is taken as a yield point and has been used to compare experiments with predictions of absolute yield stress.[5] iii) A third definition of yielding is denoted by a maximum in G''.[13] At this point, the system is dissipating a maximum amount of energy.

For glassy suspensions of hard spherical particles, the low strain limiting elastic modulus and the yield stress tend to be power law or exponential functions of volume fraction,[4, 5, 14] while, for hard particles, yield strain can show decreasing

volume fraction dependence[14] or nonmonotonic behavior.[4, 5, 15] For these systems, regardless of the specific definition chosen to characterize it, there is a single yielding event. For low frequency strains (well away from those capable of inducing thickening), this is seen as a monotonic decay in *G'* and, at most, a single maximum in *G"* with increasing stress. Current understanding of this phenomenon relies on an Eyring-type approach where stress relaxation requires diffusion over an entropic barrier produced by nearest neighbor cages. This diffusive process occurs with a characteristic time of t_{hop}. Deformation of the suspension lowers the barrier to nearest neighbor exchange thus making t_{hop} a function of strain. Yielding is associated with deformations that reduce t_{hop} to close to the experimental deformation time.[4, 5, 13-15] For hard particles there is a single caging constraint that must be overcome to relax stress and give rise to fluid-like mechanical behavior.

Changing particle shape increases the degrees of freedom of movement. In addition to translational (center-of-mass, CM) movement, rotational motion can also relax stress. This has been demonstrated theoretically using MCT for anisotropically shaped molecules.[16-21] More recently Zhang and Schweizer showed multiple glassy states are predicted for uniaxial dicolloid particles.[22] The nonlinear Langevin (NLE), naïve Mode Coupling Theory (nMCT) predicts three distinct states: an ergodic fluid where neither CM or rotational movement are frozen, a plastic glass state where CM movement is localized, but particles are still free to rotate, and a double glass where both types of movement are localized. The onset of localization is determined by solving a coupled equation for the localization length, r_{loc}, and localization angle θ_{loc} using equilibrium microstructural information as input.[22] In the double glass region,

at small aspect ratios, there is a decoupling of rotational and translational motion with a lower entropic barrier for rotation than for center of mass motion. As the aspect ratio increases there is a stronger coupling between rotational and center of mass motion.

The prediction of multiple glassy states leads to the exploration of how these confinements are broken as the system of anisotropic particles experiences stress. The transition from single to double glasses in the above theoretical predications is expected to accompany the development of a second mechanism for relieving stress and thus transitions from single yield to double yield events are expected as shape and volume fraction is changed.

In this chapter, an experimental system is described where uniform, nonspherical colloid particles are synthesized and suspensions are prepared resulting in nearly hard pair potentials. Using NLE nMCT as a guide, the initiation of nonlinear mechanical behavior of glassy systems is explored and properties are compare with those seen for spheres experiencing similar pair potentials. In Section 5.2, particle synthesis and preparation techniques is described as well as experimental procedures and equipment. In Section 5.3.1, results are shown from dynamic stress sweep experiments and evidence is compared for multiple yielding to predicted double glass state diagrams from the literature.[16-22] Section 5.3.2. investigates yield stresses and strains defined at G_x compares these to theoretical predictions from NLE nMCT for hard spheres. Also in this section, shape-independent, universal behavior is sought through previously successful volume fraction scaling methods.[23, 24] Finally in

Section 5.4, the findings are summarized and conclusions are offered about the influence of shape on the mechanisms of stress relief.

5.2 Experimental

The particles used in the experiments discussed here are synthesized in four distinct, monodispersed shapes: sphere (S), heterdicolloid (hDC), symmetric homodicolloid (sDC), and tricolloid (TC). Particles in the size range of D=250-350nm are synthesized using a multi-step emulsion polymerization technique developed by Mock and coworkers[25] and described in more detail in ref [23]. SEM images of the particles can be seen in Figure 5.1 (a-d). To make comparisons to the previously mentioned nMCT predictions for symmetric dicolloids, approximate aspect ratios (L/D) for S, hDC, and sDC particles are measured using SEM images. These particles are found to have aspect ratios of 1.0, 1.15, and 1.31 respectively.

The particles are stabilized with the adsorption of a nonionic surfactant [$C_{12}E_6$] to the surface and suspended in an aqueous solution of NaCl at a concentration of 0.03M. The surface charge of the particles is measured with electrophoresis and is constant (within experimental error) for each shape at a given ionic strength. The combination of electrostatic charge and van der Waals forces give the full particle interaction energies as described in ref [23]. At 0.03M ionic strength, the particles behave as if they are experiencing effectively hard interactions. An effective particle volume fraction is used that accounts for the effects of surface charges, $\phi_{eff}=\phi[(D+\Delta)/D]^3$ where Δ is the increase to the particle diameter due to the

effects of the electrostatic double layer. Table 5.1 summarizes the parameters used in determination of ϕ_{eff}.

SEM micrographs of the particles were taken using a Hitachi S4700 instrument. One drop of the as-synthesized suspension was placed on a Formvar coated copper grid and attached to a sample holder using conductive tape. Particle dimensions were determined by measuring 50-100 particles from SEM images and confirmed with dynamic light scattering with a bench-top FOQELS DLS instrument.

After synthesis, particles are cleaned and concentrated to ϕ~0.35 with dialysis against deionized water. $C_{12}E_6$ and a concentrated solution of aqueous NaCl (0.1M) is then added to the particle suspension such that the final surfactant concentration is 0.03M (sufficient for monolayer coverage[7]) and the final solvent ionic strength is 0.03M as well . The suspensions are then concentrated further with centrifugation (at ~4000g) until no supernatant can be removed. The highly concentrated suspension remaining in the centrifuge tube becomes the highest volume fraction sample for a given particle shape and is subsequently diluted to obtain lower volume fractions at that condition.

To perform rheological experiments, ~3.2mL of sample is removed from the centrifuge tube and transferred to the cup of a cup-and-bob geometry Bohlin constant stress C-VOR rheometer equipped with a roughed titanium bob. A small portion of the sample in the cup is then removed and the wet and dry weight is measured to obtain the sample volume fraction. The samples undergo an oscillatory stress sweep from ~0.01-1000Pa at a frequency of 1Hz, where the viscous and elastic moduli are measured. Each data point has an integration time of 4s.

In order to compare suspensions of different particle shapes, stress and modulus are nondimensionalized with k_BT and a measure of the particle volume, V^* such that stress $\tau^*=\tau V^*/k_BT$ and $G'^*=G'V^*/k_BT$. The definitions of V^* are as follows: S – D^3, hDC – LD^2, sDC – L^2D, TC – bhD where L=longest axis length, D=short axis length or sphere diameter, and b and h=base and height of an inscribing triangle. Each of these dimensions include the core particle and Δ.

5.3 Results and Discussion

5.3.1 Multiple yielding

Dynamic strain sweep experiments for each of the four particle shapes at an ionic strength of 0.03M are shown in Figures 5.2 (a-d). Here two representative volume fractions are shown (one high, one low) for shapes S, sDC, and TC while for hDC three volume fractions are shown. For suspensions containing spheres, typical hard-sphere-like behavior is seen with $G'^*>G''^*$ at low strains, a decrease in G'^* as strain is increased, a single maximum in G''^* near a strain of 1-10% (i.e 0.01-0.1), a G'^*-G''^* crossover occurring near the maximum in G''^*, and finally terminal flow with $G'^*\sim\dot{\gamma}^{-1.3}$ and $G''^*\sim\dot{\gamma}^{-0.6}$. This is consistent with previous experimental systems.[5, 13, 26] At low volume fractions, hDC suspensions show a single, relatively small G''^* peak at ~5% strain and $G'^*=G''^*$ occurs far beyond the peak, at ~30% strain. For intermediate volume fractions, two G''^* peaks develop. One occurs at a strain of ~3% and the other at a strain of ~30% while $G'^*=G''^*$ occurs at an intermediate strain near 20%. At the highest volume fractions, again only one G''^* peak is seen. However it is much larger and broader than the low volume fraction

single peak indicating that the two intermediate volume fraction peaks may have merged into one single peak at this particle density. For sDC suspensions a G''^* peak at strains of ~40% is seen and $G'^*=G''^*$ just below this peak, at strains of ~10-30%. For the highest volume fraction, there is also a low strain G''^* peak at 1-3%. Unfortunately the data does not allow determination of a similar peak at the low volume fraction because the first data point is ~1% strain. The lowest strain data point has a higher value of G''^* than the next point indicating the possibility of a peak in the strain range <2%. TC suspensions exhibit unique behavior where a minimum in G'^* is seen and G''^* remains roughly constant until a large peak at high strains ~ 100%. The G'^*-G''^* crossover occurs near the minimum in G'^* at a strain of ~20% for these suspensions.

In the Figures 5.3 (a-d) and 5.4 (a-d), G'^* and G''^* are shown as functions of reduced dimensionless stress, τ^* where G'^*, G''^* and τ^* have scaled on the plateau values $G_0'^*$ $G_0''^*$and $G_0'^*$ respectively. This is done to deemphasize the shifts in absolute stress as volume fraction is increased by using the plateau modulus as characteristic stress of the system. The insets of Figure 5.3 shows $G_0'^*$ and $G_0''^*$ as a function of volume fraction for each shape. These insets also indicate volume fractions where the suspensions start to show glassy behavior ($G_0'^* > G_0''^*$) at a deformation frequency of 1Hz. Below experimental glass transition is defined as the volume fraction where $G_0'^*= G_0''^*$ as determined by a cross over point found using exponential fits to the modulus data shown in the inserts. This extrapolation is shown in the inset in Figure 5.3a.

A quick glance at the data in these figures demonstrates that there are sometimes multiple maxima in G''^* and inflection points in G'^* and that their positions change with volume fraction and particle type. The complex shape of $G'^*(\tau^*)$ and $G''^*(\tau^*)$ compared to hard sphere systems suggests that multiple escape events exist for suspensions of anisotropic particles.

The presence of two constraints limiting rapid stress relaxation in suspensions of hard particles can be understood from the theoretical studies using MCT and nMCT suggesting that anisotropic hard particles can become localized in two distinct ways. First the centers of particle mass can become localized by caging of nearest neighbors. For small degrees of anisotropy, this first occurs at volume fractions where the particles remain free to rotate within their cages. As volume fraction is raised a double glass region is entered where the particle angular orientation becomes localized. Typical CM localization lengths, r_{loc}, are 10% of a particle size and decreases as volume fraction is increased. For particles with an L/D on the order of the hDC system, the initial angular localization is on the order of 75°. As the aspect ratio of the particles is increased, particles' centers of mass are localized at higher volume fraction while the volume fraction of angular localization decreases. These lines cross at an $L/D \sim 1.4$ where, for larger anisotropy, localization both centers of mass and angular localization are predicted to occur at the same volume fraction.[22] As discussed below, there is qualitative agreement between these predictions and experimental observations.

For S particle suspensions, the drop in G'^* is sudden and smooth and is accompanied by only one maximum in G''^* occurring at a reduced stress ~0.01-0.03.

In the theoretical framework of NLE-NMCT, yielding in glassy spherical particle suspensions occurs at the stress required to overcome the CM localization barrier which occurs at 1-3% of the characteristic stress of the system.

For the anisotropic particles, more complex yielding behavior is seen. For example, the hDC particles show a single maximum in G''^* at τ^*~(0.05-0.1)$G'_0{}^*$ at the three lowest volume fractions. This behavior suggests that the particles are constrained by a dynamic potential requiring a stress of magnitude (0.05-0.10)$G'_0{}^*$ to lower the entropic barrier such that stress is relaxed on a time scale of ~2π s. The stress at the maximums in G''^* for the hDC are larger than those observed in suspensions of spheres. As volume fraction is increased, two peaks in G'' are observed (these samples are shown in darker orange in Figures 3b and 4b). The first peak is seen near a $\tau^*/G_0'^*$ ~ of 0.02 and a second near $\tau^*/G_0'^*$ ~ 0.06. At the same volume fractions a shoulder is seen to grow in the decay of G'^* with increasing stress. This behavior as indicating that there are two barriers to relaxing stress in this system and these are observable for ~0.65 < ϕ < ~0.67. These two peaks are interpreted as resulting from a low barrier to rotational motion and a higher barrier to center of mass motion.[9] As volume fraction is increased above ~0.67, the two peaks appear to merge into a single large, broad peak. The reemergence of a single peak is consistent with a strong coupling between rotational and CM confinement at these high particle densities.

For sDC particles, all volume fractions exhibit a high stress G''^* maximum that shifts to lower stress with increasing volume fraction. At the lowest particle density, this peak occurs at a τ^*~ $0.5G'_0{}^*$ and moves to $0.05G'_0{}^*$ at the highest

volume fraction. While a low stress maximum for G''^* is not observed for all samples (only the highest two volume fractions), there are indications of a minimum in G''^* at lower stresses and a roll off in G'^* at a stress of ~0.01G'^*_0. These observations suggest that stress sweep experiments probe two yielding events for all volume fractions of sDC particles studied. Again, the first yielding event is associated with breaking rotational motion entropic barriers and the second with overcoming entropic barriers for CM motion. The results suggest that that dimensionless yield stress producing CM motion is larger for hDC than sDC. This observation is consistent with the work of Zhang and Schweizer[22] who predict an increasing entropic barrier to CM diffusion with increasing aspect ratio.

The TC particle suspensions display unique behavior. One maximum is observed in G''^* which occurs at stresses near (0.5-1)G'^*_0. After a yield event at low stress, there is a dramatic maximum in G'^* not observed with other particle shapes. The maximum in G'^* also occurs at stresses of (0.5-1)G'^*_0. There may be hints of a minimum in G''^* at low stress but these are in the limit of instrumental resolution and confirmation would require additional work. The maxima in G'^*_0 and G''^*_0 indicate a dynamic stress thickening occurring at stresses well below those expected for spheres of equal size, although the extremely high volume fractions of these samples should be noted.[27]

To conclude this section, in Figure 5.5 a yielding state diagram is presented summarizing the above findings. Spherical particles only show a single yielding event for all volume fractions above the kinetic glass transition.[23] Suspensions heterogeneous dicolloids first show a single yield event, then two, and finally a board

single event as volume fraction is increased. Double yielding is observed in suspensions of for homogeneous dicolloids for all volume factions above the kinetic glass transition, while TC suspensions demonstrate behavior that is distinct from dicolloid shapes.

5.3.2. Yield stress, strain, and modulus

Stress sweep experiments described above show evidence for multiple yielding events depending on volume fraction and particle shape. These events are probed due to the imposed oscillatory motion. The choice is made to discuss modulus maxima in terms of stress as opposed to strain to be consistent with interpretations of stress lowering entropic barriers and enabling diffusion to relax imposed stresses. A distinct method to probe yielding in these suspensions is to define the absolute yield point as the intersection of G'^* and G''^* (i.e., the stress (strain) where $G'^*=G''^*=G_x^*$).[5] In all suspensions studied here, this provides a single yield stress τ_y^*, and yield strain γ_y, enabling comparisons the results with those of Anderson and Zukoski's experimental work with hard spheres (also at 1Hz), the hard sphere experiments of Petekidis et al.[15] and of Pham et al.[13] as well as the NLE NMCT theory from Kobelev and Schweizer.[4] Returning to Figure 5.2 one can see that for S suspensions, G_x^* occurs near or just after the maximum in G''^*. For hDC particle suspensions, G_x^* occurs at slightly higher stress than the single G''^* peaks or between double peaks. Suspensions of sDC particles also have a G_x^* point between double peaks (and also near G''^* minimums if two peaks cannot be observed). Finally, for TC suspensions, G_x^* is seen near the G'^* minimum and at the beginning

of the rise in G''^*. Thus while τ_y^* indicates a transition from a predominantly elastic response to a predominantly lossy response to an imposed strain, it is clear that for $\tau^* > \tau_y^*$, in oscillatory experiments, the suspension's mechanical response remains sensitive to microstructural rearrangements and activation of different stress relaxation mechanisms. The power of exploring the shape and volume fraction dependence of stresses and strains at G_x^* lies in the ability to compare events at this unique cross over point from primarily elastic to primarily viscous response.

The volume fraction dependence of yield stresses for different particle shapes is shown in Figure 5.6. Yield stress increases exponentially with volume fraction for each shape in the form $\tau_y^* \sim Ae^{b\phi}$. The value of A varies from 10^{-13}-10^{-20} and b is approximately constant with a value of ~60-70. Also plotted in Fig 5.5 are data of Anderson and Zukoski showing similar qualitative behavior.[4]

Recently work explored the effects of shape on the low shear modulus for repulsive anisotropic particle systems and found that the differences could be explained in terms of a volume fraction parameter (ϕ^*) that relates the measured volume fraction to a shape-dependent maximum packing fraction or Random Close Packing (RCP) value defined as $\phi^* = 1/(\phi_{RCP} - \phi)$, where ϕ_{RCP} = 0.66 (S), 0.70 (hDC), 0.72 (sDC), and 0.73 (TC).[23] When volume fraction is rescaled in this manner, the $G_0'^*$ measured for different shapes collapse onto a single curve. Using the above values of ϕ_{RCP} (except as noted below), a similar analysis is done with yield stress and is shown in Figure 5.7. Reasonable collapse is seen indicating that at a fixed volume fraction, τ_y^* is dominated by packing efficiency as described in ref [23].

In addition to yield stress, yield strain and the yield modulus are compared with literature value of hard spheres. In Figure 5.8, yield strain for each particle shape is plotted along with data from Anderson and Zukoski[5], Petekedis et al.[15], and of Pham et al.[13], as well as the NMCT calculations from Kobelev and Schweizer.[4] Each experimental system of spherical particles shows similar qualitative nonmonotonic behavior. Yield strains reach a maximum near a volume fraction of 0.60-0.61. Theoretical calculations also show nonmonotonic behavior, but the maximum occurs at a lower volume fraction. Suspensions of heterodicolloids also show a maximum yield strain which occurs at a volume fraction near 0.66 while suspensions of sDC and TC do not show a clear maximum yield strain. Yatsenko and Schweizer predicted that for sDC particles of similar aspect ratio to those in this work, the maximum in yield strain occurs at the same distance from the shape-dependent onset of localization (i.e. ϕ/ϕ_c-1=0.15) and the values of yield strain decreases with increasing aspect ratio for sDC particles.[28] The results illustrated here however show that the yield strain appears to increase with larger aspect ratio dicolloids.

Nonmonotonic yield strains with increasing volume fraction can be understood as resulting from different volume fraction dependencies of yield stress (which is a measure of the entropic barrier height of the dynamic potential) and modulus which probes the curvature of the dynamic potential its minimum. Subtle variations in these parameters with volume fraction give rise to variations to changes in yield strain.[4] The results suggest that strains at yielding tend to increase with increasing (but still small) particle anisotropy.

In Figure 5.9, G_x^* is plotted as a function of volume fraction. The volume fraction dependencies of $G_0'^*$ and G_x^* are similar for all particle shapes. Theoretical predictions of $G_0'^*$ show a much weaker volume fraction dependence that is observed experimentally The difference in the magnitude of G_x^* between these experimental results and those of Anderson and Zukoski could be explained by noting that here the work is done at a higher dimensionless frequency due to the larger size of the particles. Finally, Figure 5.10 shows a similar collapse of G_x^* using the volume fraction scaling based on the distance from ϕ_{RCP} as described above for τ_y^* and as observed for $G_0'^*$.

In previous work, the collapse of linear elastic moduli with ϕ^* was explained by the relationship between modulus and the contact value of the pair distribution function which diverges for spheres as $1/(\phi_{RCP}-\phi)$.[23] Note that the G_x^* is a measure of energy storage (loss) at a microstructural deformation well outside the linear range where one might expect substantial changes in values of the pair distribution function at contact. The collapse of G_x^* data for different shapes with ϕ^* suggests an underlying connection between yielding and equilibrium properties as captured in the model of Kobelev and Schweizer[4]. Note that the flattening of the curves at high values of ϕ^* may be indicative of other physical phenomena such a slip at the suspension rheometer tool interface or a failure of the effective hard interaction energy at volume fractions so close to random close packing.

5.4 Conclusion

Here it has been demonstrated that shape anisotropy of particles experiencing volume exclusion interactions can lead to multiple yielding events in the stress relaxation of glassy suspensions. These constraints were probed by working with particles that are rendered effectively hard through the adsorption of a stabilizing surfactant layer and the manipulation of solvent ionic strength. Particle shape is found to have a profound influence on the mechanisms of stress relief. Spherical particles display only one constraint for stress relaxation. Anisotropic particles relieve stress through center of mass as well as rotational motions. Newly developed NLE nMCT predictions for multiple glassy states offers insight into the conditions multiple yielding events might be observed for symmetric dicolloid particles.

The absolute yielding of these suspensions, as defined by the point where *G'=G"*, is also influenced by particle shape. The yield stress is found to correlate with the distance from maximum packing similar to $G_0'^*$.[23] Yield strains show nonmonotonic behavior with volume fraction, which for spheres is consistent with previous studies. As shape anisotropy is increased, the relation between yield strain and volume fraction becomes less clear. The modulus at the yield point follows similar behavior to the yield stress and qualitatively matches previous experimental results with both showing a divergence at a shape dependent volume fraction of random close packing.

5.5 Figures and Tables

Δ_{surf}	Δ_{elect}	Δ_{total}
8nm	6	14

Table 5.1. Increase to particle diameter, from surfactant layer and electrostatic double layer, used to determine effective volume fraction.

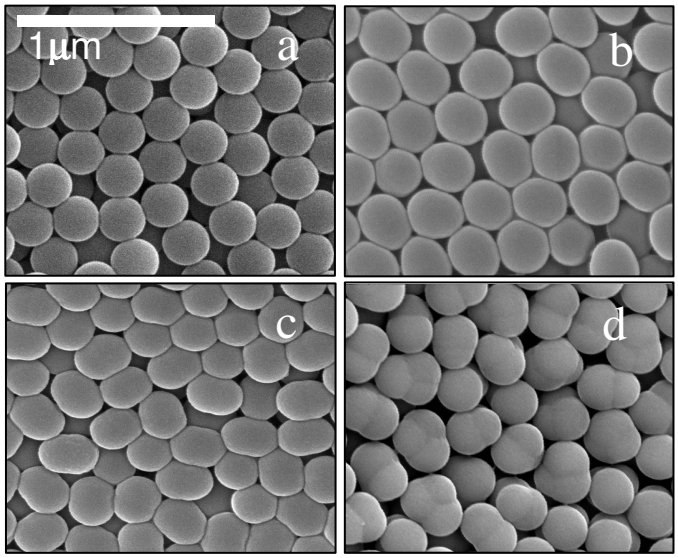

Figure 5.1. SEM images of the four particle shapes: S (a), hDC (b), sDC (c), TC (d)

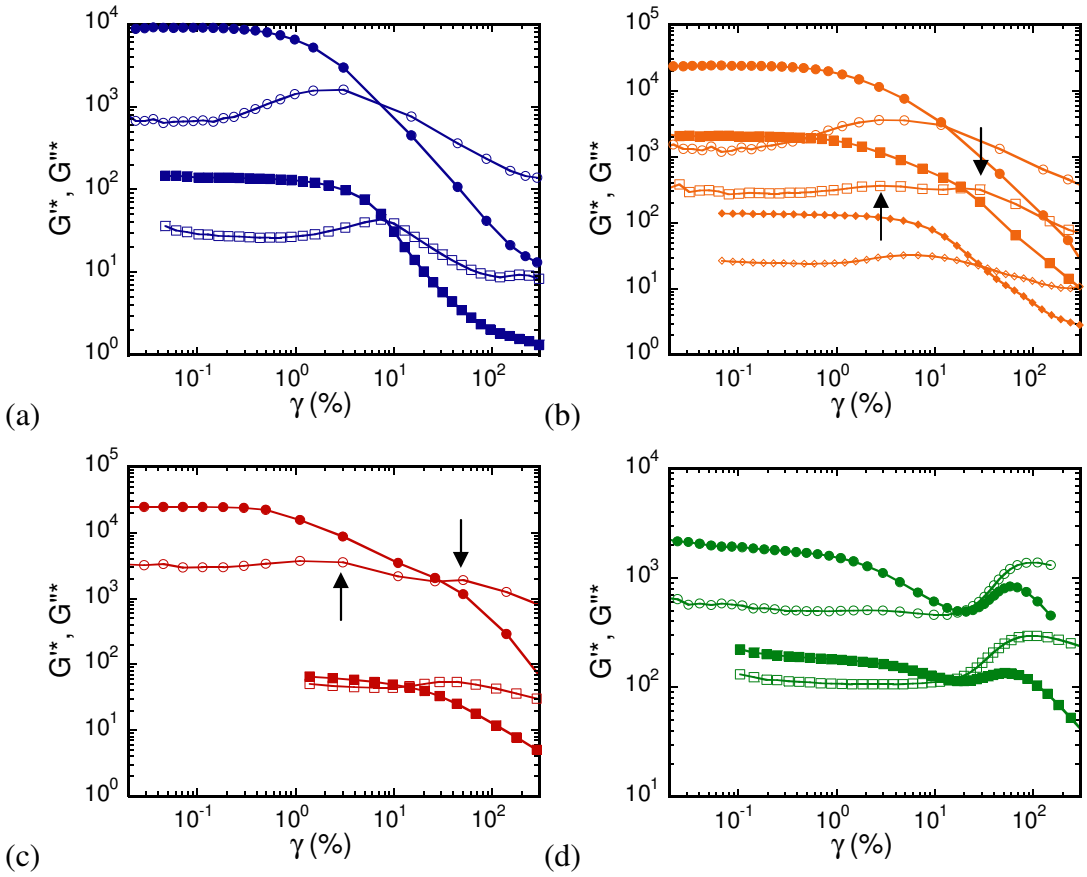

Figure 5.2. Dynamic strains sweeps for 2-3 representative volume fractions. *G'** are solid points, *G"** are open points. S (panel a, blue) at ϕ_{eff}=0.655 (circles) and 0.580 (squares). hDC (panel b, orange) at ϕ_{eff}=0.678 (circles), 0.655 (squares), and 0.614 (diamonds). sDC (panel c, red) at ϕ_{eff}=0.704 (circles) and 0.638 (squares). TC at ϕ_{eff}=0.685 (circles) and 0.661 (squares). Arrows indicate location of two peaks for *G"**.

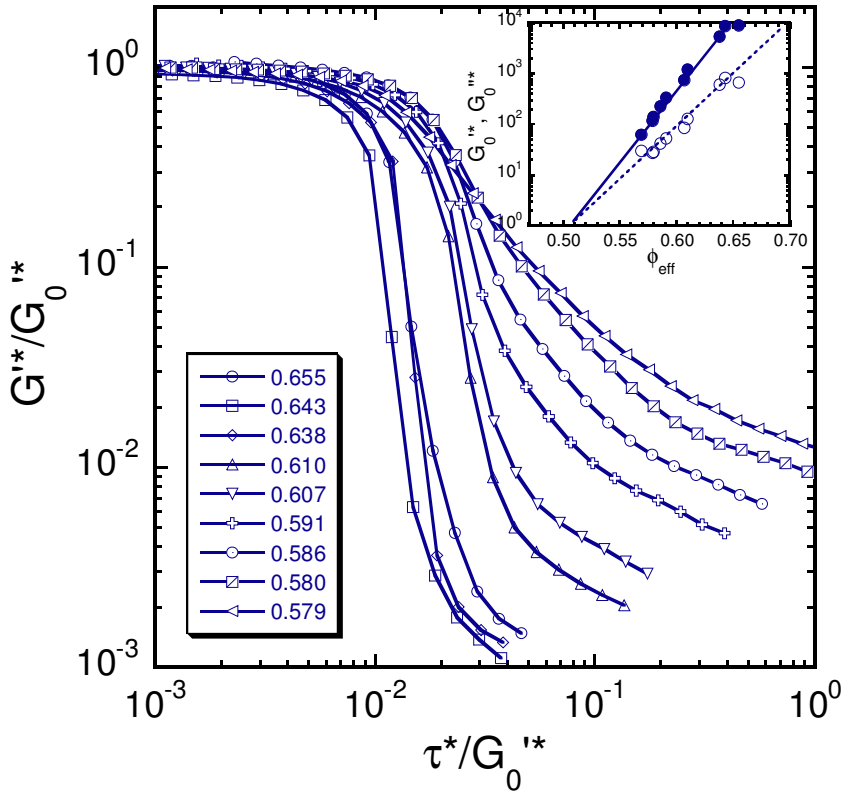

(a)

Figure 5.3 (continued on next page)

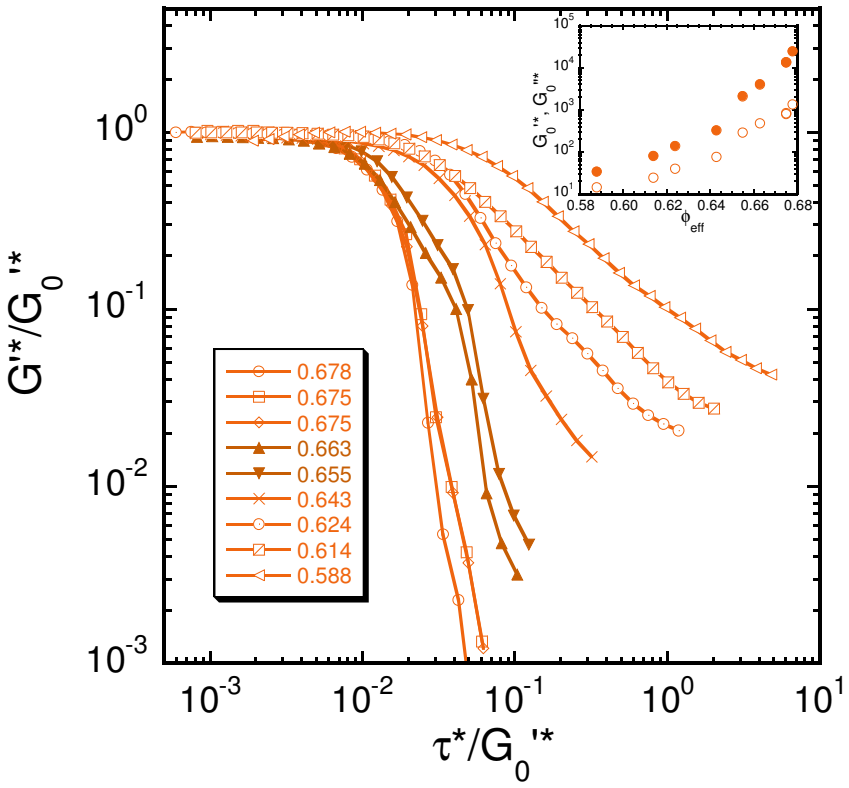

(b)

Figure 5.3 (continued on next page)

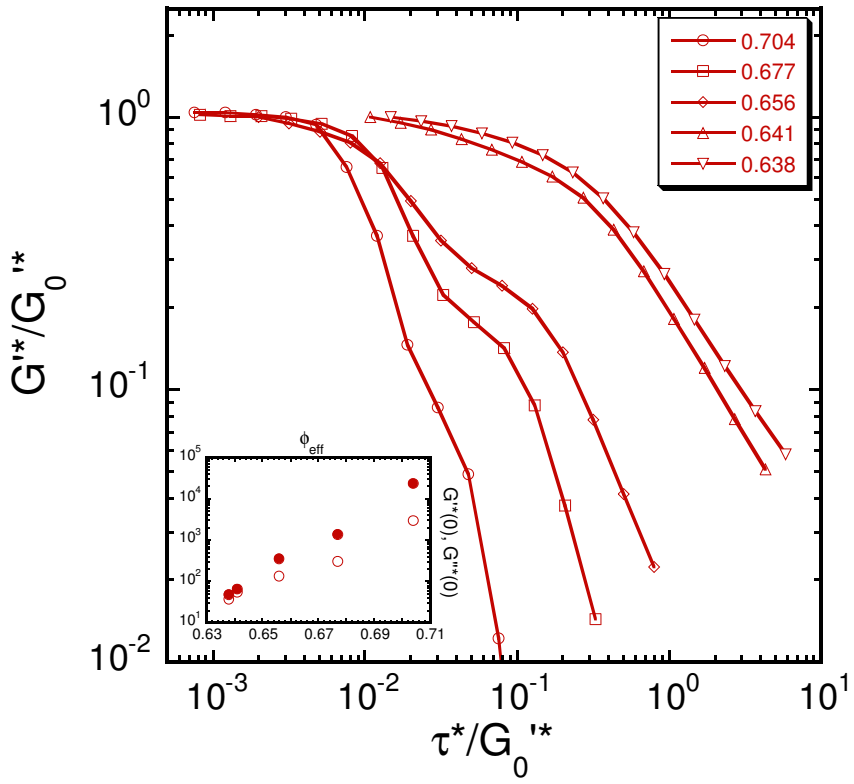

(c)

Figure 5.3 (continued on next page)

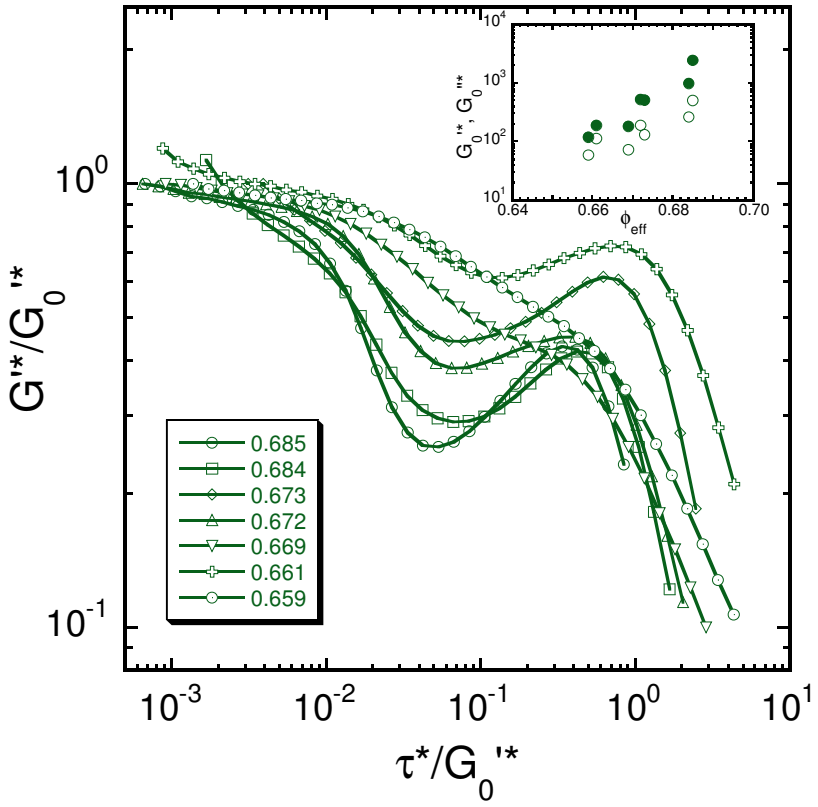

(d)

Figure 5.3. Dynamic stress sweeps showing $G'^*/G_0'^*$ as a function of reduced stress for S (a), hDC (b), sDC (c) and TC (d). (inset) $G_0'^*$, $G_0''^*$ for each particle shape as functions of effective volume fraction. Solid points are $G_0'^*$ and open points are $G_0''^*$.

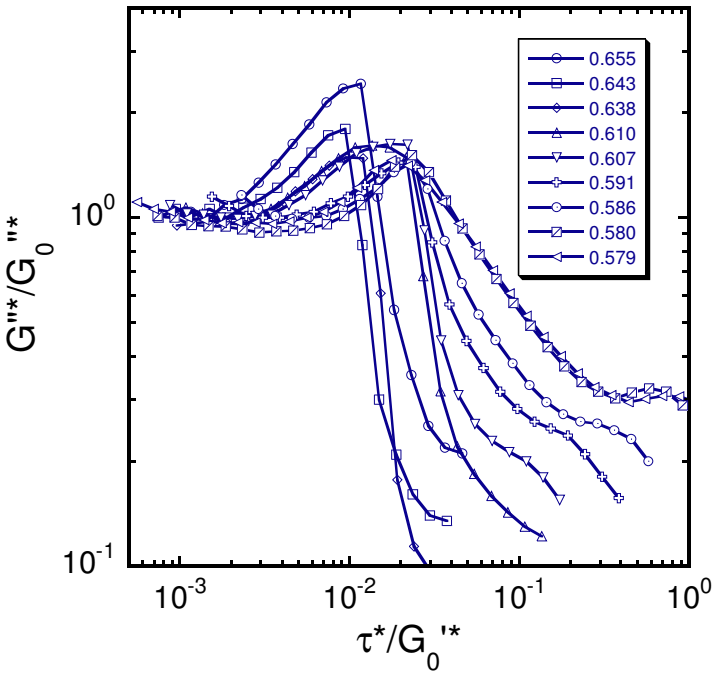

(a)

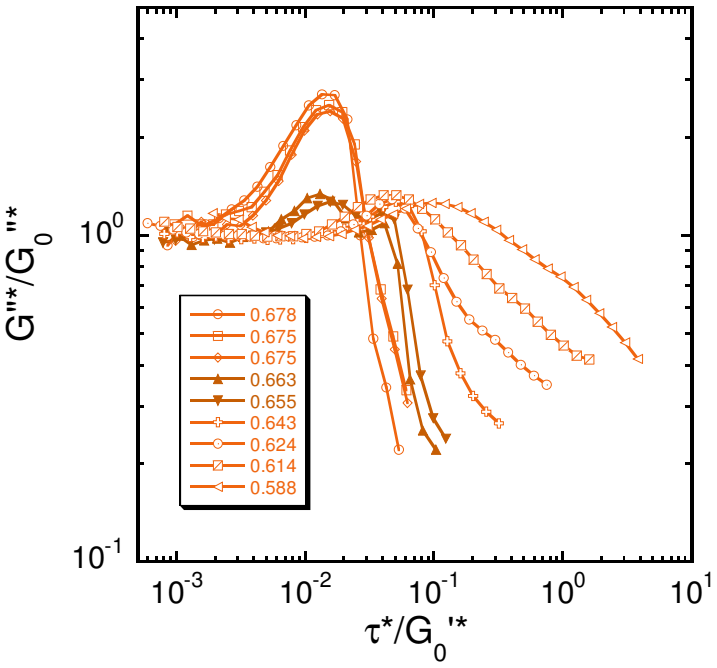

(b)

Figure 5.4 (continued on next page)

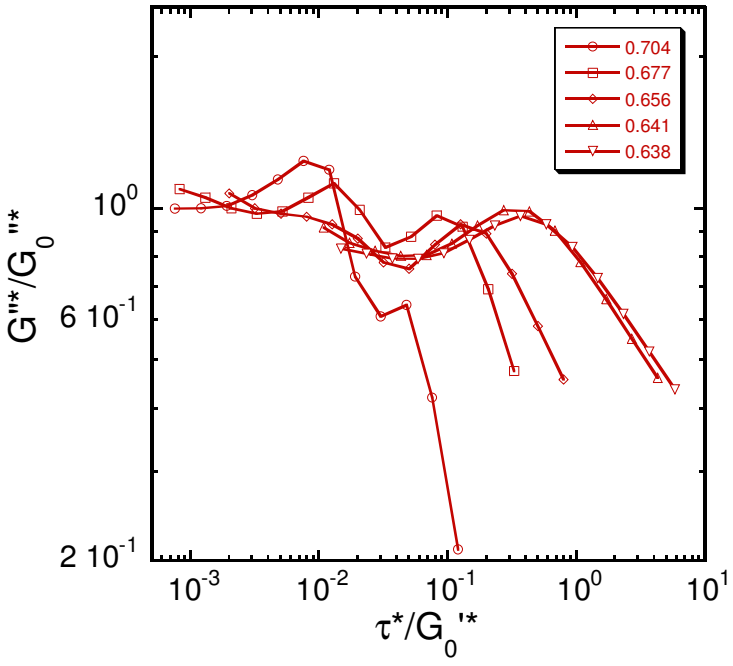

(c)

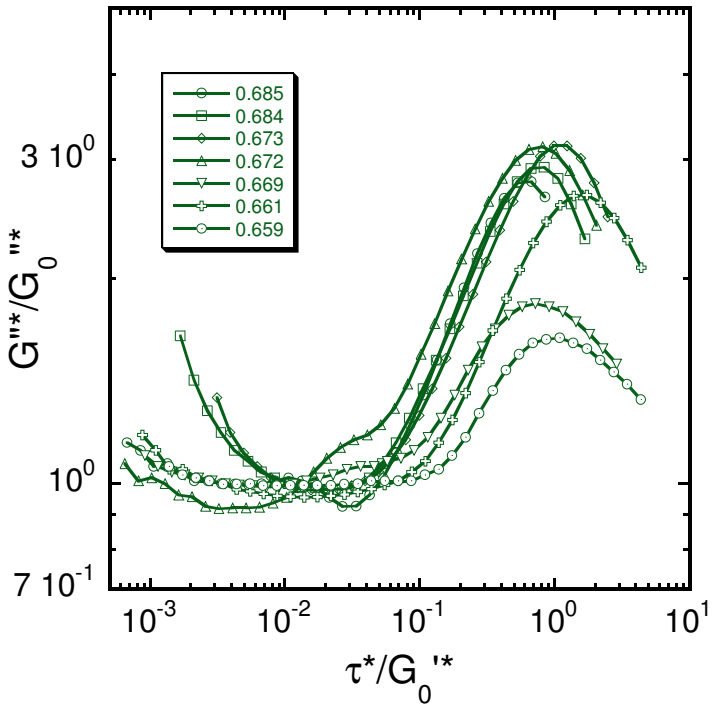

(d)

Figure 5.4. Dynamic strain sweeps showing *G"*/G₀"** as a function of reduced stress for S (a), hDC (b), sDC (c) and TC (d)

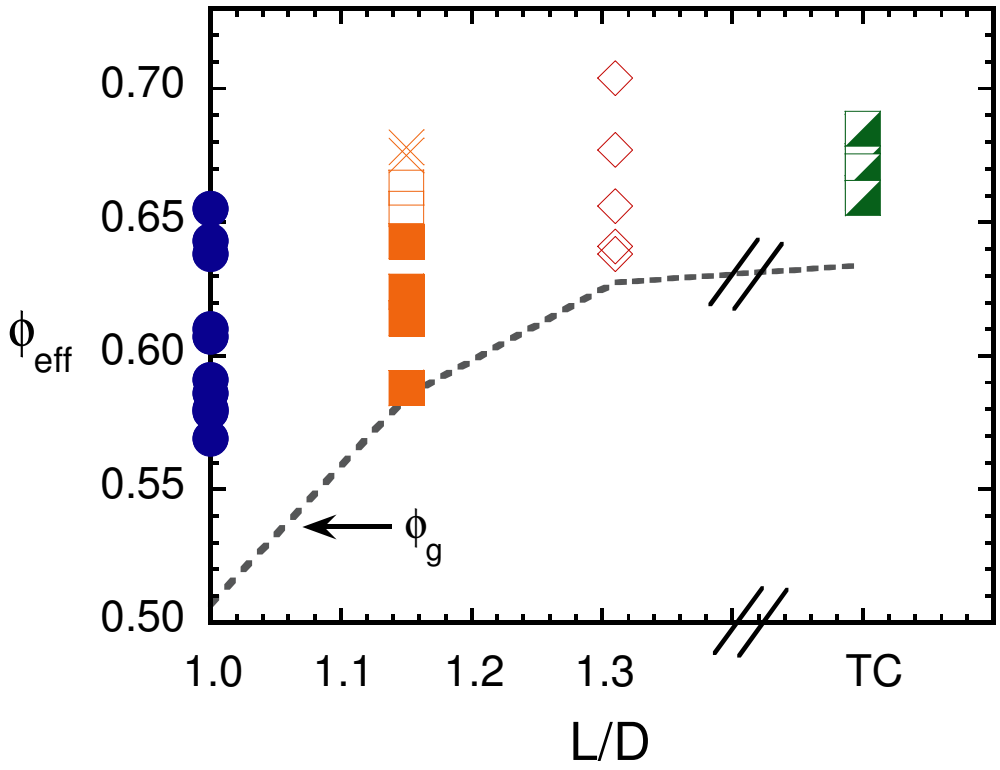

Figure 5.5. "Double yielding" state diagram showing single yielding samples (closed points), and double yielding (open points). S are shown in blue, hDC in orange, and sDC in red. "X" points indicate a return of single yielding samples for hDC at high volume fraction. TC samples are also shown in the figure separate from other shapes. TC particle suspensions exhibit unique yielding behavior not consistent with either single or double yielding dicolloids.

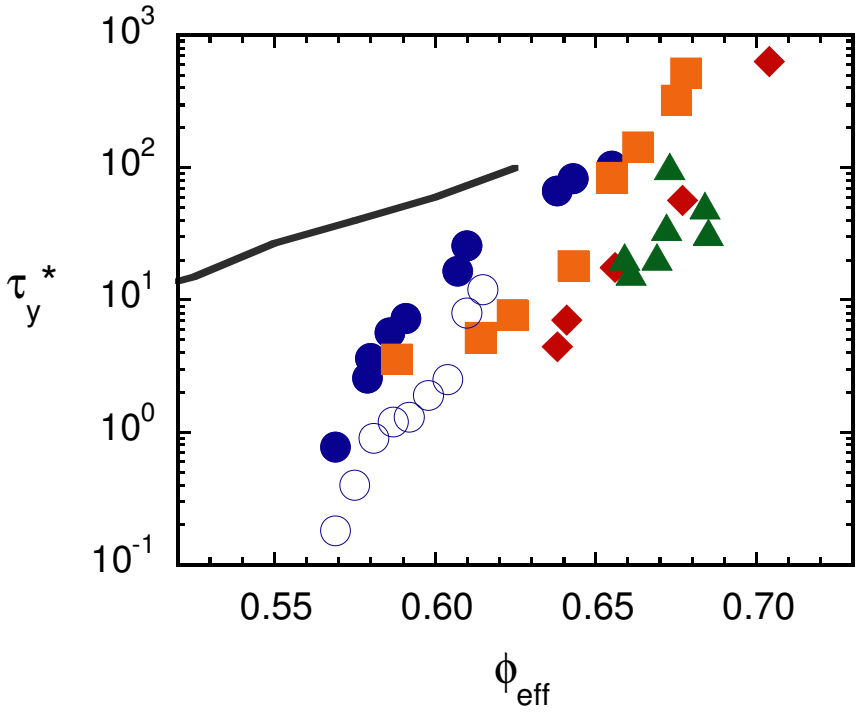

Figure 5.6. Dimensionless absolute yield stress (τ_y^*) as a function of effective volume fraction for all particle shapes: S (blue), hDC (orange), sDC (red), TC (green). Hard Sphere data from ref [5] shown with open blue circles. Grey curve indicates NMCT predictions from ref.[4]

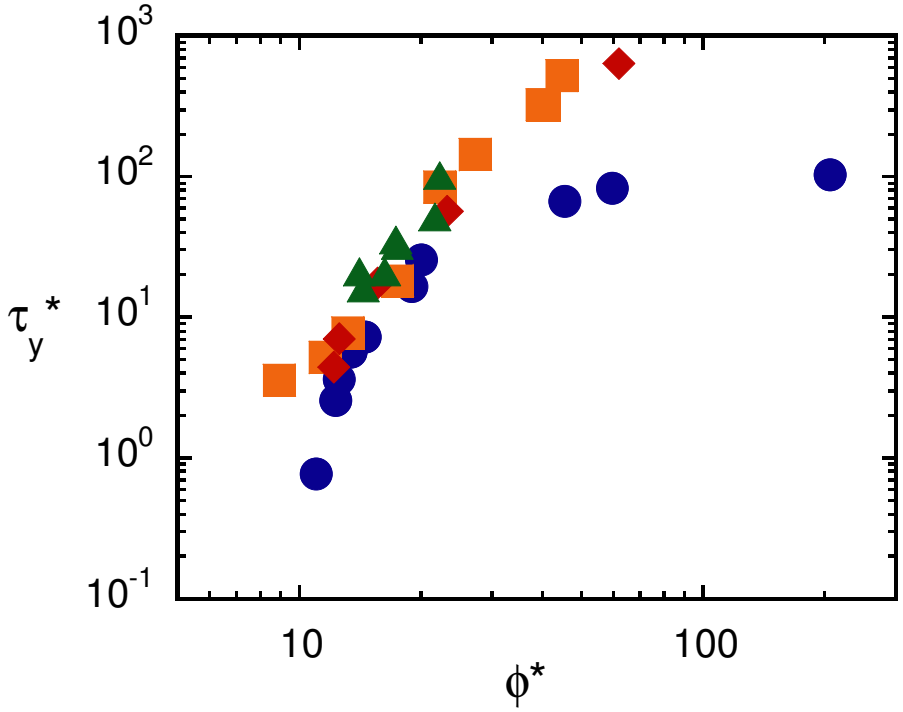

Figure 5.7. Yield stress as a function of ϕ^*. S (blue), hDC (orange), sDC (red) and TC (green) data collapses onto a single curve when volume fraction is rescaled as ϕ^*.

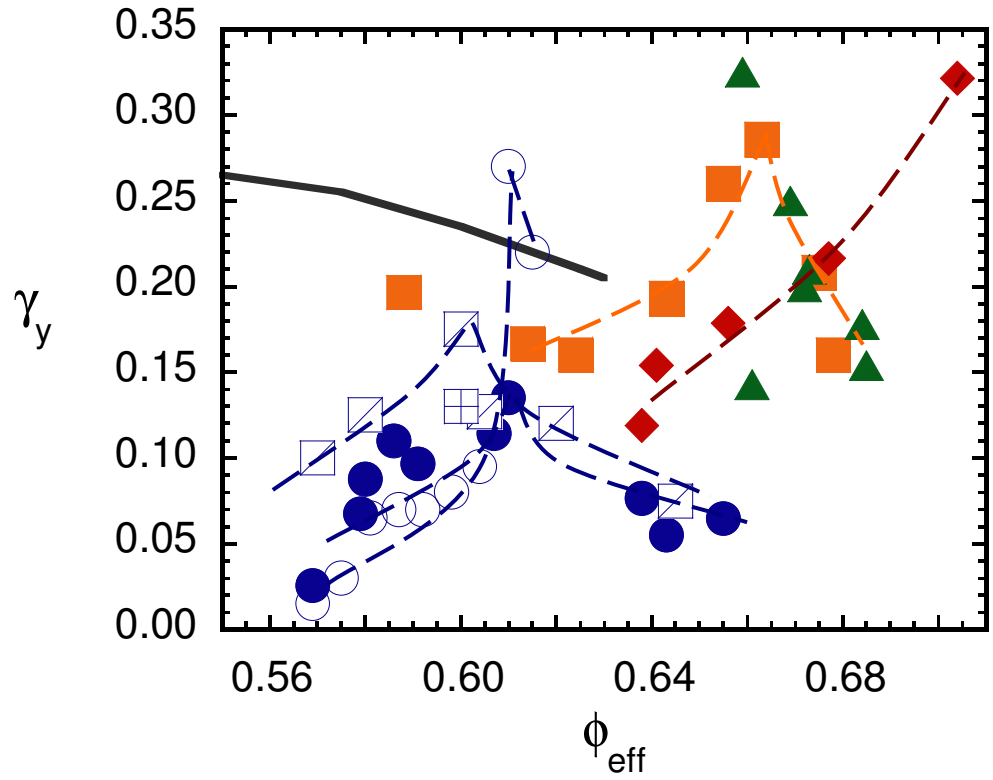

Figure 5.8. Absolute yield strains (γ_y) for S (blue), hDC (orange), sDC (red), and TC (green). Also shown are NLE NMCT predictions from ref [4] (solid grey curve), experimental data from ref [5] (open circles), from ref [15] (open squares with diagonal line) and one point from ref [13] (open squares with plus). Dashed curves are drawn to guide the eye to the maximums yield strains for S, hDC and sDC suspensions.

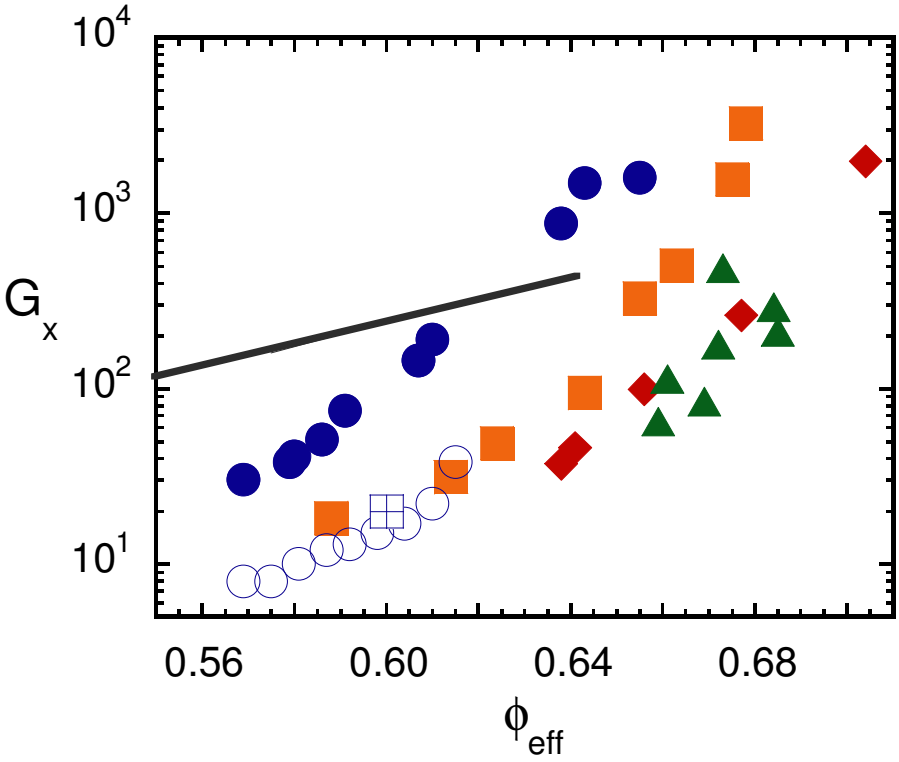

Figure 5.9. Modulus, G_x, at the point where G'^* and G''^* intersect for each shape. S (blue), hDC (orange), sDC (red), and TC (green). Also shown are NLE MNCT calculations from ref [4] as a solid curve, data from ref [5] as open circles, data from ref [13] as an open square.

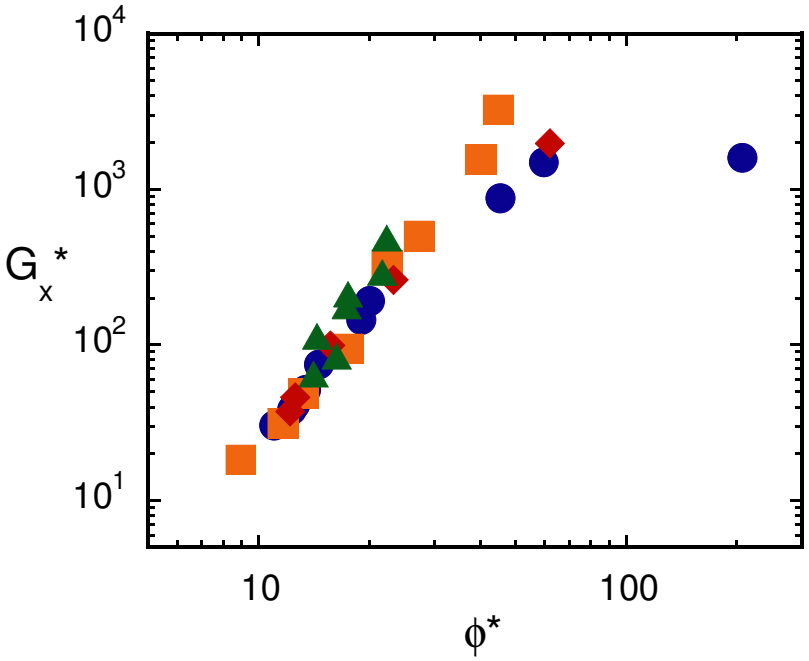

Figure 5.10. G_x* as a function of ϕ* for each particle shape. Data collapse is found when values of ϕ_{RCP} from ref [23] are used to calculate ϕ*.

5.6 List of References

[1] Dawson, K.A., *Cur. Opin. Coll. Inter. Sci.*, **2002**, 7(3-4), 218.
[2] Sciortino, F. and P. Tartaglia, *Adv. Phys.*, **2005**, 54(6), 471.
[3] Russel, W.B., D.A. Saville, and W.R. Schowalter, *Colloidal Dispersions*. 1989, Cambridge, UK: Cambridge Universtiy Press.
[4] Kobelev, V. and K.S. Schweizer, *Phys. Rev. E*, **2005**, 71, 021401.
[5] Anderson, B.J. and C.F. Zukoski, *J. Phys.: Cond. Matt.*, **2009**, 21, 285102.
[6] Buscall, R., P.D.A. Mills, J.W. Goodwin, and D.W. Lawson, *J. Chem. Soc. Faraday Trans. 1*, **1988**, 84(12), 4249..
[7] Kramb, R.C. and C.F. Zukoski, *Langmuir*, **2008**, 24(14), 7565.
[8] Lewis, J.A., *J. Amer. Ceram. Soc*, **2000**, 83, 2341.
[9] Partridge, S.J., *Rheology of Cohesive Sediments*, in *Dept. of Physical Chemistry*. 1985, Bristol University.
[10] Ramakrishnan, S. and C.F. Zukoski, *Langmuir*, **2006**, 22, 7833.
[11] Ramakrishnan, S., V. Gopalakrishnan, and C.F. Zukoski, *Langmuir*, **2005**, 21, 9917.
[12] Ramakrishnan, S., *Depletion Attractions Between Hard Spheres: Comparisons of Theory and Experiment*, in *Chemical Engineering*. **2001**, University of Illinois at Urbana-Champaign: Urbana, IL.
[13] Pham, K.N., G. Petekidis, D. Vlassopoulos, S.U. Egelhaaf, P.N. Pusey, and W.C.K. Poon, *Europhys. Lett.*, **2006**, 75(4), 624.
[14] Rao, R.B., V.L. Kobelev, Q. Li, J.A. Lewis, and K.S. Schweizer, *Langmuir*, **2006**, 22(6), 2441.
[15] Petekidis, G., D. Vlassopoulosa, and P.N. Pusey, *Faraday Discuss*, **2003**, 123, 287.
[16] Chong, S.-H. and W. Götze, *Phys. Rev. E*, **2002**, 65(4), 041503.
[17] Chong, S.-H. and W. Götze, *Phys. Rev. E*, **2002**, 65(5), 051201.
[18] Letz, M., R. Schilling, and A. Latz, *Phys. Rev. E*, **2000**, 62(4), 5173.
[19] Pfleiderer, P., K. Milinkovic, and T. Schilling, *Europhys. Lett.*, **2008**(1), 16003.
[20] Schilling, R., *Phys. Rev. E*, **2002**, 65(5), 051206.
[21] Chong, S.-H. and W. Kob, *Phys. Rev. Lett.*, **2009**, 102(2), 025702.
[22] Zhang, R. and K.S. Schweizer, *Phys. Rev. E*, **2009**, 80, 011502.
[23] Kramb, R.C., R. Zhang, K.S. Schweizer, and C.F. Zukoski, *Phys. Rev. Lett.*, (Accepted June, 2010).
[24] Koumakis, N., A.B. Schofield, and G. Petekidis, *Soft Matt.*, **2008**, 4, 2008.
[25] Mock, E.B., H. De Bruyn, B. Hawkett, R. Gilbert, and C. Zukoski, *Langmuir*, **2006**, 22.
[26] Pham, K.N., G. Petekidis, D. Vlassopoulos, S.U. Egelhaaf, W.C.K. Poon, and P.N. Pusey, *J. of Rheol.*, **2008**, 52(2), 649.
[27] Maranzano, B.J. and N.J. Wagner, *J. Chem. Phys.*, **2001**, 114(23), 10514.

Chapter 6 Yielding in Dense Suspensions: Cage, Bond, and Rotational Confinements

6.1 Introduction

Yielding of soft matter is a subject of intense interest due to the ubiquity of this state in products such as foams, slurries, pastes, inks, adhesives, emulsions, and granular assemblies.[1] Progress in understanding the mechanical behavior of these states comes from studies of the simplest colloid system: hard spheres. The glassy state for hard spheres is created by particles becoming trapped or localized by their neighbors at elevated volume fraction such that cooperative motion is required for long range diffusion. With this as a starting point, the role of attractions in producing a gel is understood as localization due to bond formation. External stresses can induce particles in colloidal glasses and gels to explore the confining potential and if the stresses are large enough, the suspensions flow. Here stress sweep techniques are used to explore the constraints placed on spherical and dumbbell shaped particles in glassy and gelled states.

At the volume fraction marking the onset of localization (characterized by a finite localization length, r_{loc}, which defines the distance of particle diffusion before encountering constraints) hard particles experience a dynamic potential the depth of which grows as volume fraction is raised.[2, 3] Diffusion results from hopping events where particles surmount an entropic barrier created by this dynamical potential.[4] This barrier grows quickly with volume fraction resulting in rapid decreases in particle diffusivity. The elastic modulus of the suspension above the localization volume fraction is associated with the curvature of the dynamic potential at its minimum. This curvature also increases rapidly with volume fraction.[2, 5, 6] Within the conceptual framework of a dynamical potential, the onset of steady flow in colloidal glasses is understood as the

external stress lowering the entropic barrier sufficiently to increase the hoping time associated with particles exchanging nearest neighbors. Stresses and strains that characterize the onset of liquid-like flow are known as the yield stress, τ_y, and yield strain, γ_y. Oscillatory stress measurements and creep measurements can be used to probe the constraints felt by the particles as applied stresses approach τ_y.[7-12]

This situation is further complicated when the particles experience attractions. At low volume fraction as the strength of attraction is increased, suspensions gel. Again gelation is associated with particle localization by neighbors – this time through a dynamic potential dominated by bond formation and the resulting dramatic reduction in the rate of long range diffusion. Yielding is again observed with a similar construct where the applied stress lowers the dynamical potential allowing stress relaxation by long range diffusion. Anisotropy in particle shape opens up new mechanisms for stress relaxation and thus alters the nature of the glassy and gelled states.[13]

Here the focus is on the behavior of suspensions of spherical and anisotropic particles near the yield point. The interest is in exploring the effects of increasing the strength of attraction between the particles on the properties of the suspensions as they yield and in using these mechanical properties to probe the constraints acting on the particles when they are localized. The tool used for this purpose is to expose the suspensions to an oscillatory stress and to increase the magnitude of the stress at fixed frequency. The in-phase and out of phase components of the strain is measured and elastic and viscous moduli are extracted. By investigating how these measures of the suspension's mechanical properties change with volume fraction, strength of attraction and particle shape, the onset of yielding is characterized.

In the discussion, the stress where $G'=G''=G_x$ is used as a measure of the stress sufficient to lower the suspension stress relaxation time to that of the imposed time scale for deformation. Previous work has explored the differences in yielding behavior, using the G_x definition, for suspensions of hard anisotropic particles by scaling volume fraction on a random closed packed or maximum volume fraction, ϕ_{RCP} with much success.[14] While the concept of random close packing for attractive systems is ill-defined, the data discussed below suggests the idea of a hypothetical maximum packing fraction, ϕ_{max} may prove useful for collapsing data for different strengths of attraction.

The constraints acting on the particles in a glassy or gelled system can be probed by observing the stress dependence of the storage and loss moduli around those characterizing G_x. For glassy suspensions, as the stress is increased, there is a single yield event associated with a monotonic decrease in G' and a maximum in G''. This behavior is attributed to hard spheres experiencing a single constraint associated with local topological cages. The cages are disrupted by application of the stress allowing particles to diffuse on a time scale of the deformation. G_x typically occurs at the maximum in G''. At sufficiently high volume fraction, as the strength of attraction is increased, G' develops a shoulder and G'' develops a second maximum.[10] This is interpreted as arising from particles experiencing both bonds produced by the short range attraction and cages produced by topological constraints. Recently there has been a prediction that if the volume fraction of suspensions containing two such constraints is lowered, the cage constraint will be lost and the attractive gels will display a single yielding event associated with the short range attraction alone.[9, 11, 12, 15]

Here experiments on aqueous suspensions containing uniform spherical and dumbbell shaped particles are described where interactions are tuned from repulsive (effectively hard) through weakly attractive to strongly attractive by varying the solvent ionic strength. With proper control of particle interactions, distinct states and yielding behaviors are observable. Because the experiments described here were performed using dumbbell shaped dicolloid particles it is possible to explore the effects of rotational motion in relaxing stress. As far as the author can ascertain, this is the first work to explore a system where three constraints (center of mass, rotational and bonds) might be expected to impact yielding behavior in attractive particle systems.

In section 6.2 of this chapter, particle synthesis and preparation techniques are described as well as experimental procedures and equipment. In section 6.3.1, results are shown from dynamic stress sweep experiments and absolute yield stress is discussed, yield strain, and yield modulus using the *G'=G"* definition of yielding. Also in this section, methods to collapse the data based on the distance from a hypothetical maximum packing fraction[16, 17] are examined. In section 6.3.2 evidence for multiple yielding is compared to previous experiments and simulations.[9, 10, 18] Finally in section 6.4, the findings are summarized and conclusions are offered about the influence of attractions on the yielding of dense suspensions.

6.2 Experimental

The particles used in the experiments discussed here are synthesized in two monodispersed shapes: spheres and symmetric homodicolloid. Particles are synthesized in the size range of D=250-350nm using a multi-step emulsion polymerization technique

developed by Mock and coworkers[19] and described in more detail in ref [16]. Figure 6.1(a,b) shows SEM images of the both particle shapes. The aspect ratio of the dicolloid particles is ~1.3 which is defined as the long axis length, L over the sphere diameter, D.

The particles are stabilized with surface monolayer of a nonionic surfactant [$C_{12}E_6$] and are suspended in a solution of NaCl in water. Salt concentrations are varied to tune particle interactions by screening electrostatic surface charges. Ionic strengths of the suspensions are 0.03, 0.05, 0.1, 0.3, 0.5 and 1.0M. The particle surface charge is measured with electrophoresis and is the same (within experimental uncertainty) for each shape at a given ionic strength. The combination of electrostatic charge and van der Waals forces give the full particle interaction energies as described in ref [16]. It has been shown that at 0.03, 0.05M and 0.1M ionic strength, the particles behave as if they are experiencing effectively hard interactions once particles sizes and volume fractions are corrected for the double layer repulsion. These electrostatic repulsions yield an effectively hard potential with cores of a diameter set by the position where the pair potential drops to $1k_BT$. This adds approximately two double layer distances to the particle diameter. The effective volume fraction is defined as, $\phi_{eff}=\phi[(D+\Delta)/D]^3$ (or $\phi[(\{L+\Delta\}^2\{D+\Delta\})/(L^2D)]$ for dicolloids) where Δ=increased particle diameter due to the presences of the surfactant molecule and the double layer. The surfactant has a length of ~4nm resulting at full coverage in an increase in particle diameter of ~8nm.[20] To this is added a distance associated with decay of the electrostatic potential yielding Δ = 14.00, 11.55, and 9.85 for ionic strengths of 0.01, 0.05, and 0.1M respectively. For higher ionic strengths, the interaction between particles becomes increasingly attractive. Based on a Hamaker coefficient of $3.1k_BT$ for polystyrene particles suspended in water, for these

samples, $\phi \approx \phi_{eff}$ and the strength of attraction at the minimum in the potential is ~1.6, 1.9 and $2.3 k_B T$ for 0.3, 0.5 and 1.0M suspension ionic strengths respectively. A detailed explanation of the pair interaction potential and figure showing the full calculation can be found in the Appendix, Equation A.1 and A.2 and Figure A.1.

SEM micrographs of the particles were taken using a Hitachi S4700 instrument. One drop of the as-synthesized suspension was placed on a Formvar coated copper grid and attached to a sample holder using conductive tape. Particle dimensions were determined by measuring 50-100 particles from SEM images and confirmed with dynamic light scattering with a bench-top FOQELS DLS instrument.

After synthesis, particles are cleaned and concentrated to ϕ~0.35 with dialysis against deionized water. $C_{12}E_6$ and a concentrated solution of aqueous NaCl (0.1M, 0.5M, 1.0M or 5.0M) is then added to the particle suspension such that the final surfactant concentration is 0.03M (sufficient for monolayer coverage[21]) and the final solvent ionic strength is the desired value. The suspensions are then concentrated further with centrifugation (~4000g) until no supernatant can be removed. The highly concentrated suspension remaining in the centrifuge tube becomes the highest volume fraction sample for a given particle shape and is subsequently diluted to obtain lower volume fractions at that condition

To perform rheological experiments, ~3.2mL of sample is removed from the centrifuge tube and transferred to the cup of a cup-and-bob geometry Bohlin constant stress C-VOR rheometer equipped with a roughed titanium bob. A small portion of the sample in the cup is then removed and the wet and dry weight is measured, and with material densities, is used to obtain the sample volume fraction. The samples undergo an

oscillatory stress sweep from ~0.01-1000Pa at a frequency of 1Hz, where the viscous and elastic moduli are measured. Each data point has an integration time of 4s.

Stress and moduli are nondimensionalized with k_BT and a measure of the particle volume, V^* such that stress $\tau^*=\tau V^*/k_BT$ and $G^*=GV^*/k_BT$. For spheres, $V^*=D_{eff}^3$, while for dicolloids, $V^*=L_{eff}^2 D_{eff}$.[22]

6.3. Results and Discussion

6.3.1 Yield stress, yield strain and ϕ_{max}

Moduli derived in dynamic stress sweep experiments for suspensions of spheres and dicolloids are shown in Figures 6.2 and 6.3 (a-f). Here the full stress sweep for one volume fraction is shown for each ionic strength and the plateau values of $G_0'^*$ and $G_0''^*$ for all volume fractions in the insets. For each ionic strength, the volume fractions are chosen so that the effective volume fraction, when the extent of the double layer is taken into account, remains approximately constant (0.59-0.60 for spheres, 0.65-0.66 for dicolloids) through the first attractive ionic strength 0.3M. For the 0.5M and 1.0M samples, the volume fraction was chosen such that $G_0'^*$ is approximately the same as the 0.3M sample. (Volume fractions used for Fig 6.2 and 6.3 are indicated as lighter colored points in Figure 6.6 discussed later) These samples display behavior characteristic of the states seen at other volume fractions. All samples studied here are at volume fractions above the kinetic glass transition where $G_0' > G_0''$ at a frequency of 1Hz.

A common method to probe yielding in these suspensions is to define the absolute yield point as the intersection of G'^* and G''^* (i.e., the stress (strain) where $G'^*=G''^*=G_x^*$).[7] In all suspensions studied here, this provides a single yield stress τ_y,

and yield strain γ_y. Despite multiple maxima in both *G'* and *G"*, there is only one crossover point for every sample. This yield point is associated as occurring when deformation reduces the stress relaxation time to close to that of the applied deformation of 2πs.

For repulsive sphere suspensions, the location of G_x is nearly the same as the maximum in *G"*. For the weakly attractive suspensions at 0.3M, G_x is found between the two peaks in *G"*. As attractions are increased into the gel state, G_x is seen at stresses just higher than the sharp drop in both *G'* and *G"*. In Figure 6.4a, yield stress as a function of sphere volume fraction (or effective volume fraction) is shown for ionic strengths of 0.03, 0.05, 0.1, 0.3, 0.5 and 1.0M. (Again, for ionic strengths larger than 0.1M, $\phi_{eff}=\phi$). For low ionic strengths, the use of ϕ_{eff} successfully collapses the data onto nearly a single curve. The yield stress is well modeled with an exponential equation $\tau_y^*=Ae^{b\phi}$, where $A\sim10^{-14}$ and $b\sim55$ for these conditions. At 0.3M, with $\phi\sim0.60$ the yield stress is higher by approximately an order of magnitude, which is attributed to the presence of interparticle attractions. The steepness of the volume fraction dependence is also higher at this ionic strength with the exponential fit yielding $A\sim10^{-25}$ and $b\sim100$. At 0.5M yield stress curves remain exponential and move to lower volume fractions with exponential parameters similar to 0.3M, $A\sim10^{-20}$ and $b\sim95$. With only three points for 1.0M, accurate fitting of the data could not be obtained, but the results at this condition are qualitatively similar to the other attractive conditions with a shift to lower volume fractions.

To gain insight into the behavior of these suspensions at extremely high volume fractions, the measured volume fraction can be modified in such a way as to quantify the distance from a hypothetical maximum packing fraction as described earlier, where

$\phi^*=1/(\phi_{max}-\phi)$.[17] For hard spherical particles, a maximum disordered volume fraction of 0.64-0.66 can be sustained. Higher volume fractions require ordering.[17, 23-25] At this maximum volume fraction (random close packing volume fraction), for hard spheres the contact value of the pair distribution function and the osmotic compressibility of the suspension diverge resulting in the localization length for constrained particles going to zero. As a result, mechanical properties such as modulus and yield stress are predicted to diverge.[26] The concept of a maximum packing fraction, however, is not well defined for attractive systems as mechanical properties appear to diverge far below ϕ=0.64. A value for ϕ_{max} can still be formally defined for attractive systems by fitting the data to the repulsive condition data where ϕ_{max} has been well documented. In the inset of Figure 6.4a, the yield stress as a function of this reduced volume fraction is plotted. For effectively hard conditions, ϕ_{max}=0.66 is used, based on the success of previous work with these particles.[16] For attractive conditions, ϕ_{max} is treated as a fitting parameter and it is found that for 0.3M ϕ_{max}=0.63, 0.5M ϕ_{max}=0.59, and 1.0M ϕ_{max}=0.47. While these values provide a good fit with the repulsive particles far away from ϕ_{max}, the behavior of the attractive and repulsive particles deviate close to ϕ_{max}. Repulsive condition data show a plateau of the dimensionless yield stress at about 100. This plateau is attributed to the softness of the double layer which begins to deform rather than flow. For attractive conditions however, there is no plateau and the yield stress continues to rise above 100. The data for 0.3 and 0.5M superimpose using the reduced volume fraction parameter and the fitted values for ϕ_{max}.

The hypothesis established by this correlation is that attractions decrease a hypothetical maximum packing fraction. Accounting for this change in ϕ_{max} results in

apparent universal collapse for multiple strengths of attraction. For these attractive systems, the yield stress is well modeled with a power law dependence on ϕ^* of the form $\tau_y^* \sim \phi^{*x}$ where $x \sim 4$. Soft repulsive conditions will fit this approximation only under conditions where they are rendered effectively hard - i.e., when the particles are not forced to separations where the softness of the repulsion is probed.

The same analysis is shown for suspensions of dicolloids in Figure 6.4b. The behavior for these suspensions is qualitatively similar to spheres. The use of effective volume fraction reasonably collapses the repulsive conditions. The collapse of the repulsive conditions at the lowest ionic strength is not as exact as with the spherical particles. This could be attributed to the double layer at low ionic strengths distorting the effective dicolloid shape of the particle to more sphere-like. This effect of smearing the anisotropy of the particle shape would decrease with ionic strength resulting in different effective shapes at low and high ionic strengths.

The inset of Figure 6.4b shows rescaling the volume fraction using $1/(\phi_{max}-\phi)$. For repulsive ionic strengths, $\phi_{max}=0.72$[16] is used. For 0.3, 0.5 and 1.0M, best fits yield $\phi_{max}=0.70$, 0.68 and 0.53 respectively. Like the spheres, at the lowest ionic strengths and highest volume fractions, the modulus does not increase with a power law slope of 4. All conditions except for 0.03M can be modeled as a power law similar to attractive spheres with a slightly higher exponent, x~5-6.

Is the strength of attraction dependent maximum packing fraction an anomaly of curve fitting or does the collapse shown here suggest some underlying physics? It is speculated that if there is an underlying physics, it has an origin in jamming volume fractions that depend on strength of attraction. The results shown here are reminiscent to

the behavior of aggregated suspensions in a pressure filter. Compression of a bed of attractive particles in a pressure filter results in a pressure-volume fraction curve that appears to diverge at a particular volume fraction. Again this apparent maximum packing fraction decreases with the increases in strength of attraction.[27-30] In the pressure filter case, however, if the particles in the compressed bed are subjected to shear, the steady state volume fraction of the bed increases. As a result, one can generate pressure–volume fraction curves at different shear rates and the apparent maximum packing fraction increases with shear rate.[27, 28, 31, 32] These observations suggest that under a given shear history, attractions produce force chains that can carry normal loads such as developed in the centrifugal concentration used in this work. These structures support small strains elastically and can be disrupted and reformed. The hypothesis is that at a given volume fraction, the pressure required to collapse the bed and the stresses required to shear the bed both grow with the number of contacts between the particles in a manner that is sensitive to the proximity of a jamming volume fraction. This jamming volume fraction depends on particle shape, strength of attraction, and shear history of the sample during compaction. The data suggest the role of particle properties (shape, and strength of attraction) and shear history are largely contained in ϕ_{max}.

Figure 6.5a and 6.5b shows the yield strain of both sphere and dicolloid suspensions at each ionic strength. 1.0M is excluded from the figure due to the low volume fractions of these samples and so that the other ionic strengths can be better distinguished. For spheres, nonmonotonic dependence of yield strain on volume fraction is seen, with approximately the same behavior for all repulsive conditions when ϕ_{eff} is used. A maximum in the yield strain is seen at an effective volume fraction near 0.60

consistent with previous reports.[7, 12] As ionic strength is increased, the maximum in the yield strain moves to lower volume fractions in a qualitatively similar way as the yield stress and ϕ_{max}. The maximums for 0.3M and 0.5M occur near volume fractions of 0.57 and 0.53.

The yield strain behavior of dicolloid suspensions is difficult to generalize. Maximums in yield strain are not clear at any of the ionic strengths investigated. Additionally, the shift with ionic strength to lower volume fractions is less pronounced than for the spheres. Nearly all data points fall between ϕ=0.59 and 0.67. Some of the differences in behavior between spheres and dicolloids may be attributable to the complex shape of the stress sweep curves with the location of G_x often shifting to different locations around multiple peaks in *G"* and *G'*. Note that within the frame work of nMCT, the yield strain is derived from the ratio of the stress and the modulus. The stress is dependent on the dynamic potential barrier height while the modulus is dependent of the curvature of the dynamic potential at its minimum. As a result, changes in the yield strain will depend on subtle volume fraction dependencies of these parameters, and a strong congruence of yield strain behavior between spheres and dumbbells is not necessarily expected.

6.3.2 Constraints and multiple yielding events

The initiation of flow requires suspension microstructure to rearrange in a manner that relaxation times decrease. The nature of the constraints limiting this rearrangement can be probed by looking at the stress dependence of the moduli curves. Here refer back to Figures 6.2a and 6.2b.

Beginning with spheres at 0.03M the behavior is typical of hard-sphere-like systems. There is a low stress plateau with *G' >G"*. The plateau is followed by a drop in *G'*. As ionic strength is increased to 0.05M and 0.1M, the behavior remains similar. The main difference lies in a reduction of the *G"* peak height with increasing ionic strength. This observation is consistent with previous results that show a disappearance of the *G"* maximum as interparticle attractions were turned on.[10] Increasing attractions are known to first increase fluidity of hard particle glasses before particles are localized by bond formation. Consistent with this knowledge, the decreases in peak height in *G"* in suspensions experiencing weak attractions suggest less energy is dissipated in disrupting microstructures of weakly attractive particles than hard particles.

As ionic strength is further increased to 0.3M, the emergence of a second maximum in *G"* at stress larger than the location of G_x is seen. At the highest ionic strengths 0.5M and 1.0M, no maximum in *G"* is seen, only a plateau followed by a drop in both *G'* and *G"*. The steepness of the fall in moduli increases as ionic strength is raised.

Based on these results, three separate suspension states can be distinguished. At the three lowest ionic strengths, there is a *nonbonded repulsive glass*.[18] This state is characterized by a single maximum in *G"* as stress is increased and this maximum occurs near G_x. This yielding response is interpreted as resulting from the applied stress lowering an entropic barrier to a point where the hopping time associated with particles diffusing out of a dynamical potential well is lowered to a time scale comparable with the deformation time. This barrier is identified with localization of center or mass diffusion due to cage formation of neighboring particles.

For the intermediate ionic strength of 0.3M, two distinct yield stresses are seen associated with a shoulder in *G'* and two separate *G"* maxima. Following earlier work this state is called a doubly confined *bonded repulsive glass.*[18] One yield stress is associated with a barrier due to attractive bonding of particles, while the other is due to cage formation. Intuitively one expects yielding by first displacing out of the short range attractive wells while a second yield event displaces particles from nearest neighbor cages.[9] Interestingly yielding due to bond breakage is thus predicted to occur at a lower stress than that which disrupts cages. Note that the stress a the second maximum is larger than G_x indicating that the suspension is largely in a liquid-like state once the second constraint is probed.

At the highest ionic strength, interparticle attractions increase and strong bonds form. Gelation will occur at volume fractions below those which result in cages of nearest neighbors. This results in a *dense gel* with volume fractions greater than the gel point at ϕ~0.35 but less than ϕ ~0.58 needed for cage confinement. Here only one yielding event is seen when the bonds are broken. (Figure 6.2f).

The yielding behavior and location of maximums in *G"* can also be described in terms of strain and the extent of deformation required to either break bonds or cages.[9, 10] For the repulsive conditions, the single *G"* maximum occurs at strains between 1-10% (γ~0.01-0.1). For double peak conditions, the first roll off in *G"* begins at strains near 1%, while the second maximum is seen at strains between 20-30%. For the dense gel state, *G"* begins to drop at a strain of ~1% for the lowest volume fraction and moves to even lower strains as volume fraction is increased. The results are similar to those reported previously.[9, 10]

For dicolloids particles, the picture is more complex. Unlike spheres that can relieve stress only through translational motion, dicolloid particles can also relieve stress through rotation. For hard anisotropic particles, the existence of multiple modes of motion and stress relief has been described using MCT[13, 33-38] and nMCT.[13] From nMCT, the behavior of anisotropic particle suspensions is determined by simultaneously solving equations for localization of CM motion (r_{loc}) and rotational motion (θ_{loc}). This provides an energy landscape with multiple barriers to particle motion. For weakly anisotropic particles there is a decoupling of rotational diffusion and center of mass diffusion such that it is possible to produce *plastic glasses* where particle centers of mass are localized and *double glasses* where both center of mass and rotational diffusion are localized.[13] Thus in addition to bonded and nonbonded glasses one can also observe either plastic or double glasses for each bond state. As a result, for hard dicolloids one expects to observe *nonbonded repulsive plastic glasses* at low volume fractions and *nonbonded repulsive double glasses* at high volume fractions. These states are distinguished by single and double yielding events (or a transition from one to two maxima in *G"*) as volume fraction is raised. This behavior is illustrated at 0.03M where detailed evaluation of the pair potential indicates the particles experience repulsive interactions[16] with the dicolloid sample shown in Fig 6.3a. The first yield event is attributed to applied stress decreasing the barrier to rotational diffusion to a sufficient extent that rotation can relax stress while the second yield event is associated with lowering the barrier to center of mass diffusion. This interpretation is consistent with the calculations of Zhang and Schweizer which indicate that the entropic barrier to rotational diffusion is lower than that for center of mass diffusion.[13] At an ionic strength of 0.1M,

qualitatively similar behavior is observed. However, the high stress peak in *G"* grows in magnitude and width while the high stress shoulder in *G'* turns into a peak demonstrating dynamic shear thickening.

At 0.3M, the dicolloids experience weak attractions. At the same ionic strength, suspensions of spheres show two yielding events associated with bond and cage yielding. For the dicolloids, a pronounced minimum in both *G'* and *G"* before the high stress maximum is observed. At 0.3M, the *G"* peak has dropped below its low stress plateau value. Also a much sharper initial drop in both *G'* and *G"* is seen compared to the behavior at lower ionic strengths. These differences from the lower ionic strengths where the particles experience repulsive pair potentials suggest yielding occurs in qualitatively different ways when anisotropic the particles experience attractions.

One might expect three yield events under these circumstances resulting from activation of stress relaxation due to rotational diffusion, diffusion out of potential wells arising from bonds and diffusion out of dynamical potential barriers arising from cages. However, two of the three must be strongly correlated so that exceeding the barrier of each one is not able to be distinguished. It is suggested that rotations and CM motion become coupled once bonds are formed. At 0.5M where spheres formed a dense gel state, in the dicolloid suspensions a high stress *G"* peak is observed accompanied by a *G'* shoulder as opposed to a *G'* peak. This result is taken to indicate that two confinements still exist for this sample.

Finally at the highest ionic strength of 1.0M, no *G"* maximums and a sharp drop in both *G'* and *G"* are seen with increasing stress. This is nearly identical to suspensions of spheres in the dense gel state at this ionic strength. The volume fraction is sufficiently

low that particle shape appears not to influence the suspension's rheological behavior again suggesting that in attractive systems that gel, rotational and translational diffusion are strongly coupled.

Similar dynamic stress sweep experiments were performed at additional volume fractions for each ionic strength. Signatures of single or multiple yielding events such as those discussed above are summarized for results for spheres and dicolloids in Figures 6.6a,b. For spheres yielding associated with exceeding cage barriers for effective volume fractions higher than ~0.57 is seen, as indicated by the horizontal dashed line in Fig 4a. This agrees well with the conventional kinetic hard sphere glass transition volume fraction of 0.58. Double yielding *bonded repulsive glass* states are observed for samples where the volume fraction is greater than 0.57 and the ionic strength is high enough for attractions between particles, roughly indicated by the horizontal dashed line in Figure 6.4a. For higher ionic strengths that result in stronger attractions, the samples gel before reaching ϕ=0.57 and thus form *dense gels*.

For dicolloids four states are seen. At low ionic strengths and effective volume fractions between ~0.60 and 0.63 single yielding *nonbonded repulsive plastic glasses* are seen. For $\phi_{eff} > 0.63$, rotational confinements and double yielding nonlinear rheology is observed. These conditions correspond to *nonbonded repulsive double glass* states predicted by nMCT for weakly anisotropic hard particle suspensions. As attractions are turned on and bonds are formed, the ability to distinguish rotational and CM yielding is lost. Two yielding events are seen that are qualitatively different than the two events for nonbonded glasses. Therefore, this state is the dicolloid version of a *bonded repulsive glass*. Finally, at the highest ionic strength, the volume fraction that was probed

experimentally is limited from strong attractions such that caging is not possible and only bond yielding is observed. This is the only dicolloid state where only one yielding event occurs and is named the *dense gel* state.

Additional plots of the dynamic stress sweep experiments for all conditions can be found in the Appendix Figure A.2(a-f) for spheres and Figure A.3(a-f) for dicolloids. These plots show the change in behavior as volume fraction is varied for each ionic strength, as well as showing examples of the yielding behavior of each state defined above.

6.4 Conclusion

Here the effects of varying particle interactions and particle shape on the yielding of dense suspensions have been explored. Yielding of these suspensions was characterized by investigating the strength of attraction and particle shape effects on the stress and strain where *G'=G"*. For all systems, the yield stress defined in this manner is found to have an exponential dependence on (effective) volume fraction. For spheres, the yield stress shows a plateau under repulsive conditions close to ϕ_{max} likely due to the soft nature of the double layer. Attractive systems continue increasing and are well modeled by $\tau_y^* \sim \phi^{*4}$. For dicolloids, only at the lowest ionic strength of 0.03M were signs of a plateau yield stress evident while all other ionic strengths approximately follow the form $\tau_y^* \sim \phi^{*5\text{-}6}$. The strength of attraction dependent maximum packing fractions are empirical but are suggestive of jamming volume fractions that depend on particle shape, interaction potential and shear history.

Evidence for multiple yielding events are seen for weakly attractive interactions and understand these results in terms bond formation and caging. With dicolloid particles, a third type of confinement, that which localizes rotational motion, is evident. Using the results from stress sweep experiments a state diagram is constructed where three nonergodic states are seen for spheres and possibly four for dicolloids. For spheres the same states described by Zaccerelli and Poon[18] are seen: *nonbonded repulsive glass*, *bonded repulsive glass*, and *dense gel*. For dicolloids, nonbonded glasses have the additional possibility of being either a *plastic glass* with no observable rotational confinement and yielding or a *double glass* where CM and rotational barriers must be overcome to yield.[13] The experiments do not provide evidence for transition from a double bonded repulsive glass to a plastic bonded repulsive glass suggesting a strong coupling of rotational and center of mass diffusion in attractive anisotropic particle suspensions. As a result for the dumbbells studied here, the state diagram indicates the existence of *nonbonded plastic repulsive glasses*, *nonbonded double repulsive glasses*, *bonded repulsive glasses* and *dense gels*.

6.5 Figures

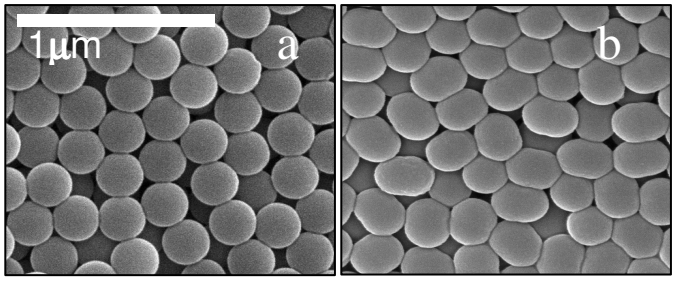

Figure 6.1. SEM images particles used in experiments: Spheres (a), Dicolloids (b),

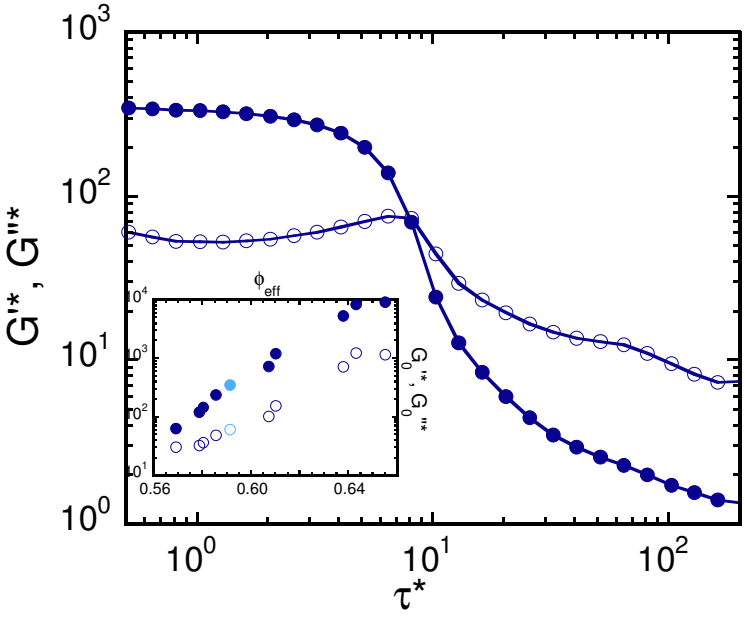

(a)

Figure 6.2 (continued on next page)

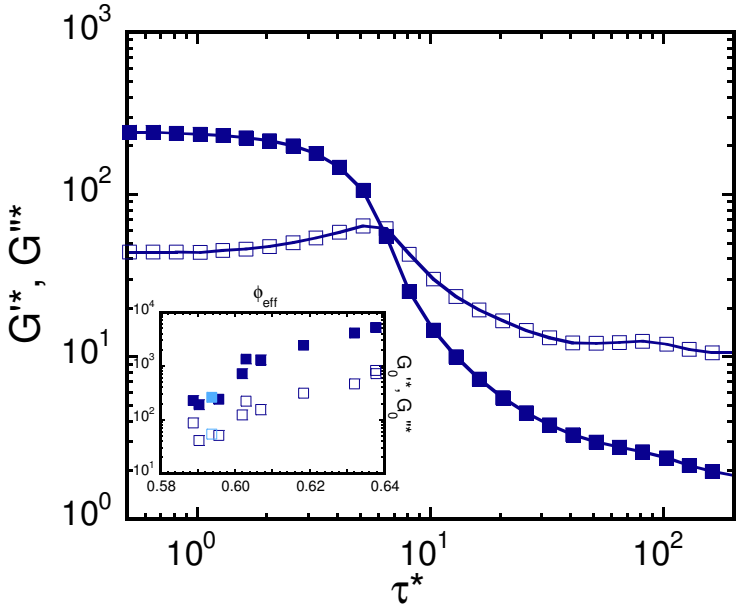

(b)

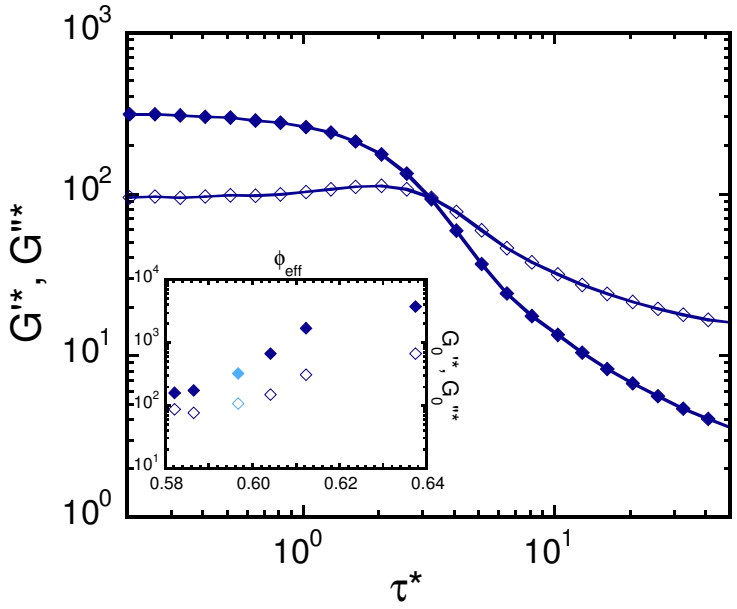

(c)

Figure 6.2 (continued on next page)

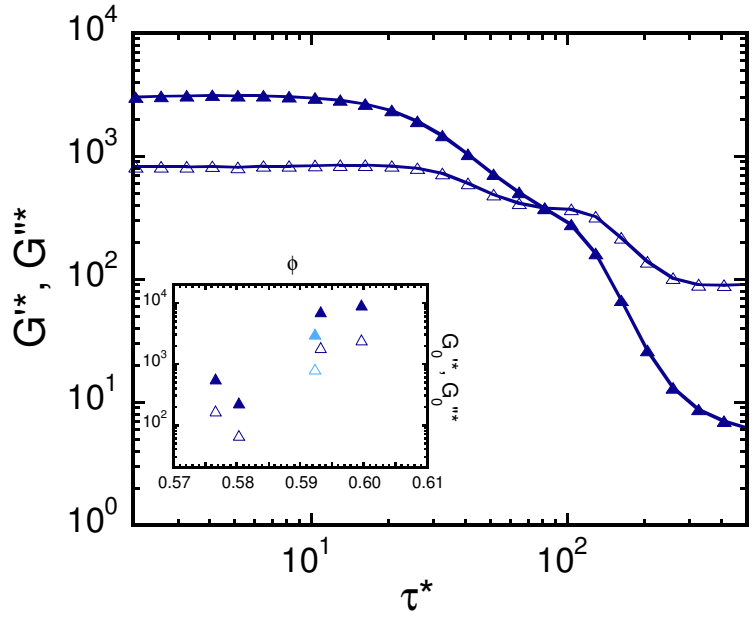

(d)

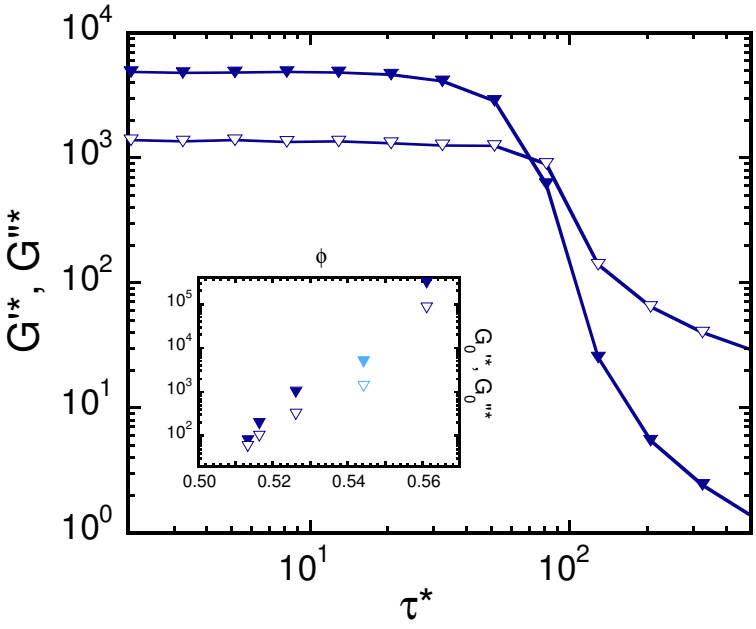

(e)

Figure 6.2 (continued on next page)

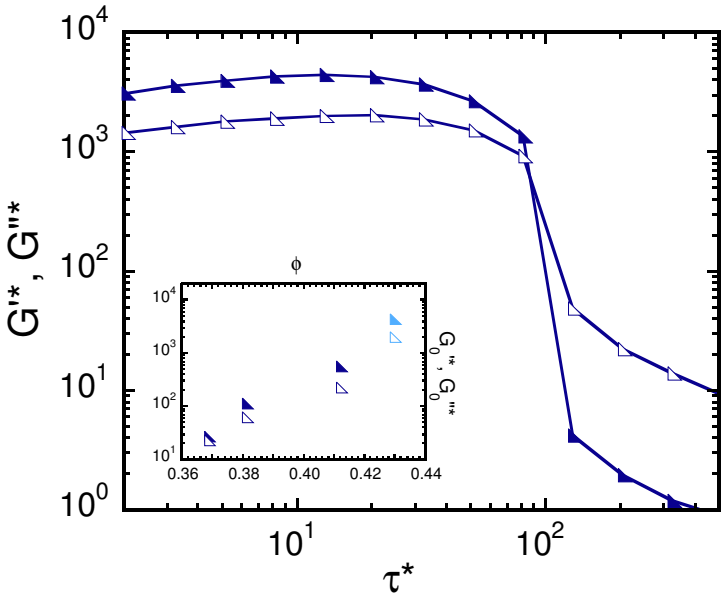

(f)

Figure 6.2. Dynamic strain sweeps showing *G'** and *G"** for Spheres at 0.03M (a), 0.05M (b), 0.1M (c), 0.3M (d) 0.5M (e) and 1.0M (f). (inset) G_0'*, G_0"* for each ionic strength as a function of volume fraction. Solid points are G_0'* and open points are G_0"*. (Effective) volume fractions for main panels are: 0.591 (a), 0.594 (b), 0.597 (c), 0.592 (d), 0.545 (e), 0.430 (f) and are shown in the inset with lighter colored points.

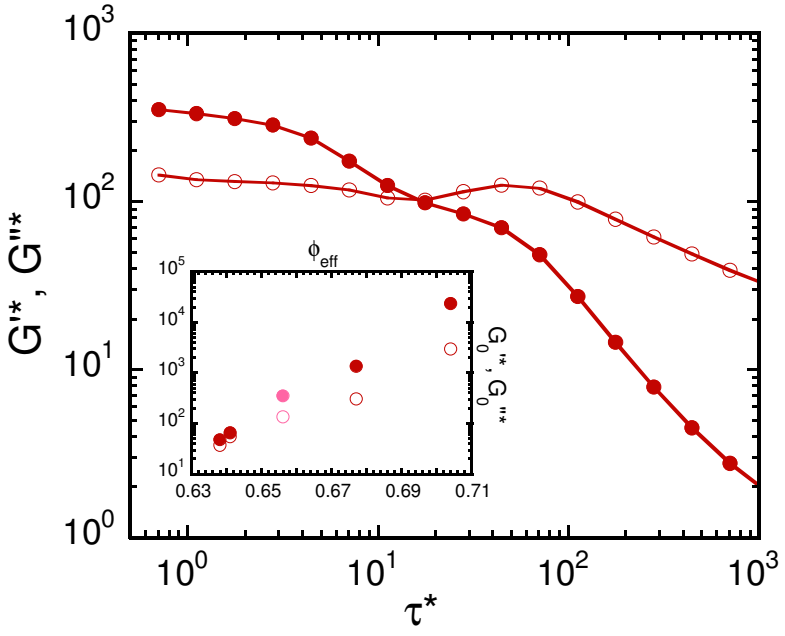

(a)

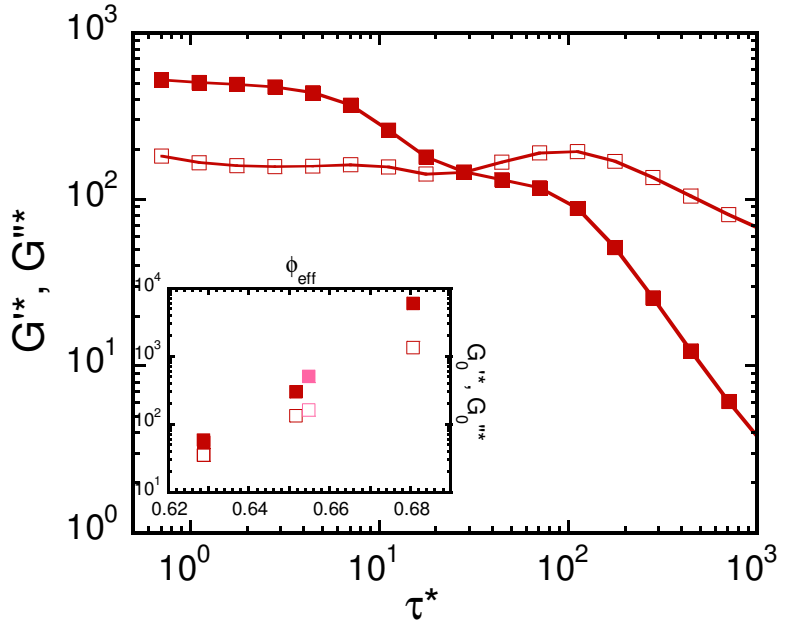

(b)

Figure 6.3 (continued on next page)

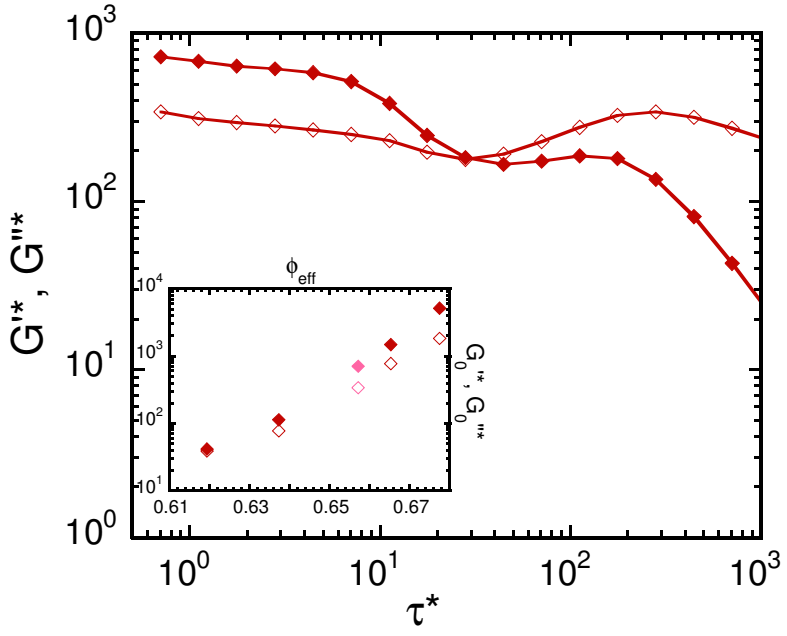

(c)

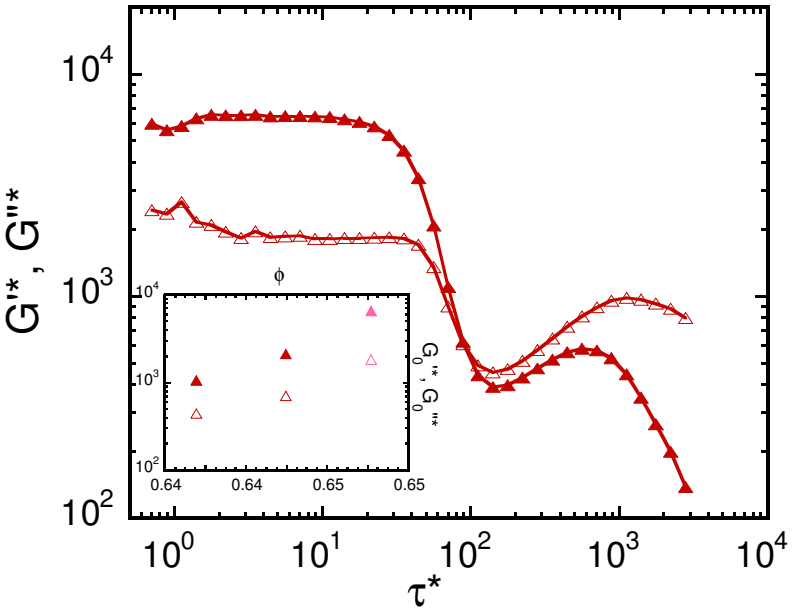

(d)

Figure 6.3 (continued on next page)

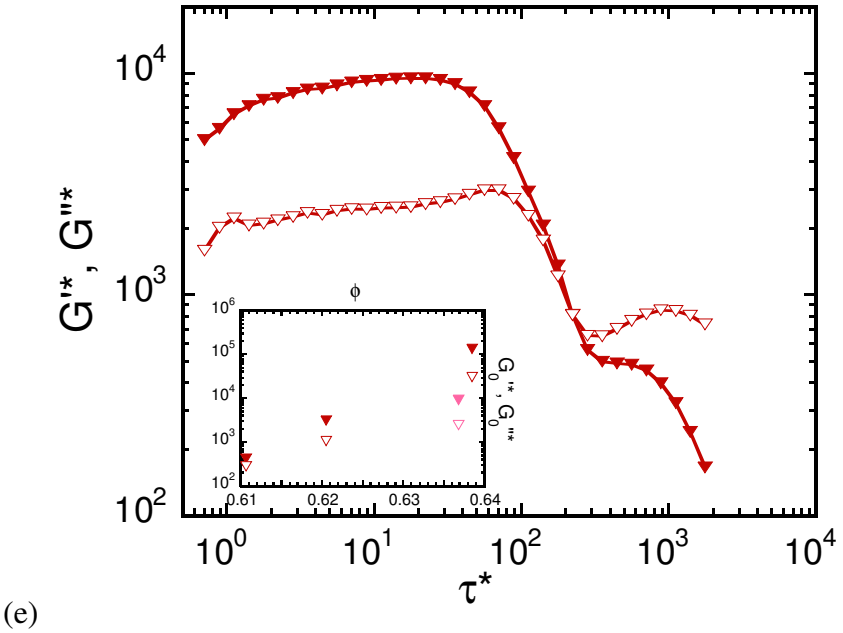

(e)

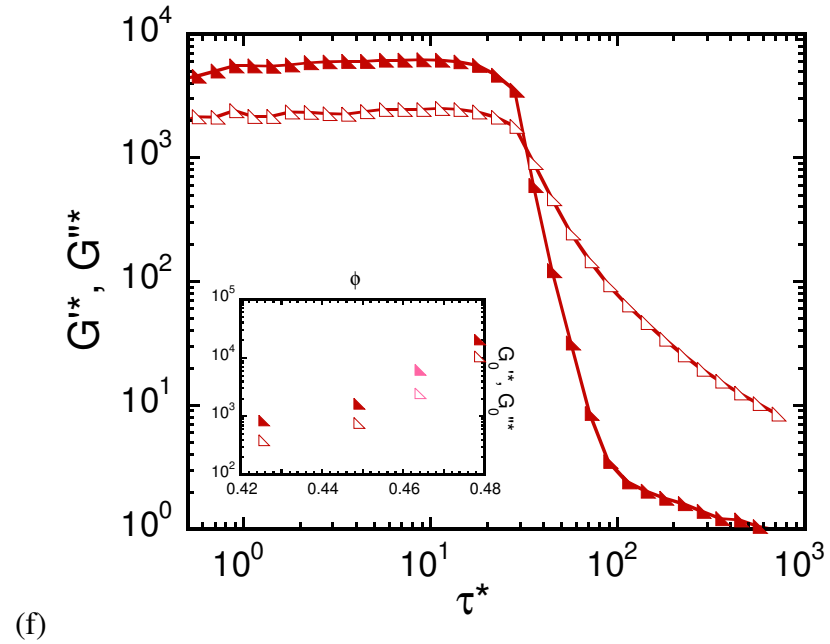

(f)

Figure 6.3. Dynamic strain sweeps showing *G'** and *G"** for Dicolloids at 0.03M (a), 0.05M (b), 0.1M (c), 0.3M (d) 0.5M (e) and 1.0M (f). (inset) G_0'*, G_0"* for each ionic strength as a function of volume fraction. Solid points are G_0'* and open points are G_0"*. (Effective) volume fractions for the main panels are: 0.656 (a), 0.654 (b), 0.656 (c), 0.647 (d), 0.636 (e), 0.464 (f) and are shown in the inset with lighter colored points.

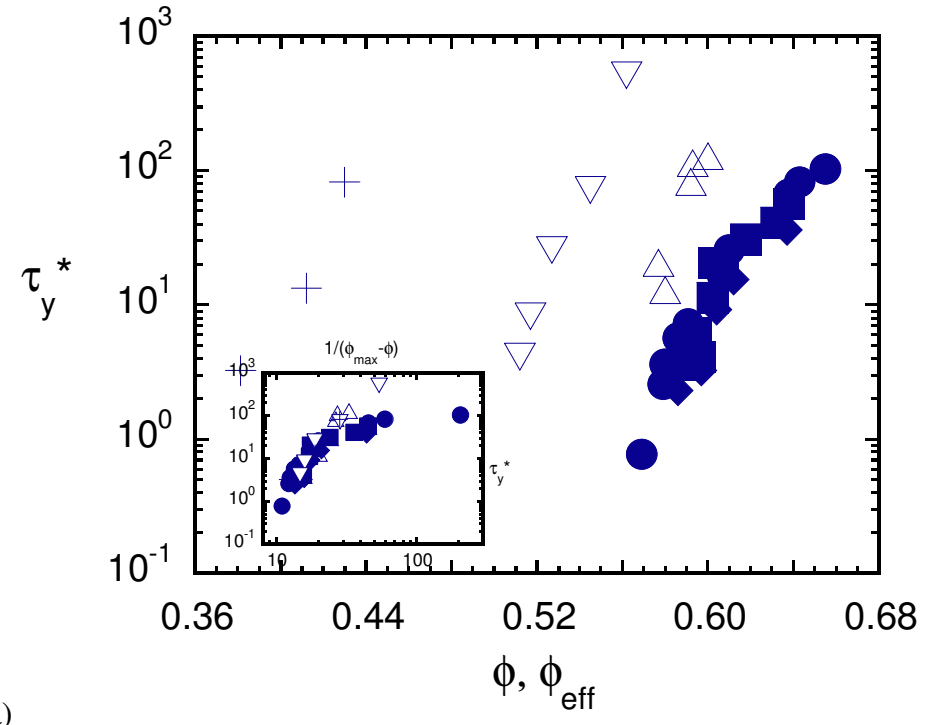

(a)

Figure 6.4 (continued on next page)

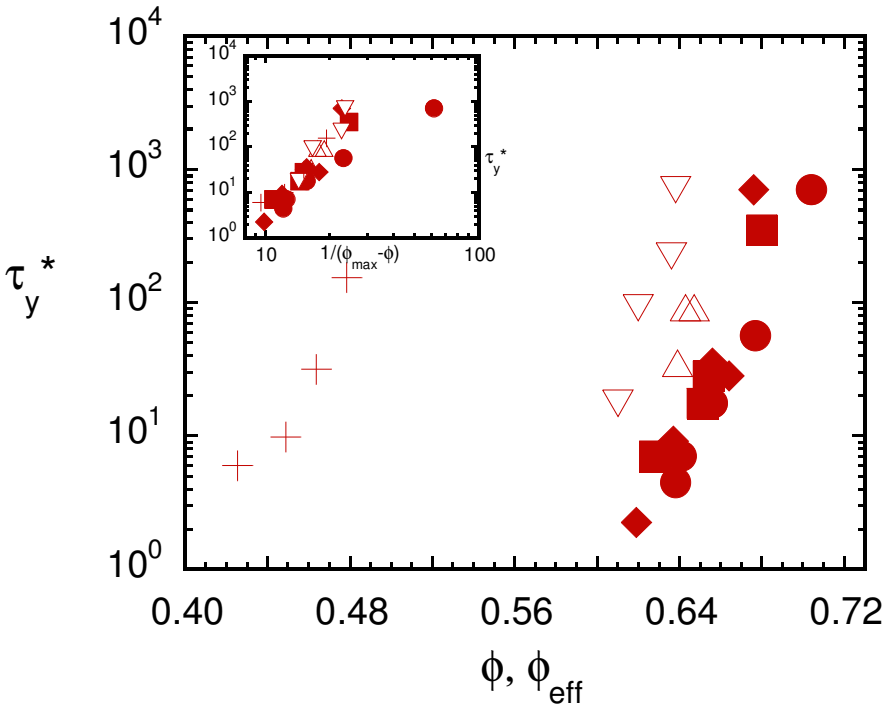

(b)

Figure 6.4. Dimensionless absolute yield stress (τ_y*) as a function of (effective) volume fraction all ionic strengths (Spheres panel a, Dicolloids panel b): 0.03M (filled circles), 0.05M (filled squares), 0.1M (filled diamonds), 0.3M (open up triangles), 0.5M (open down triangles), and 1.0M (plus). Low ionic strengths show similar behavior when volume fraction scaling ϕ_{eff} is used. (Inset) Yield stress as a function of ϕ*.

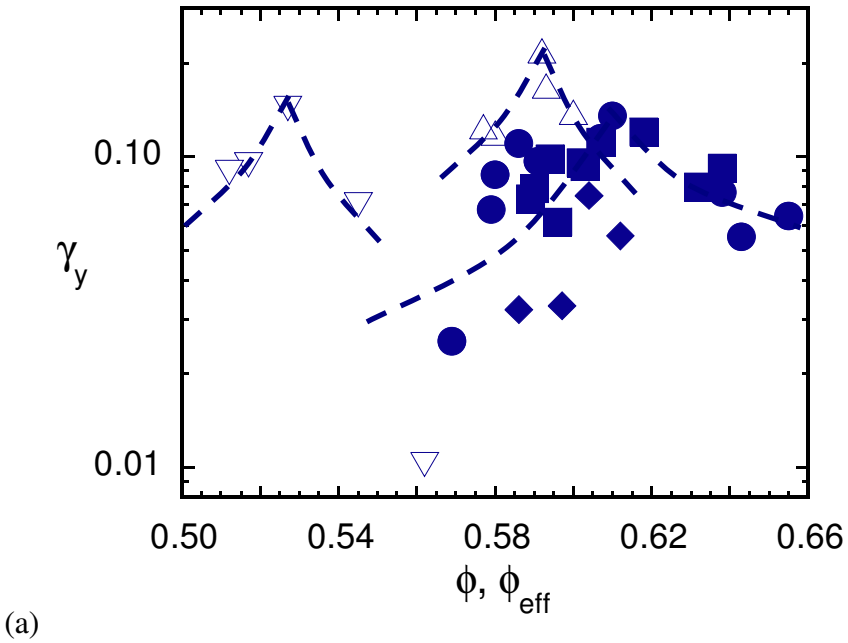

(a)

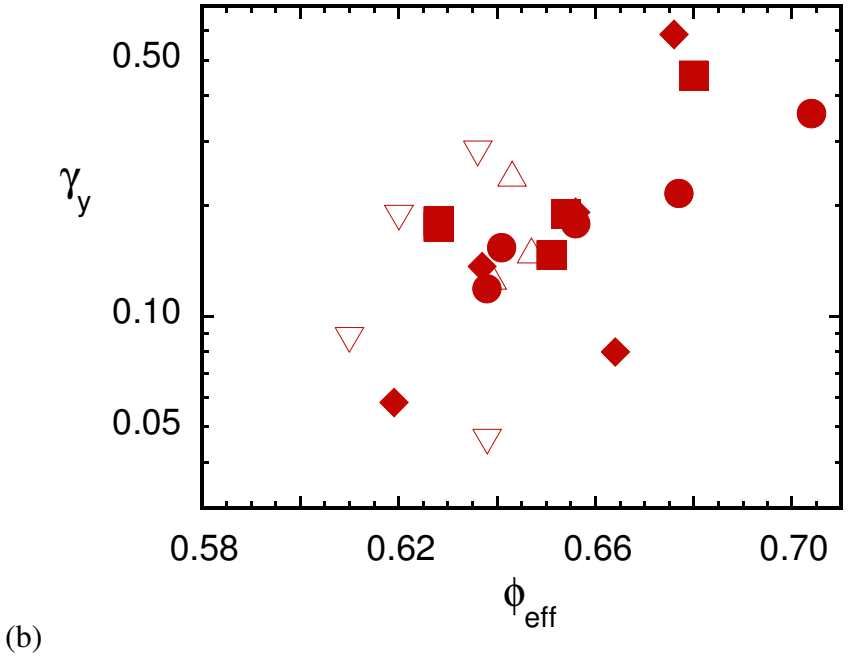

(b)

Figure 6.5. Absolute yield strain (γ_y) as a function of (effective) volume fraction all ionic strengths (Spheres panel a, Dicolloids panel b): 0.03M (filled circles), 0.05M (filled squares), 0.1M (filled diamonds), 0.3M (open up triangles), 0.5M (open down triangles). Dashed curves are to guide the eye to the maximum yield strains for sphere particle suspensions.

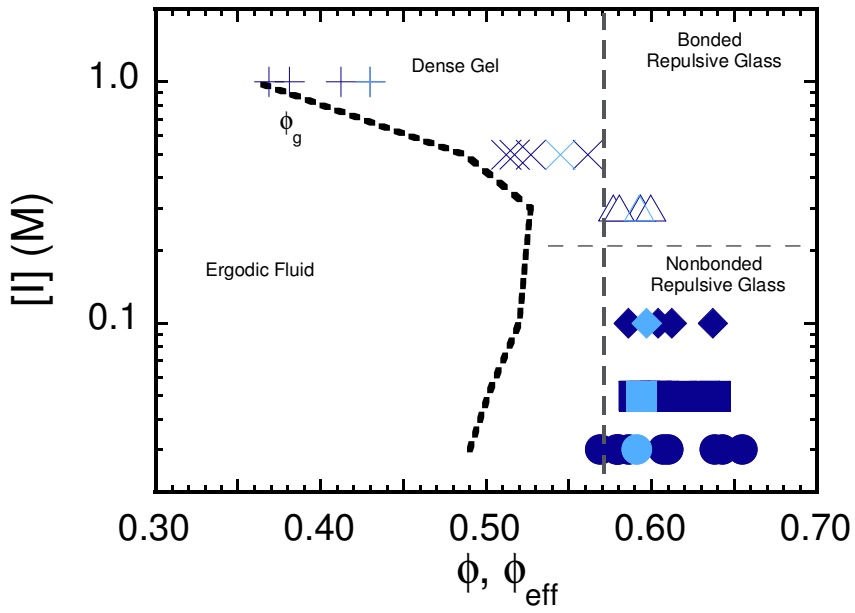

(a)

Figure 6.6 (continued on next page)

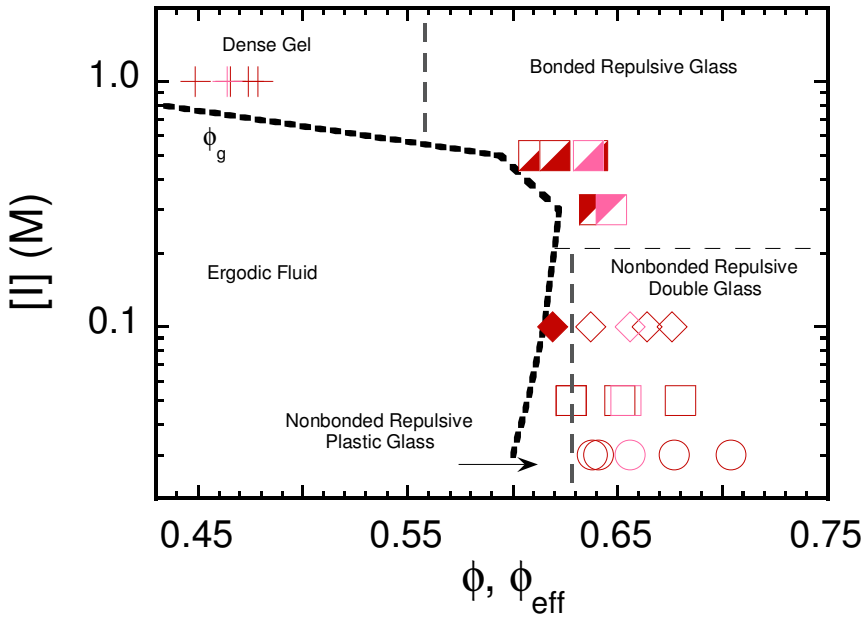

(b)

Figure 6.6. "Multiple yielding" state diagram. For spheres (blue, panel a), single cage yielding samples are closed points, single bond yielding samples are star points, and double yielding are open points. For dicolloids (red, panel b), single yielding nonbonded repulsive plastic glass samples are solid points, nonbonded repulsive double glasses are open points, bonded repulsive glasses are half-filled points, and dense gels are plus signs. Volume fractions used for Fig 2, 3 are indicated with lighter colored points here.

6.6 List of References

[1] Russel, W.B., D.A. Saville, and W.R. Schowalter, *Colloidal Dispersions*. 1989, Cambridge, UK: Cambridge Universtiy Press.

[2] Saltzman, E.J. and K.S. Schweizer, *J.Chem. Phys.*, **2003**, 119(2), 1197.

[3] Schweizer, K.S. and E.J. Saltzman, *J. Chem. Phys.*, **2003**, 119(2), 1181.

[4] Sciortino, F. and P. Tartaglia, *Adv. Phys.*, **2005**, 54(6), 471.

[5] Schweizer, K.S. and E.J. Saltzman, *J. Phys. Chem. B*, **2004**, 108(51), 19729.

[6] Saltzman, E.J. and K.S. Schweizer, *J. Chem. Phys.*, **2003**, 119(2), 1181.

[7] Anderson, B.J. and C.F. Zukoski, *J. Phys.: Cond. Matt.*, **2009**, 21, 285102.

[8] Gopalakrishnan, V. and C.F. Zukoski, *Langmuir*, **2007**, 23, 8187.

[9] Pham, K.N., G. Petekidis, D. Vlassopoulos, S.U. Egelhaaf, P.N. Pusey, and W.C.K. Poon, *Europhys. Lett.*, **2006**, 75(4), 624.

[10] Pham, K.N., G. Petekidis, D. Vlassopoulos, S.U. Egelhaaf, W.C.K. Poon, and P.N. Pusey, *J. Rheol.*, **2008**, 52(2), 649.

[11] Petekidis, G., D. Vlassopoulos, and P.N. Pusey, *J. Phys.: Cond. Matt.*, **2004**, 16(38), S3955.

[12] Petekidis, G., D. Vlassopoulosa, and P.N. Pusey, *Faraday Discuss*, **2003**, 123, 287.

[13] Zhang, R. and K.S. Schweizer, *Phys. Rev. E,* **2009**, 80, 011502.

[14] *Chapter 5*.

[15] Mason, T.G. and D.A. Weitz, *Phys. Rev. Lett.*, **1995**, 75(14), 2770.

[16] Kramb, R.C., R. Zhang, K.S. Schweizer, and C.F. Zukoski, *Phys. Rev. Lett.*, (Accepted June, 2010).

[17] Koumakis, N., A.B. Schofield, and G. Petekidis, *Soft Matter*, **2008**, 4, 2008.

[18] Zaccarelli, E. and W.C.K. Poon, *PNAS*, **2009**, 106(36), 15203.

[19] Mock, E.B., H. De Bruyn, B. Hawkett, R. Gilbert, and C.F. Zukoski, *Langmuir*, **2006**, 22.

[20] Partridge, S.J., *Rheology of Cohesive Sediments*, in *Dept. of Physical Chemistry*. 1985, Bristol University.

[21] Kramb, R.C. and C.F. Zukoski, *Langmuir*, **2008**, 24(14), 7565.

[22] Yatsenko, G. and K.S. Schweizer, *J. Chem. Phys.*, **2007**, 126.

[23] Scott, G.D. and D.M. Kilgour, *J. Phys. D.:Appl. Phys.*, **1969**, 2(6), 863-866.

[24] Donev, A., I. Cisse, D. Sachs, E.A. Variano, F.H. Stillinger, R. Connelly, S. Torquato, and P.M. Chaikin, *Science*, **2004**, 303(5660), 990.

[25] Torquato, S., T.M. Truskett, and P.G. Debenedetti, *Phys. Rev. Lett.,* **2000**, 84(10), 2064.

[26] Schweizer, K.S., *J. Chem. Phys.*, **2007**, 127(16), 164506.

[27] Channell, G.M., K.T. Miller, and C.F. Zukoski, *AIChE Journal*, **2000**, 46(1), 72.

[28] Channell, G.M., *Mechanics of aggregated alumina suspensions: Behavior under shear and compression*, in *Chemical Engineering*. 1999, University of Illinois at Urbana-Champaign: Urbana. p. 133.

[29] Kretser, R.G.d., S.P. Usher, P.J. Scales, D.V. Boger, and K.A. Landman, *AIChE Journal*, **2001**, 47(8), 1758.

[30] Zhou, Z., M.J. Solomon, P.J. Scales, and D.V. Boger, *J. Rheol.*, **1999**, 43(3), 651.

[31] Miller, K.T., R.M. Melant, and C.F. Zukoski, *J. Amer. Cer. Soc.*, **1996**, 79(10), 2545.
[32] Green, M.D., M. Eberl, and K.A. Landman, *AIChE Journal*, **1996**, 42(8), 2308-2318.
[33] Chong, S.-H. and W. Götze, *Phys. Rev. E*, **2002**, 65(5), 051201.
[34] Chong, S.-H. and W. Götze, *Phys. Rev. E*, **2002**, 65(4), 041503.
[35] Pfleiderer, P., K. Milinkovic, and T. Schilling, *Europhys. Lett.*, **2008**(1), 16003.
[36] Letz, M., R. Schilling, and A. Latz, *Phys. Rev. E*, **2000**, 62(4), 5173.
[37] Schilling, R., *Phys. Rev. E*, **2002**, 65(5), 051206.
[38] Chong, S.-H. and W. Kob, *Phys. Rev. Lett.*, **2009**, 102(2), 025702.

Chapter 7 Dynamic Yielding and Discontinuous Shear Thickening in Dense Suspensions of Anisotropic Colloid Particles

7.1 Introduction

A saturated bed of hard, Brownian particles at the random close packing volume fraction, ϕ_{RCP}, must dilate to flow. At slightly lower volume fractions suspensions flow above a dynamic yield stress but, as the shear rate is increased, shear thicken in a manner indicating the suspensions experience flow-induced jamming and are attempting to dilate. At still lower volume fractions, suspensions of hard particles demonstrate liquid-like behavior with well defined zero shear rate viscosities and shear thinning at elevated stresses with no shear thickening. There is thus a range of volume fractions where suspensions of Brownian particles move from being granular solids to being viscous, shear thinning liquids. How suspensions move from solid-like behavior to the liquid state is of great interest as the shear thickening and yield stresses have substantial technological importance and can be engineered through variations in particle interaction potential and particle shape.

One definition of the jammed state for hard, Brownian particles is that volume fraction where the osmotic compressibility and pair distribution function at contact diverge. At this volume fraction, long range self diffusion stops. Here the volume fraction where the suspension is jammed is referred to as ϕ_j noting that $\phi_j=\phi_{RCP}$ for hard particles. It is noted that this definition of jamming presumes that the stress relaxation times diverge at ϕ_j and the suspensions have an amorphous microstructure. For $\phi<\phi_j$, particles are caged by nearest neighbors or attractive interactions and are therefore trapped in a potential energy well and subject to activated motion. As a result, while stress relaxation

times may get very long over small changes in packing fraction, jamming occurs only when there is divergence in the height of the barrier over which activated motion relaxes stress. For spheres, ϕ_j is found experimentally to lie near 0.66[1-3] while ϕ_j passes through a maximum with increasing particle anisotropy. For fused spheres, the maximum lies at a length to diameter (L/D) ratio near 1.4 where ϕ_j~0.72.[2, 4, 5] This end point is less well defined for hard particles experiencing attractions where the jammed state may depend on the suspension's shear history.[6]

For ϕ less than but sufficiently near ϕ_j, the suspensions of hard particles display glassy dynamics where long range self diffusion is constrained by collective rearrangement of particle cages. Within the framework of Nonlinear Langevin Equation modified Mode Coupling Theory, there is a cross over volume fraction, $\phi_c < \phi_j$, where particles become localized by cages of nearest neighbors which produce an entropic dynamic potential.[7, 8] Rearrangement of nearest neighbors requires particle diffusion over a barrier produced by this dynamic potential. The characteristic hoping time, t_{hop}, associated with this diffusive motion over the dynamic potential barrier diverges at ϕ_j. As a result, for $\phi_c < \phi < \phi_j$, when the suspension is deformed at a time scale shorter than the hopping time, the material will display a solid-like response where the linear, low stress storage modulus, G_0' , is larger than the loss modulus G_0''. For a deformation frequency $\omega > 1/t_{hop}$, at low stresses the material responds in the solid-like or elastic manner. With increasing stress, the elastic modulus decreases and at a particular value of stress, $G' = G''$. For larger stresses the suspension responds in a largely liquid-like manner while for smaller stresses the suspension is largely elastic. The stress where $G' = G''$ in stress sweep measurements is called the yield stress, τ_y.[9]

For $\phi < \phi_j$, the onset of dilatent behavior is often referred to as discontinuous shear thickening and is associated with a time average shear rate that is independent of stress. The stress at the onset of thickening, τ_t, is weakly dependent on volume fraction.[10-12] For $\tau > \tau_t$, the suspension shows positive first normal stress differences.[10] and flow behavior is associated with particles intermittently forming structures that bridge the rheometer tool gap.[12-14] The time averaged shear rate when $\tau > \tau_t$ increases as volume fraction decreases and at a volume fraction less than a specific value, ϕ_t, shear thickening is no longer observed.

Continuous shear thickening is distinct from discontinuous thickening. Here, at high shear rates, the viscosity of a suspension increases smoothly to a high shear rate plateau and the suspensions show a negative second normal stress difference. Continuous shear thickening is associated with the formation of hydroclusters and has a hydrodynamic origin.[15-17] A single sample can exhibit either continuous,[11, 17-21] discontinuous,[11, 20, 21] or both kinds of shear thickening behavior,[10] suggesting that they have different origins. In particular, discontinuous shear thickening is associated with an extension of dilatency required to establish continuous shear in beds of particles at ϕ_{RCP}.

Both ϕ_c and ϕ_j show a maximum with increasing anisotropy.[2, 4] As a consequence, the relationship between discontinuous shear thickening and the onset of flow as ϕ_j is approached can be probed by investigating variations in the stresses at thickening with particle shape. Egres and Wagner[11] report a decrease in the minimum volume fraction where *discontinuous* thickening is seen with increasing aspect ratio of ellipsoidal particles. Egres and Wagner investigate aspect ratios of 2-7 that lie in a region where ϕ_j decreases with increasing aspect ratio offering support for the hypothesis that

dilatent behavior is linked to proximity of the jamming transition. Their observations have been confirmed for a wide variety of anisotropic particles which aspect ratios grater that 2.[10, 22-27] In this chapter, the other extreme is explored where ϕ_j increases with degree of anisotropy (L/D<1.4).

Attractions delay the onset of continuous shear thickening.[28] This has been attributed to the growth in stresses required to pull apart attraction induced microstructures which leads to shear thinning at larger stresses thus masking the growing contribution of energy dissipation due to the formation of hydroclusters. The role of attractions in discontinuous shear thickening has seen little investigation.[28, 29]

For suspensions containing non-Brownian particles (several hundred microns in characteristic length) jamming of hard objects is associated with random loose packing and thus for spheres is near ϕ~0.58.[21] Here the definition of jamming is associated with the onset of a static yield stress. When this yield stress is exceeded, the suspensions shear thin and then show discontinuous thickening. At still larger stresses the suspensions show a second region of shear thinning (which has also been reported for suspensions of Brownian particles). The static yield stress is a strong function of volume fraction while the stress at thickening is independent of volume fraction.[30] State diagrams have been developed indicating that the yield stress remains lower than the thickening stress until both are equal to the stress at the second stage of shear thinning at which point the yield stress becomes a constant.[21, 30] Similar state diagrams have been developed at constant volume fraction where the strength of interparticle attractions has been varied by application of electric and magnetic fields.[30]

There are many qualitative similarities in the observed flow of suspensions of non-Brownian and Brownian particles: the independence of τ_t on volume fraction, shear thinning behavior before thickening and the observation of a second shear thinning region (which has been associated with wall slip). One of the major differences lies in definition of jamming. In Brownian suspensions of hard particles, above ϕ_c, the suspensions are glassy but will display a zero shear rate viscosity if deformed at a rate much smaller than $1/t_{hop}$. Thus static yield stresses are not observed until $\phi=\phi_{RCP}$. On the other hand, because the particles are localized in a dynamic potential produced by cages of nearest neighbor particles, the suspensions have a dynamic yield stress as described above. As the strength of short range attractions increases, for $\phi>\phi_c$, suspensions initially become more fluid but at a sufficiently large attraction, suspensions gel. In the gelled state particles are once more localized but this time in wells with an extent defined by range of the interparticle attraction. Again, it is possible to define a dynamic yield stress for gels. This dynamic yield stress is expected to diverge at some volume fraction less than ϕ_{RCP}.[31] As with hard particles, it is expected that τ_y will approach τ_t at some volume fraction begging the question of how cohesive suspensions of Brownian particles move from liquid-like to solid-like behavior as a maximum packing fraction is approached.

In this chapter, the role of particle shape and interaction potential on the initial yielding of suspensions of Brownian particles is explored and observed discontinuous shear thickening to the approach to the solid state are related. In particular it is found that while τ_t is independent of volume fraction, τ_y increases rapidly as volume fraction is raised indicating that at some volume fraction, the stress at thickening will equal the yield stress. For our samples this is extrapolated to occur at a volume fraction just below ϕ_{RCP}.

Above this volume fraction, unless other physical processes intervene, we would expect the material sample to only establish steady flow by dilating. Previous work with non-Brownian glass spheres found a similar crossover of yielding and thickening to occur at a volume fraction of ~0.57, which is near Random Loose Packing (RLP).[21] For the experiments described here with Brownian particles, effective volume fractions where $\tau_y = \tau_t$ will exceed this value and indeed approach Random Close Packing for hard spheres (0.66).[1, 3] This indicates a fundamental difference between Brownian and non-Brownian particles. The hypothesis is tested by investigating the behavior of dense suspensions of spheres and homodicolloid particles composed of fused spheres with an aspect ratio of 1.17. For this aspect ratio and for hard interaction potentials ϕ_j is larger than that of hard spheres. Here variations in the onset of discontinuous shear thickening is explored as one moves from soft short range repulsions to weak short range attractions. In this process, the effect of particle shape and interaction potential on the volume fraction dependencies of stresses at yielding and thickening are explored.

In Section 7.2 of this chapter, the synthesis and sample preparation techniques as well as the details of the rheological experiments are discussed. In Section 7.3.1 the glass transition volume fraction (ϕ_g) for Brownian particles is discussed. Here ϕ_g is extracted from the volume fraction dependence of the linear response elastic and viscous moduli of dynamic stress experiments and is taken as a bound on the localization volume fraction, ϕ_c. In Section 7.3.1 the dynamic yield stress τ_y where $G' = G''$ is also discussed. In Section 7.3.2 the results from continuous shear experiments are described. These experiments show discontinuous shear thickening at τ_t which is found to be independent of volume fraction, ionic strength, and particle shape. Here the implications of the

volume fraction and ionic strength dependence of τ_y and τ_t leading to a point, where $\tau_{y=}\ \tau_t$ is also discussed. A jamming state diagram is developed where the effects of stress, ionic strength, and volume fraction on the ability of dense suspensions to flow are mapped out. Finally in Section 7.4 conclusions are offered on the shear thickening of these dense suspensions.

7.2 Experimental

The particles used in the experiments discussed here are produced in the size range of D=1.0-1.3μm and are synthesized using a multi-step polystyrene emulsion polymerization technique developed by Mock and coworkers[32] The process uses seed particles made from a surfactant-free technique from Homola and coworkers.[33] If seed particles contain divinylbenzene crosslinker (2% by weight, Aldrich - 55% mixture of isomers tech. grade), the resulting final particle shape resembles two overlapping spheres, or a dumbbell shape. If no crosslinker is used in the seed particle synthesis, the resulting final particle is merely a larger sphere particle. These two particle shapes can be seen in the SEM images of Fig 7.1(a, b). The average diameter of sphere particles is 1.14μm while the long axis length of the dicolloids is 1.20μm and the diameter is 1.03μm. The resulting length to diameter (L/D) or aspect ratio of the dumbbell particles was measured to be 1.17, indicating weak anisotropic shape. The particles are stabilized with the adsorption of a nonionic surfactant [$C_{12}E_6$] to the surface (molecule size, δ~4nm) and suspended in an aqueous solution of NaCl at concentrations of 10^{-3}-10^{-2}M. The surface charge of the particles is measured with electrophoresis. The combination of electrostatic charge and van der Waals forces give the full particle interaction energies. Small

differences in the surface potential were found between the S and sDC of the large particles. The total interaction energies of the dicolloids was found to be roughly similar to spheres when an ionic strength 1/2-1/3 that of the sphere particles was used. Therefore spheres suspended at an ionic strength of $3x10^{-3}$M spheres have pair potentials that are approximately equivalent to the dicolloids suspended at an ionic strength of 10^{-3}M .

SEM micrographs were taken using a Hitachi S4700 instrument. One drop of the as-synthesized suspension was placed on a Formvar coated copper grid and attached to a sample holder using conductive tape. Particle dimensions were determined by measuring 50-100 particles from SEM images.

After synthesis, particles are cleaned and concentrated to ϕ~0.35 with dialysis against deionized water. $C_{12}E_6$ and a concentrated solution of aqueous NaCl (0.05-0.1M) is then added to the particle suspension such that the final surfactant concentration is 0.03M (sufficient for monolayer coverage[34]) and the final solvent ionic strength is the desired value. The suspensions are then concentrated further with centrifugation (~1300g) until no supernatant can be removed. The highly concentrated suspension remaining in the centrifuge tube becomes the highest volume fraction sample for a given particle size, particle shape, and solvent ionic strength and is subsequently diluted to obtain lower volume fractions at that condition. Approximate sphere particle interaction energies are calculated from the Hamaker coefficient of polystyrene in water and the measured surface potential from electrophoresis. The results of these calculations are shown in Fig 7.2 for ionic strengths of 10^{-3} $3x10^{-3}$, $5x10^{-3}$ and10^{-2}M. Due to uncertainties in measuring the surface potential, these calculations should only be considered approximate and are adjusted as explained later. An effective particle diameter roughly

based on the separation distance where the potential falls to $1k_BT$ is calculated. The total additional distance is referred to as Δ.

To perform rheological experiments, ~3.2mL of sample is removed from the centrifuge tube and transferred to the cup of a cup-and-bob geometry Bohlin constant stress C-VOR rheometer. A small portion of the sample in the cup is then removed and the wet and dry weight is measured to obtain the sample volume fraction using reported material densities. The samples undergo two types of experiments. First the viscosity is measured as a continuous stress ramp is applied. Samples are presheared at a stress below τ_t for 30s to remove sample inhomogeneities. Data collection times vary with sample volume fraction up to 5min for each stress to allow for steady state to be reached. Solvent evaporation limited longer experiment times. Measurements where $0.9 < d\ln(\dot{\gamma})/dt < 1.1$ were accepted as being at steady state. Up sweep and down sweep experiments showed some hysteresis as samples in the thickened state remain so in the down sweep step for stresses below τ_t. However, repeating the preshear step followed by a second up sweep experiment showed quantitatively similar results demonstrating the reversibility of the shear thickening. All results shown here are from the initial up sweep experiments.

Following the continuous shear experiments and another preshear step, samples undergo oscillatory stress sweeps from ~0.01-1000Pa at a frequency of 1Hz, where the viscous and elastic moduli are measured. Each data point has an integration time of 4s.

The experimental values of stress and moduli are nondimenionalized using a measure of the particle size. The dimensionless stress τ^* is defined as $\tau(D+\Delta)^3/k_BT$ for spheres and $\tau(L+\Delta)^2(D+\Delta)//k_BT$ for dicolloids. Similarly for the dimensionless moduli, $G^*=G(D+\Delta)^3/k_BT$ and $G^*=G(L+\Delta)^2(D+\Delta)/k_BT$ for spheres and dicolloids respectively.

7.3 Results and Discussion

7.3.1 Yielding of nonergodic suspensions

The dynamics of the suspensions studied are essentially identical to those seen in other suspensions of Brownian particles experiencing short range soft repulsions and short range weak attractions.[2] As a result, at low volume fractions these suspensions have well defined zero shear rate viscosities and at intermediate volume fractions shear thin. Above the volume fraction ϕ_c, the suspensions display the behavior of glasses or gels showing dynamic yield stresses. At a maximum packing fraction the elastic modulus and dynamic yield stress appear to diverge. To place the low strain experimental results in context, the data is discussed in terms of a framework established by the nonlinear Langevin equation naïve Mode Coupling Theory, NLE nMCT. In this theory, for $\phi > \phi_c$, particles are localized within a dynamic potential the depth of which grows with volume fraction.[8, 35] ϕ_c, which for hard spheres is approximately 0.43 and for hard dicolloids (L/D=1.17) is approximately 0.46,[4] sets the lower bound for particle localization and is a function of pair potential and particle shape.[4, 5, 8, 35] As ϕ grows above ϕ_c, stress relaxation becomes dominated by diffusion over the dynamic potential barrier. The characteristic time for particles to diffuse over dynamic potential barrier is referred to as the hopping time, t_{hop}, grows dramatically with ϕ. This theory has been developed to describe the properties of suspensions at rest or weakly deformed although extensions to continuous deformations have been made.[36] This model has seen numerous experimental tests, in particular predicted scaling of elastic modulus with volume fraction for hard spherical and anisotropic particles[1, 2] and the effects of weak attractions on yielding[37] and it is used here to frame discussion of the experimental results.[38]

In Fig 7.3(a-d) and 7.4(a-d) examples of G'^* and G''^* are shown as functions of stress for two representative volume fractions at ionic strengths of 10^{-3}, $3x10^{-3}$, $5x10^{-3}$ and 10^{-2}M and for both particle shapes. The experimental dynamic glass transition volume fraction, ϕ_g, is defined for the systems as the volume fraction where $G_0'=G_0''$ at a frequency of 1Hz. Here G_0' and G_0'' are the limiting low stress storage and loss moduli respectively, as shown in Figs. 7.3 and 7.4. In the language of NLE nMCT, ϕ_g is the dynamic glass transition where t_{hop} grows to approach the deformation time of 2πs.[2] Previous studies showed that for ~300 nm diameter hard sphere particles, ϕ_g/ϕ_c~ 1.3. ϕ_g is found by plotting the linear response elastic and viscous moduli as a function of volume fraction. By fitting an exponential equation to this data, one can extrapolate to the volume fraction where $G'=G''$.[2] This is demonstrated in the inset of Fig 7.5.

The main panel of Fig. 7.5 shows the location of ϕ_g for as a function of ionic strength for each particle shape. Both particle shapes display a reentrant state diagram where increasing ionic strength first increases ϕ_g while further increases in ionic strength lead to weak interparticle attractions which cause a maximum or nose in ϕ_g to develop. Larger increases in ionic strength lead stronger attractions and the formation of gels. Although both spheres and dumbbells show a region where ϕ_g decreases with increasing ionic strength, at $5x10^{-3}$M the minimum in the pair potential is on the order of $1k_BT$. Values of ϕ_g are also given in Table 7.1. While ϕ_g varies by 0.03-0.04 for spheres and dumbbells over the ionic strength range explored, the impact on the modulus is substantial. For example for spheres, at a volume fraction of ~0.56, $G_0'^*$ has values of $3x10^4$, $2x10^4$, $3x10^3$, and $3x10^4$ for ionic strengths of 10^{-3}, $3x10^{-3}$, $5x10^{-3}$, and 10^{-2} respectively.

Above ϕ_g, G_0' increases in an exponential manner with volume fraction where one sees similar volume fraction dependencies for spheres and dumbbells at all ionic strengths. The particles suspended at low ionic strengths experience soft repulsions with an extent that is a small fraction of the particle diameter. As a result at volume fractions where the double layers do not substantially overlap, the expectation is for the suspensions to behave as if they are hard objects with a small increase in size to account for the double layer repulsions.[2, 39]

Previous studies have shown that under these conditions, $G_0'^*$ data taken at different ionic strengths scales as ϕ^{*4} where $\phi^*=1/(\phi_{RCP}-\phi_{eff})$.[1, 3] $\phi_{eff}= \phi(1+\Delta/D)^3$ is defined as the effective hard sphere volume fraction. This treatment is motivated by the predictions of nMCT which indicates that G_0' should diverge at ϕ_j as $g(D)^2$ where $g(D)$ is the value of the pair distribution function at contact. For hard objects $g(D)$ diverges as ϕ^{*2}, and for hard spherical particles, ϕ_{RCP} = 0.66. The same scaling was found for anisotropic particles if ϕ_{RCP} was taken as an aspect ratio dependent parameter. In the inset of Fig 7.6, $G_0'^*$ is plotted as a function of ϕ^* for low ionic strengths where pair potentials will best experience hard interactions: 10^{-3}M and $3x10^{-3}$M for spheres and 10^{-3}M dicolloids) with $\phi^*=1/(\phi_{RCP}-\phi_{eff})$. Here, the data collapses along a line showing $G_0'^{\sim}\phi^{*4}$ (except for the high values of ϕ^*) in agreement with previous studies. The flattening of the modulus data at high ϕ^* is attributed to reaching volume fractions where particle interactions are no longer effectively hard as would be expected as electrostatic double layers begin to substantially overlap. The effective hard sphere collapse of the $G_0'^*$ data confirms that for hard spheres ϕ_{RCP}= 0.66 while for hard dicolloids with L/D=1.17 ϕ_{RCP} =

0.68. These represent upper bounds on the packing of the hard spheres and hard dicolloids and these are plotted as vertical lines in Fig. 7.5.

Additional work with smaller particles suggests a similar scaling collapses the volume fraction dependencies of attractive particles where ϕ_{RCP} is replaced with ϕ_{max}. This new term ϕ_{max} is lower than ϕ_{RCP} as effective volume fraction is also now replaced with the measured volume fraction which accounts only for the core particle and the surfactant and not the effects of the soft double layer. ϕ_{max} depends on the strength of attraction and shows a similar reentrant-type shape as ϕ_g.[40] With the success of the low ionic strength results using ϕ_{eff} and ϕ_{RCP} based on the work from chapter 5, the same procedure is applied for determining an ionic strength dependent $\phi_{max.}$ The exponential dependence of $G_0'^*$ on ϕ^* and exponent of 4 is used to find values of ϕ_{max} that result in the best collapse. In the main panel of Fig. 7.6, the results of this procedure are shown with $G_0'^*$ as a function of ϕ^*, where $\phi^*=1/(\phi_{max}-\phi)$ for all ionic strengths. In Fig. 7.5 the values of ϕ_{max} that yield collapse from Fig. 7.6 are shown noting that these values lie below those expected for hard objects and thus represent lower bounds on the volume fractions where suspensions would jam. Except for spheres at 10^{-2}M (where there are large uncertainties due to measurement of only two volume fractions) one sees a similar shape to ϕ_{max} as ϕ_g. Values of ϕ_{max} are also given in Table 7.1.

Samples studied here are at volume fractions above ϕ_c. As a result, at 1Hz the materials display glassy dynamics. At frequencies $\omega << 2\pi/t_{hop}$ terminal, liquid like flow will be observed. For such systems, yielding - the existence of a stress below which the samples will deform elastically but not creep - results from observations at time scales shorter than t_{hop}. For frequencies greater than $2\pi/t_{hop}$, stresses lower the dynamic barrier

allowing activated stress relaxation. At these frequencies, for $\tau<\tau_y$, particles remain caged by nearest neighbors or by interparticle bonds produced by attractions. For $\tau>\tau y$ the barrier is low enough such that on the time scale for the deformation there is substantial rearrangement of nearest neighbors and the sample is liquid-like. In a dynamic stress sweep at a frequency of 1Hz, the stress required to lower the dynamic potential barrier to a point where $t_{hop}\sim 2\pi$ s is characterized by defining the dynamic yield stress, τ_y*, as that stress where $G'^*=G''^*$ for each volume fraction above ϕ_g. τ_y* has a strong volume fraction dependence, reaching a value of ~10^3 for the highest volume fraction samples.

A summary of τ_y* for both particle shapes and all ionic strengths in Figure 7.7 where one observes approximately exponential increases in τ_y* with the same slopes independent of volume fraction and ionic strength. As found for the plateau modulus, $\tau_y^*\sim\phi^{*4}$ (Fig. 7.8). suggesting that without the inception of additional physics, such as substantial double layer overlap, particle deformation, or wall slip in the rheometer, the elastic modulus and the dynamic yield stress to diverge at ϕ_{max}.

7.3.2 Shear Thickening

Steady viscosities as a function of applied stress are shown in Figs 7.9(a-d) for spheres and in Figs 7.10(a-d) for dicolloid particles. The zero shear rate region cannot be probed because of long relaxation times. This is caused by both high volume fractions where particles experience large dynamic potential barriers and because the particles are large such that the limiting diffusivity at zero volume fraction is small on an absolute scale. As a result, in the accessible low limit stress range, only shear thinning is observed.

At low volume fractions, the samples shear thin towards what appears to be a high shear rate plateau viscosity. Above a critical volume fraction, ϕ_t, shear thinning is interrupted by discontinuous shear thickening and dilatent behavior. The volume fractions above and below ϕ_t are shown in Table 7.1. While $\phi_t > \phi_g$, both volume fractions are weakly dependent on ionic strength.

As shown in Fig 7.9a in the thickening region the viscosity increases linearly with stress indicating that the shear rate is independent of applied stress. The stress at the minimum of viscosity, is taken as stress at thickening τ_t^*, and is relatively constant as volume fraction and ionic strength are raised. Indeed, this stress is constant for both particle shapes. For the two lowest ionic strengths, the shear thinning region of the data below τ_t^* is steeper than for the higher ionic strengths. The lower viscosity at higher ionic strengths is attributed to better screening of the electrostatic double layer and reduced effective particle size and effective volume fraction.

The onset of thickening behavior is more consistent and better defined for the lower ionic strengths. There is a sharp, discontinuous increase in viscosity above τ_t^*, and the minimum viscosity point shifts only between two values of stress (2.5×10^4 and 3.6×10^4) for all volume fractions. At the higher ionic strengths, the point of minimum viscosity is broader and is found with in a larger range stress between 1.1×10^4 and 3.6×10^4. However there is no clear volume fraction dependence on τ_t^* and no clear dependence on pair potential despite the absolute viscosity being dependent on both changes in volume fraction and pair potential.

The results for dicolloid suspensions are qualitatively similar. At 10^{-3}M, the approach to τ_t^* is considerably steeper than at higher ionic strengths. The sharp point at the

minimum in viscosity is apparent at 1, 3 and $5x10^{-3}$M while at 10^{-2}M, thickening is not as abrupt and is similar to the spheres at the two higher ionic strengths. Also similar to the spheres, the variation in τ_t^* is smaller with the three lower ionic strength samples, where the minimum in viscosity is found at a dimensionless stress between $1.6x10^4$ and $3.4x10^4$. At 10^{-2}M, the lower range of τ_t^* drops to $1.1x10^4$. As with spheres, despite clear changes in suspension viscosity associated with suspension volume fraction and pair potential as modulated by ionic strengths, the stress at thickening is very insensitive to these variables.

In the inset of Figure 7.11 the values of τ_t^* for spheres and dicolloids is summarized. All shear thickening stress values fall within a narrow range of the total window of stress used in the experiments. Additionally, no dependencies on ionic strength or particle shape are distinguishable. Values of τ_t^* are plotted as a function of ϕ^* in the main panel of Fig 7.11 along with τ_y^* from the previous discussion. By extension of the line for τ_y^*, one finds that $\tau_t^*=\tau_y^*$ at approximately ϕ^*=70-100. Therefore one expects the thickening and yield stresses to be equal at a volume fraction about 0.014-0.01 below ϕ_{max} for each shape and ionic strength. A flattening in the yield stress curves as ϕ^* increases above 50 has been previously discussed. This behavior is attributed to the introduction of new physics controlling the mechanics of the suspensions such as substantial overlap of double layers, particle deformation or wall slip. In practical terms, these new deformation mechanisms will delay the point where suspensions will dilate prior to yielding. For the samples it is surmised that $\tau_t^*=\tau_y^*$ at a volume fraction of (ϕ_{RCP}-0.015) or larger.

7.4 Conclusion

From stress sweep experiments, two qualitatively different quantities for dense suspensions of spherical and dicolloid particles are extracted. First an experimental glass transition volume fraction ϕ_g is determined from the linear response behavior and determine the volume fraction, pair potential and shape dependencies of the limiting low strain elastic modulus for $\phi > \phi_g$. In keeping with previous experiments on smaller particles where it is observed that $G_0'^* \sim \phi^{*4}$. Secondly a yield stress is defined at the stress where for $\phi > \phi_g$, $G'=G''$. The yield stress shows a strong volume fraction dependence with a magnitude that is sensitive to ionic strength and particle shape. The differences in yield stress can be collapsed by using a volume fraction scaling procedure shown to be successful with hard particles. The yield stress follows similar scaling as the linear elastic modulus where $\tau_y^* \sim \phi^{*4}$. From the collapse of G_0^* and τ_y^* with $\phi^*=1/(\phi_{max}-\phi)$ it is found that $\phi_g < \phi_{max} < \phi_{RCP}$ of hard particles. The changes in ϕ_{max} with ionic strength and particle shape mirror those of ϕ_g.

In a second type of experiment, the stress is continuously applied and the viscosity of the suspension is measured. In these experiments, above a critical volume fraction, we observe shear thickening and dilatency. The stress at the onset of this type of flow behavior is weakly dependent on changes to particle interaction, particle shape, and volume fraction. When yield stress and the stress at thickening are plotted together, an apparent crossover point is projected to occur at $\phi^* \sim 70\text{-}100$, or ~0.014-0.01 below ϕ_{max}. For ϕ^* larger than this cross over volume fraction, an elastic modulus would be measured and be related to particle caging and details of the dynamic potential but steady flow could not be established without the suspension dilating. The volume fraction where the

dynamic yield stress equals the stress at thickening for the Brownian particles studied here is significantly higher than for non-Brownian glass spheres.[21]

The collapse of modulus and yield stress data on ϕ^* indicates that the particles are sufficiently hard that these parameters diverge with the pair distribution function at contact. As the volume fraction approaches ϕ_{max}, these conditions are violated such that alternative mechanisms of stress relaxation become important. Experimentally this results in delay to higher volume fractions the point where $\tau_y^* = \tau_t^*$. For the systems studied, mechanisms of stress relaxation that enable steady flow at stresses below τ_t^* appear in factors controlling zero strain modulus and dynamic yield stress such as double layer overlap, particle deformation or wall slip before they are observed in changes to τ_t^*. The results suggest however that if there is a volume fraction region below ϕ_{max} where steady flow cannot occur without dilation, it will be at volume fractions $>0.97\phi_{max}$.

7.5 Figures and Tables

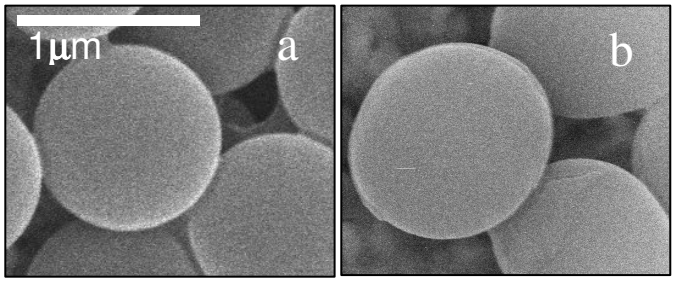

Figure 7.1. SEM Images of particles used in this chapter

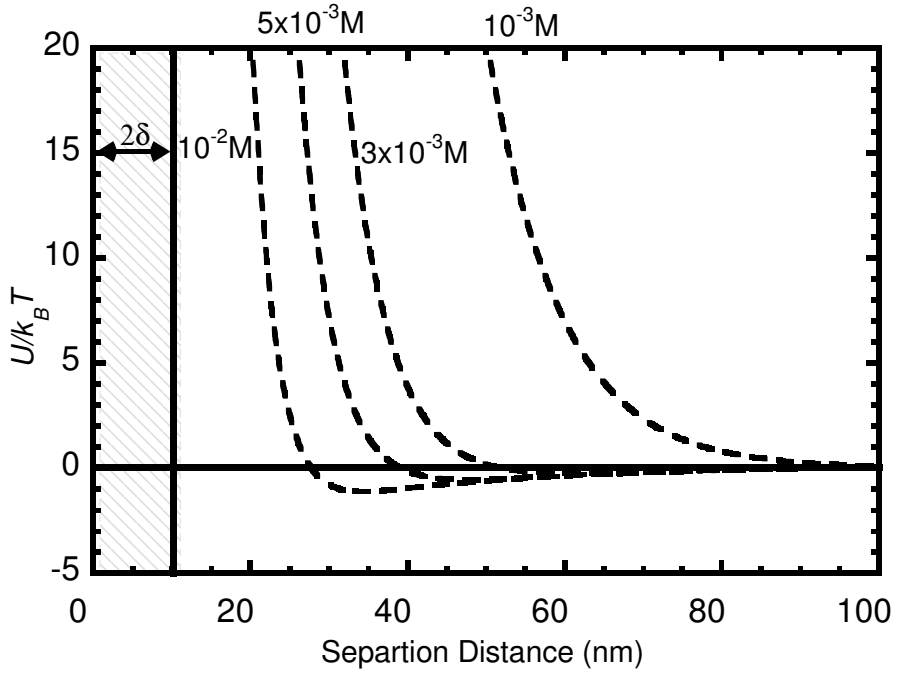

Figure 7.2. Approximate pair interaction potentials calculated from van der Waals and electrostatic forces.

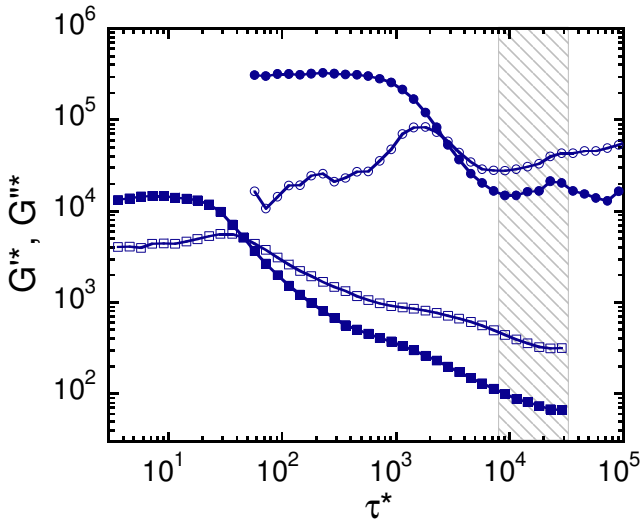

(a)

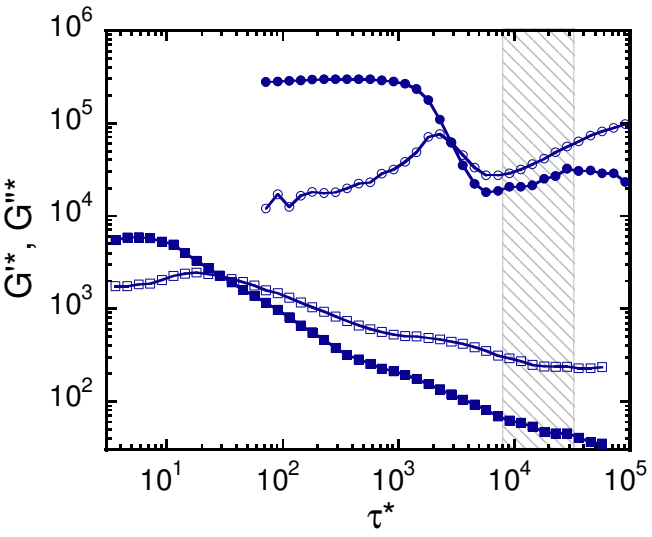

(b)

Figure 7.3 (continued on next page)

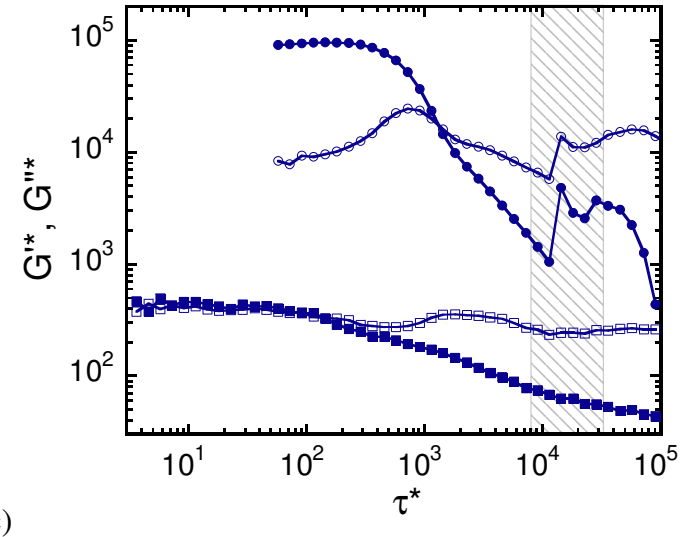

(c)

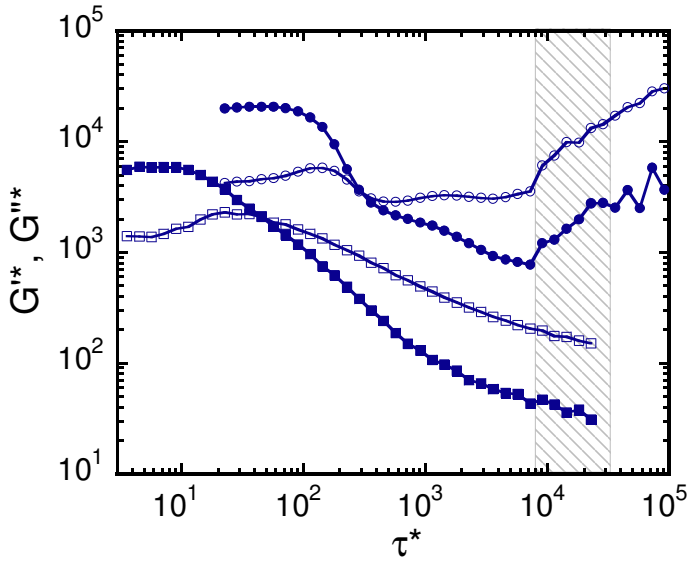

(d)

Figure 7.3. Dynamic stress sweep experiments where *G'** and *G"** are plotted as a function of τ^* for sphere particle suspensions. The grey box indicates the range of stresses at the onset of shear thickening from continuous stress experiments described in Section 7.3.2. Ionic strengths are 10^{-3}M (a), $3x10^{-3}$M (b), $5x10^{-3}$M (c), 10^{-2}M (d). The volume fractions for each sample are 0.553 and 0.584 (a), 0.541 and 0.589 (b), 0.550 and 0.585 (c), 0.521 and 0.577 (d).

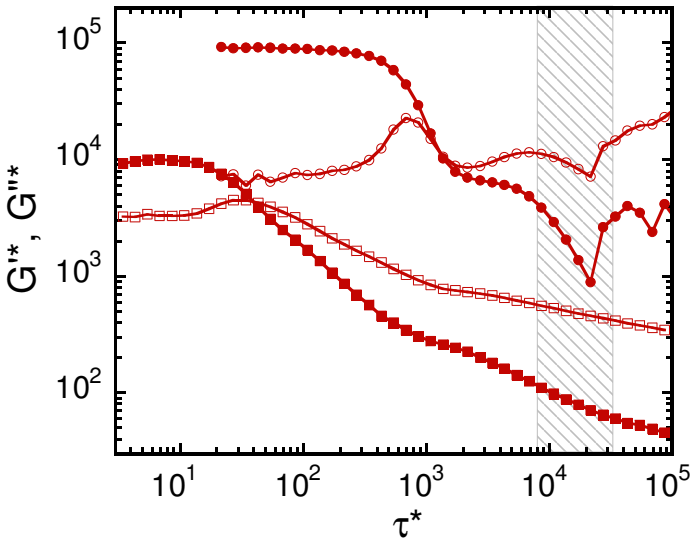

(a)

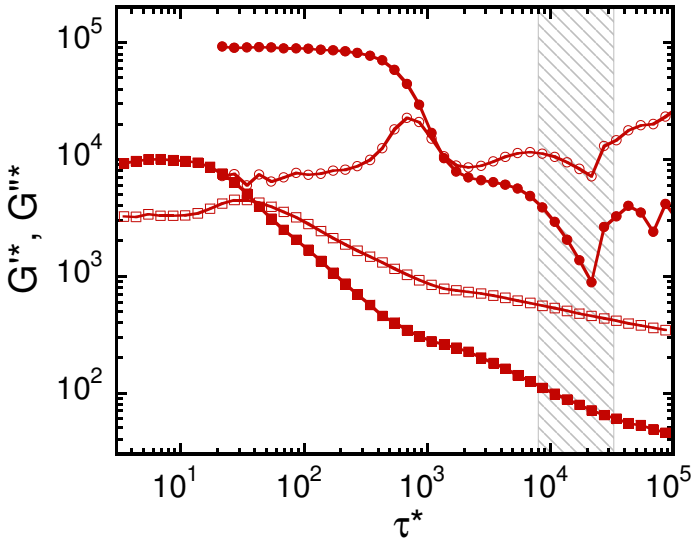

(b)

Figure 7.4 (continued on next page)

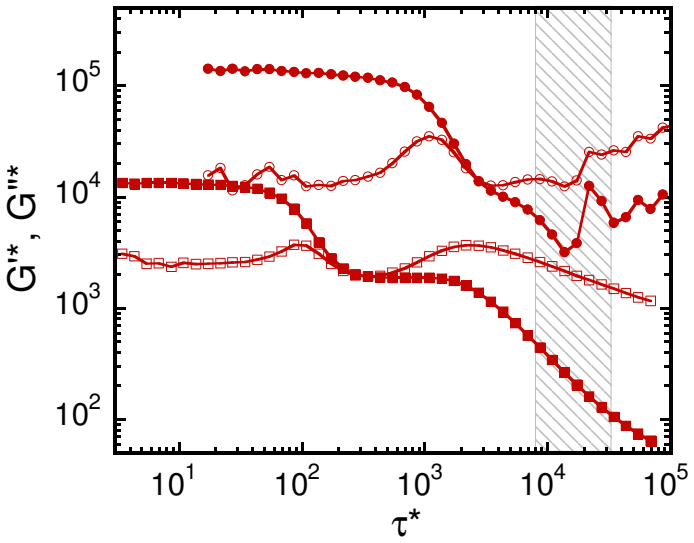

(c)

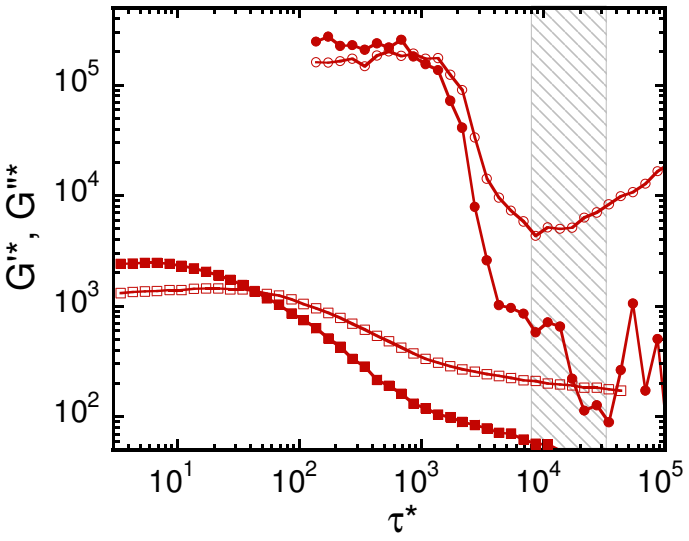

(d)

Figure 7.4. Dynamic stress sweep experiments where *G'** and *G"** are plotted as a function of τ^* for dicolloid particle suspensions. The grey box indicates the range of stresses at the onset of shear thickening from continuous stress experiments described in Section 7.3.2. Ionic strengths are 10^{-3}M (a), $3\text{x}10^{-3}$M (b), $5\text{x}10^{-3}$M (c), 10^{-2}M (d). The volume fractions for each sample are 0.568 and 0.611 (a), 0.554 and 0.611 (b), 0.592 and 0.618 (c), 0.545 and 0.584 (d).

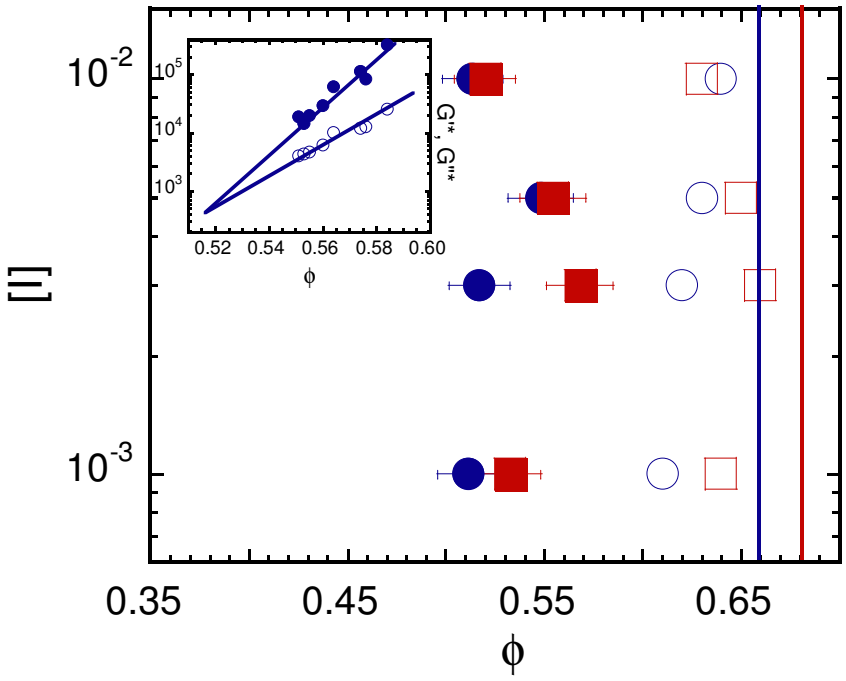

Figure 7.5. Dynamic state diagram indicating the location of ϕ_g for each ionic strength and particle shape with closed points. Error bars indicate uncertainties from extrapolation of linear moduli data. The volume fraction ϕ_{max} is also shown as open points, and ϕ_{RCP} for hard spheres and dicolloids are shown as a vertical line at 0.66 and 0.68 respectively. Inset shows exponential fit to $G_0'^*$, $G_0''^*$ vs ϕ demonstrating procedure to calculate ϕ_g.

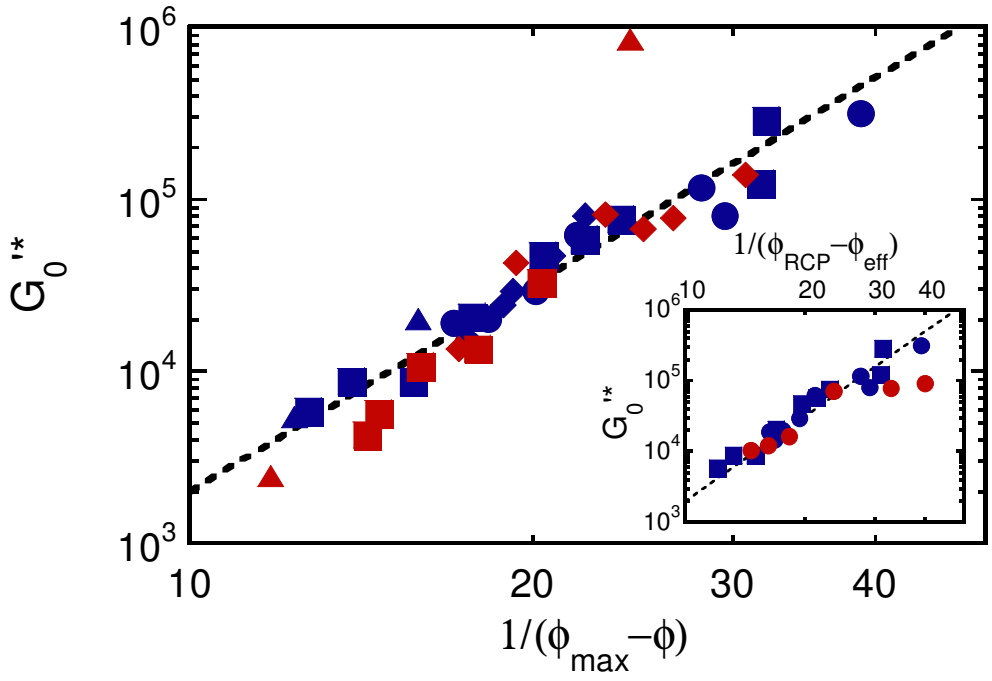

Figure 7.6. $G_0'^*$ as a function of ϕ^* for all ionic strengths with $\phi^*=1/(\phi_{max}-\phi)$. Spheres are shown in blue and dicolloids in red. Ionic strengths are 10^{-3}M (circles), $3\text{x}10^{-3}$M (squares), $5\text{x}10^{-3}$M (diamonds) and 10^{-2}M (triangles). A line of slope 4 is shown to demonstrate theoretical prediction of $G_0'^* \sim \phi^{*4}$. Inset – $G_0'^*$ as a function of ϕ^* for low ionic strength conditions with $\phi^*=1/(\phi_{RCP}-\phi_{eff})$.

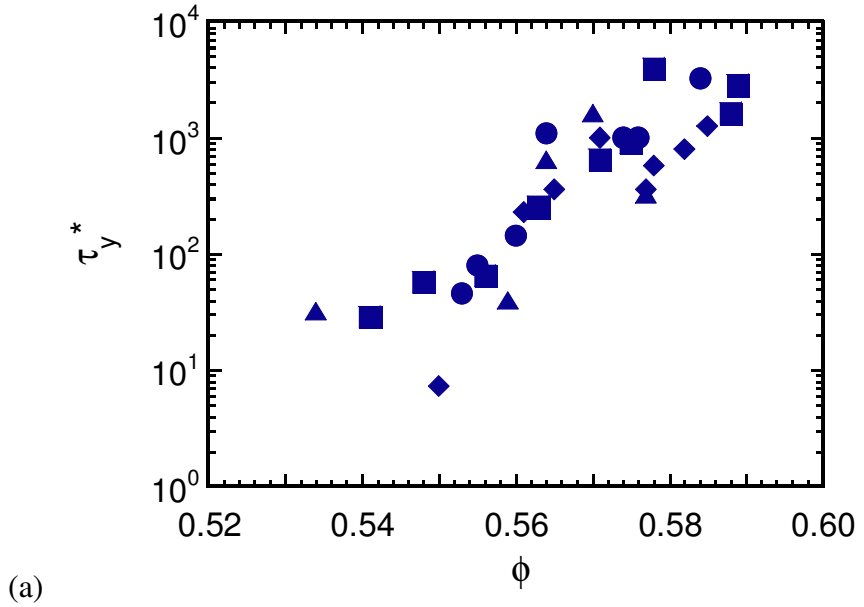

(a)

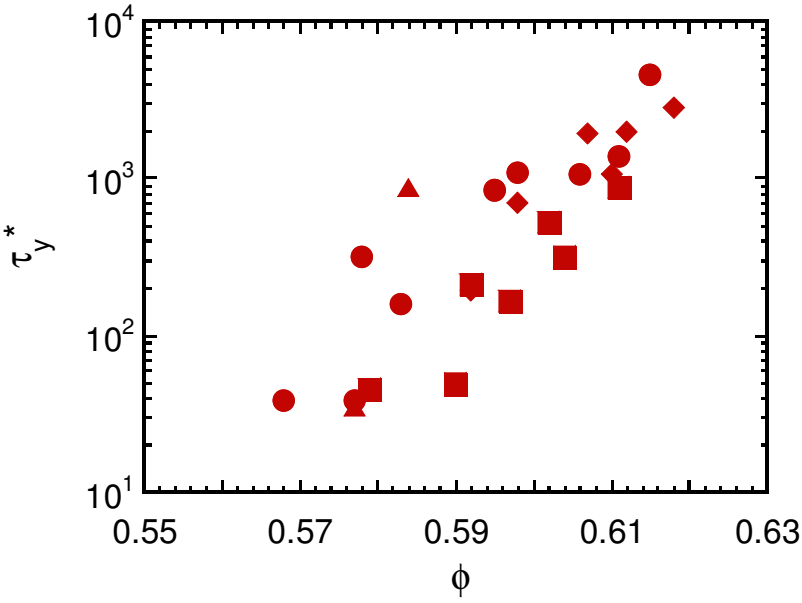

(b)

Figure 7.7. Dynamic yield stress as a function of volume fraction for spheres (a, blue) and dicolloids (b, red). Ionic strengths are 10^{-3}M (circles), $3x10^{-3}$M (squares), $5x10^{-3}$M (diamonds), 10^{-2}M (triangles).

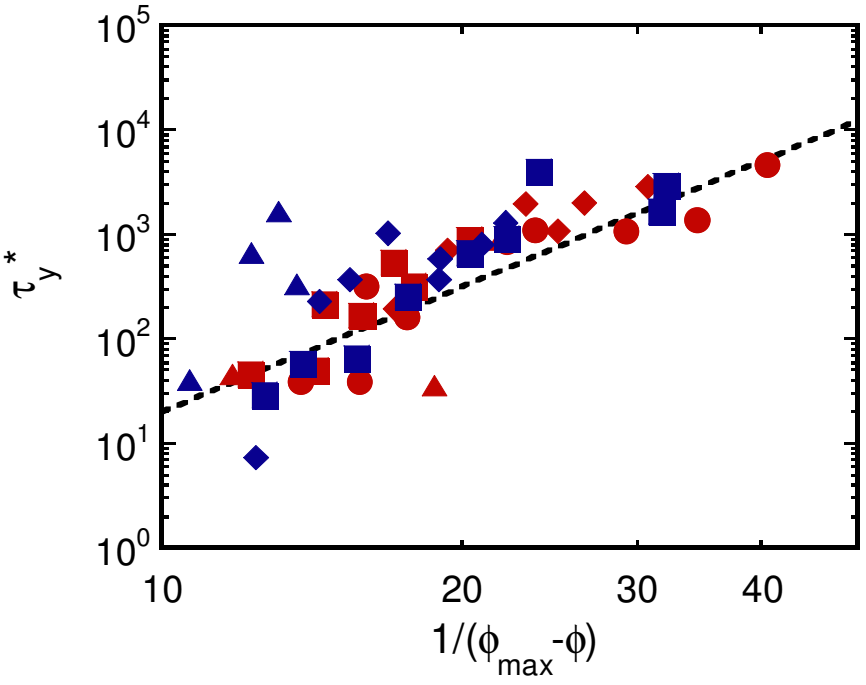

Figure 7.8. τ_y* as a function of ϕ* where ϕ*=1/(ϕ_{max}-ϕ). Sphere suspensions are shown in blue and dicolloid suspensions in red. Ionic strengths are 10^{-3}M (circles), $3x10^{-3}$M (squares), $5x10^{-3}$M (diamonds), 10^{-2}M (triangles).A line of slope 4 is drawn to indicate nMCT prediction of the dependence of absolute yield stress on ϕ*.

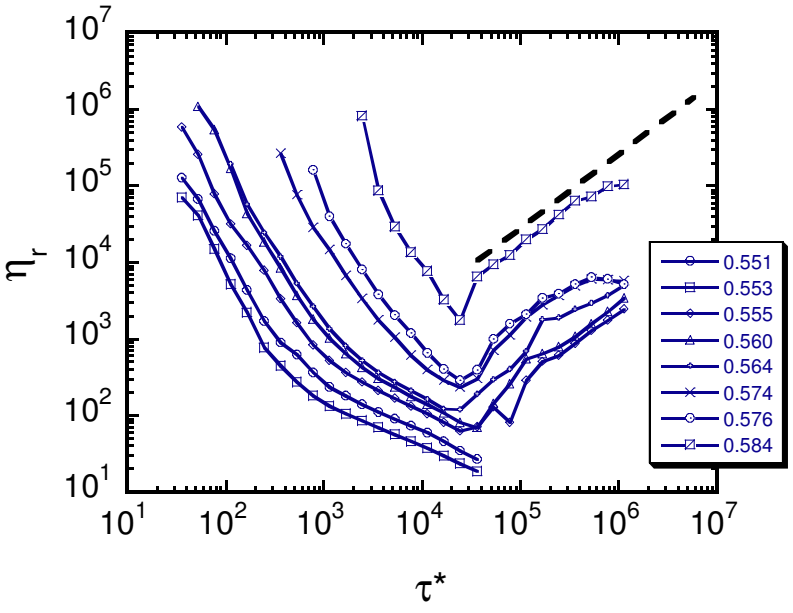

(a)

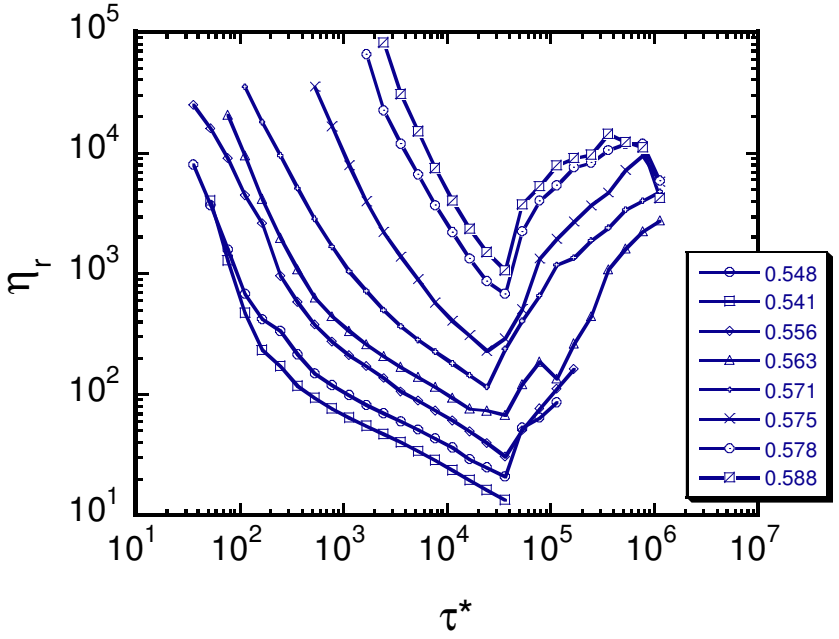

(b)

Figure 7.9 (continued on next page)

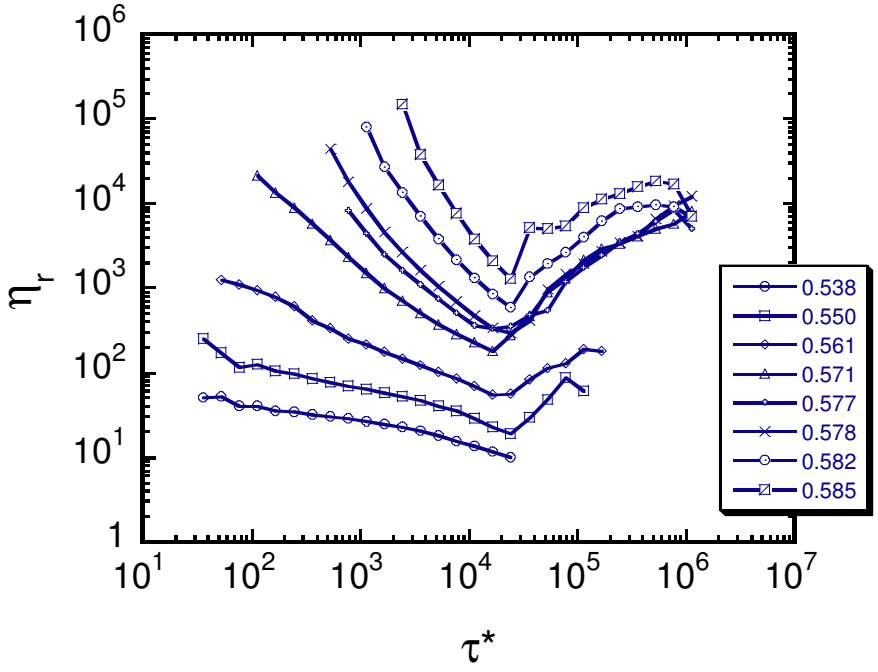

(c)

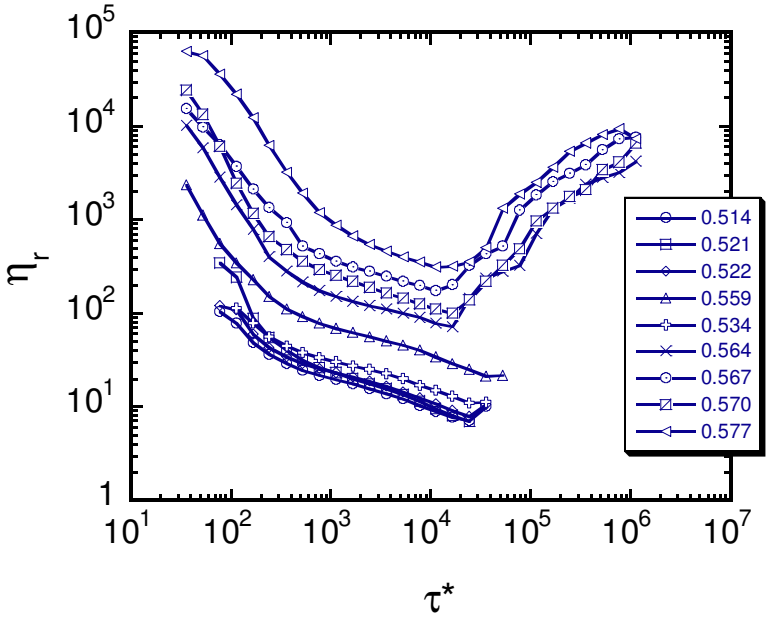

(d)

Figure 7.9. Viscosity as a function of stress for spheres. Ionic strengths are 10^{-3}M (a) (A line of slope one is drawn to indicate constant shear rate and discontinuous shear thickening), $3x10^{-3}$M (b), $5x10^{-3}$M (c), 10^{-2}M (d).

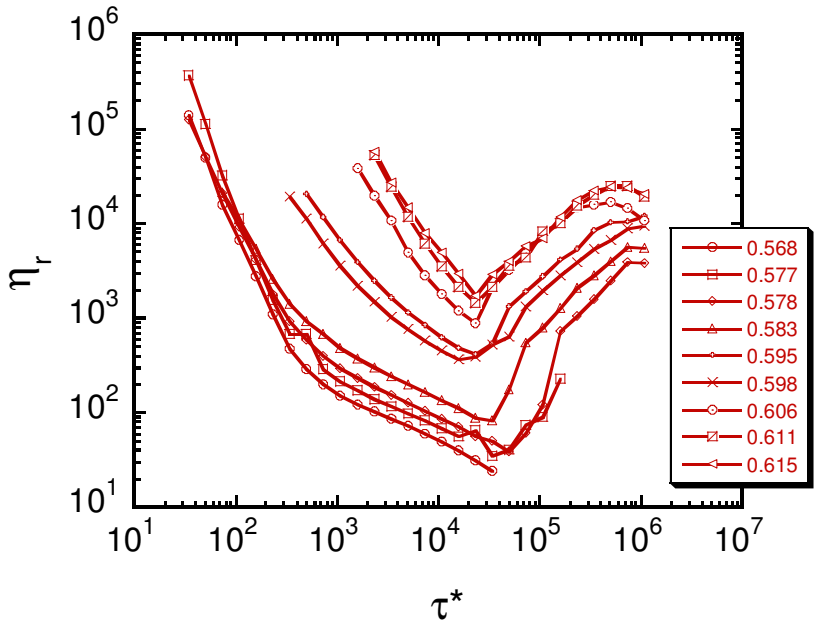

(a)

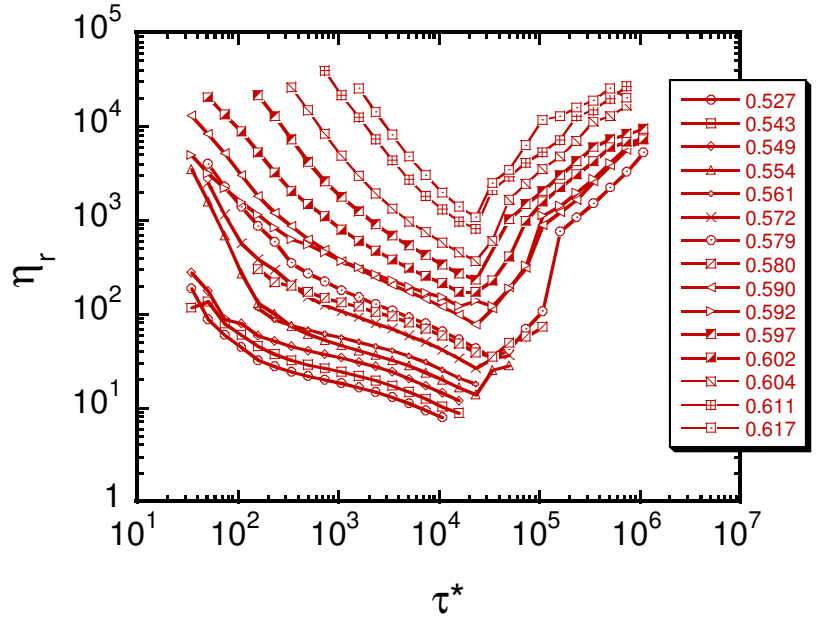

(b)

Figure 7.10 (continued on next page)

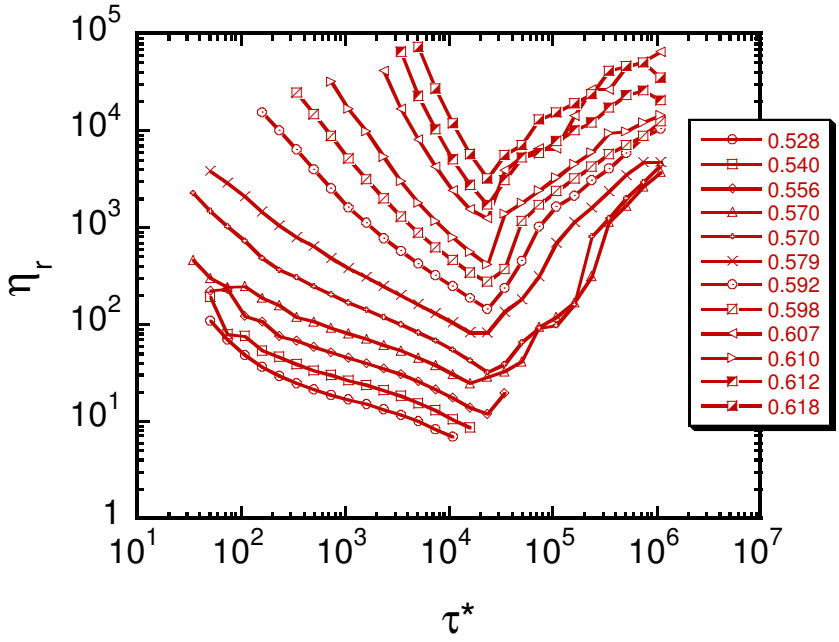

(c)

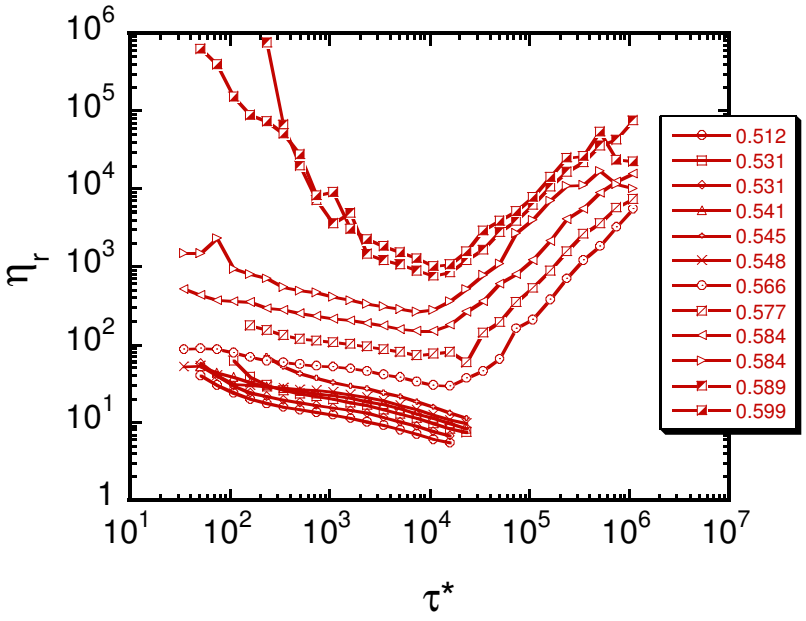

(d)

Figure 7.10. Viscosity as a function of stress for spheres. Ionic strengths are 10^{-3}M (a) (A line of slope one is drawn to indicate constant shear rate and discontinuous shear thickening), $3x10^{-3}$M (b), $5x10^{-3}$M (c), 10^{-2}M (d).

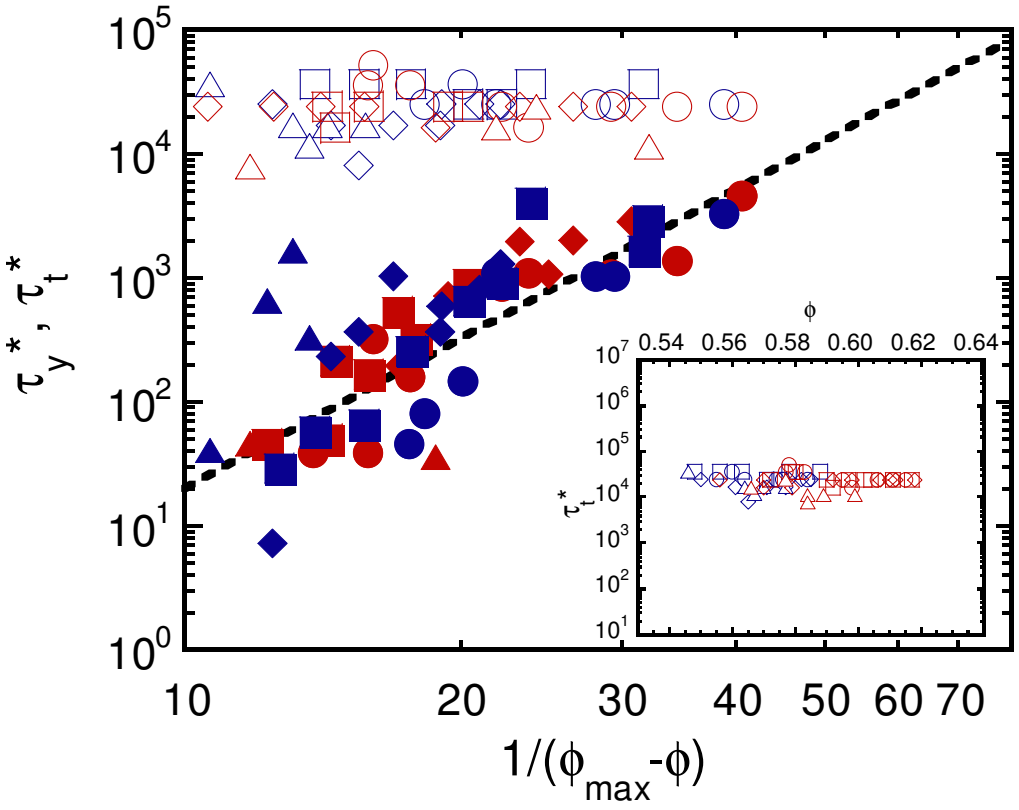

Figure 7.11. τ_y^* (closed points) and τ_t^* (open points) as a function of ϕ^*. The dashed line of slope 4 shows predicted scaling and indicates where the intersection of τ_t^* and τ_y^* would occur if there were no changes to the fundamental physics at short separation distances, at approximately ϕ^*=70-100. In experiments double layer overlap and slip begin to influence results at ϕ^*>~50. Inset shows τ_t^*as a function of absolute volume fraction indicating a near constant shear thickening stress over all experimental conditions.

[I] (M)	ϕ_g	ϕ_t lower	ϕ_t upper	ϕ_{max}
Spheres				
10^{-3}	0.51	0.551	0.555	0.61
$3x10^{-3}$	0.52	0.541	0.548	0.62
$5x10^{-3}$	0.55	0.538	0.550	0.63
10^{-2}	0.51	0.534	0.546	0.64
Dicolloids				
10^{-3}	0.53	0.568	0.577	0.64
$3x10^{-3}$	0.57	0.561	0.572	0.66
$5x10^{-3}$	0.55	0.540	0.570	0.65
10^{-2}	0.52	0.548	0.566	0.63

Table 7.1. Values for ϕ_g, lower and upper bound of ϕ_t, and ϕ_{max}

7.6 List of References

[1] Koumakis, N., A.B. Schofield, and G. Petekidis, *Soft Matt.*, **2008**, 4, 2008.
[2] Kramb, R.C., R. Zhang, K.S. Schweizer, and C.F. Zukoski, *Phys. Rev. Lett.*, Accepted June, 2010.
[3] Schaertl, W. and H. Sillescu, *J. of Stat. Phys.*, **1994**, 74(3), 687.
[4] Yatsenko, G. and K.S. Schweizer, *J. Chem. Phys.*, **2007**, 126.
[5] Zhang, R. and K.S. Schweizer, *Phys. Rev. E,* **2009**, 80, 011502.
[6] Channell, G.M., *Mechanics of aggregated alumina suspensions: Behavior under shear and compression*, in *Chemical Engineering*. 1999, University of Illinois at Urbana-Champaign: Urbana. p. 133.
[7] Saltzman, E.J. and K.S. Schweizer, *J. Chem. Phys.*, **2003**, 119(2), 1197..
[8] Schweizer, K.S. and E.J. Saltzman, *J. Chem. Phys.*, **2003**, 119(2), 1181.
[9] Anderson, B.J. and C.F. Zukoski, *J. of Phys.: Cond. Matt.*, **2009**, 21, 285102.
[10] Larsen, R.J., J.-W. Kim, C.F. Zukoski, and D.A. Weitz, *Phys. Rev. E*, **2010**, 81, 011502.
[11] Egres, R.G. and N.J. Wagner, *J. Rheol.*, **2005**, 49(3), 719.
[12] Maranzano, B.J. and N.J. Wagner, *J. Chem. Phys.*, **2001**, 114(23), 10514.
[13] Chow, M.K. and Z.C. F., *J. Rheol.*, **1994**, 39(1), 15.
[14] Franks, G.V., Z. Zhou, N.J. Duin, and D.V. Boger, *J. of Rheol.,* **2000**, 44(4), 759.
[15] Wagner, N.J. and J.F. Brady, *Physics Today*, **2009**.
[16] Melrose, J.R. and R.C. Ball, *J. Rheol.,* **2004**, 48(5), 961.
[17] Bender, J.W. and N.J. Wagner, *J. Rheol.*, **1996**, 40(5), 899.
[18] Boersma, W.H., J. Laven, and H.N. Stein, *AIChE Journal*, **1990**, 36(3), 321.
[19] Kogan, M., C.J. Dibble, R.E. Rogers, and M.J. Solomon, *J. Coll. Inter. Sci.,* **2008**, 318, 252.
[20] D'Haene, P., J. Mewis, and G.G. Fuller, *J. Coll. Inter. Sci.*, **1993**, 156, 350.
[21] Brown, E. and H.M. Jaeger, *Phys. Rev. Lett*, **2009**, 103, 086001.
[22] Clarke, B., *Trans. Inst. Chem. Eng.*, **1967**, 45, 251.
[23] Beazley, K.M., *Industrial aqueous suspensions*, in *Rheometry: Industrial Applications*, K. Walters, Editor. 1980, Research Studies Press: Chichester. p. 339.
[24] Alince, B. and P. LePoutre, *Tappi J.*, **1983**, 66(11).
[25] Lee, D.I. and A.S. Reder. *The rheological properties of clay suspensions, latexes and clay-latex systems*. in *TAPPI Coating Conference*. 1972. San Francisco, CA.
[26] O'Brien, V.T. and M.E. Mackay, *J. Rheol.*, **2002**, 46, 557.
[27] Bergstrom, L., *J. Mat. Sci.*, **1996**, 31(19), 5257.
[28] Gopalakrishnan, V. and C.F. Zukoski, *J. Rheol.,* **2004**, 48(6), 1321.
[29] Osuji, C.O., C. Kim, and D.A. Weitz, *Phys. Rev. E*, **2008**, 77(6), 060402.
[30] Brown, E., N.A. Forman, C.S. Orellana, H. Zhang, B.W. Maynor, D.E. Betts, J.M. DeSimone, and H.M. Jaeger, *Nat. Mat.,* **2010**, 9(3), 220.
[31] *Chapter 5*.
[32] Mock, E.B., H. De Bruyn, B. Hawkett, R. Gilbert, and C.F. Zukoski, *Langmuir*, **2006**, 22.
[33] Homola, A.M., M. Inoue, and A.A. Robertson, *J. App. Polymer Sci.*, **1975**, 19, 3077.

[34] Kramb, R.C. and C.F. Zukoski, *Langmuir*, **2008**, 24(14), 7565.
[35] Saltzman, E.J. and K.S. Schweizer, *J. Chem. Phys.*, **2003**, 119(2), 1181.
[36] Holmes, C.B., M.E. Cates, M. Fuchs, and P. Sollich, *J. of Rheol.*, **2005**, 49(1), 237.
[37] Gopalakrishnan, V. and C.F. Zukoski, *Langmuir*, **2007**, 23, 8187.
[38] Guo, H., S. Ramakrishnan, J.L. Harden, and R.L. Leheny, *Phys. Rev. E*, **2010**, 81(5), 050401.
[39] Bryant, G., S.R. Williams, L. Qian, I.K. Snook, E. Perez, and F. Pincet, *Phys. Rev. E*, **2002**, 66(6), 060501.
[40] *Chapter 4*.

Chapter 8 Conclusions

8.1 Summary

In this thesis, the effects of particle shape, size and interaction on the rheological behavior of dense suspensions has been studied. Particles were synthesized from polymerizing styrene monomer within an emulsion reaction. Additional polymerization steps using the original particles as seeds, resulted in anisotropically shaped final particles. Depending on the size of the seed particle, two size ranges were produced. The final approximate equivalent diameter of the first set of spherical and anisotropic particles was 200-300nm, and this set consisted of four particle shapes. These shapes included spheres (S), heteronuclear dicolloids (hDC, with an aspect ratio of ~1.15), symmetric homonuclear dicolloids (sDC, with an aspect ratio of ~1.3), and tricolloids. The second set of particles consisted of spheres and symmetric homonuclear dicolloids (sDC, with an aspect ratio of ~1.17) with equivalent diameters between 1.0 and 1.3μm.

An experimental glass transition volume fraction (ϕ_g) was found using the linear response behavior from dynamic stress sweep experiments at a frequency of 1Hz. For interactions modeled as effectively hard, particle shape was found to profoundly influence the location of ϕ_g in the same manner as predicted by activated nMCT. Spheres have the lowest ϕ_g, with lower aspect ratio hDC or sDC having higher values of ϕ_g, larger aspect ratio sDC having a yet higher ϕ_g, and TC having the highest volume fraction transition to a glassy state. The linear response elastic modulus G_0' is found to have a similar effect as ϕ_g from changing particle shape. However collapse of all shapes is found when the effective volume fraction of each sample is scaled in terms of its distance from

a maximum packing fraction known as random closed packing (ϕ_{RCP}). For all shapes, $G_0' \sim \phi^{*4}$ where $\phi^* = 1/(\phi_{RCP} - \phi_{eff})$.

The effects of tuning particle interactions for S and sDC on the location of ϕ_g and G_0' were studied. At the lowest ionic strengths, particles are repulsive due to electrostatic charges on the surface. As ionic strength is increased, the electrostatic double layer is increasingly screened reducing the effective size of the particles. ϕ_g is seen to rise as ionic strength is initially increased. For smaller particles, at an ionic strength of 0.3M, the interaction between particles is weakly attractive and a maximum in ϕ_g is found for both spheres and sDC suspensions. Further increases in ionic strength lead to the formation of gels and the suspensions become nonergodic at lower volume fractions. The result is a reentrant state diagram with ϕ_g that is nonmonotonic with increasing ionic strength.

The yielding behavior of dense suspensions of these particles was also studied, first under conditions that result in effectively hard interactions for all four particle shapes and then under varying particle interactions for sphere and sDC suspensions. The external stress applied to samples of these suspensions is understood to lower the entropic barriers constraining the particle motion. For hard interactions, anisotropic shapes lead to multiple modes of stress relief as rotational motion becomes possible. Here, for hDC and sDC suspensions, two yielding events are seen. One event is from exceeding the entropic barrier associated with center-of-mass motion and the other from exceeding the barrier associated with rotational motion. The yielding behavior of TC also shows indications of multiple yield events, but the behavior is more difficult to explain. As ionic strength is increased, particles begin forming bonds that also constrains motion. Under conditions where spheres are weakly attractive, there is again evidence for two yielding events.

These events come from escaping barriers associated with cages of neighboring particles and with interparticle bonds. For dicolloids under weakly attractive conditions, two yield events are also observed. Here, rotational and translational motion likely becomes coupled and the two distinct events stem from breaking bonds and cages.

The shape dependence of the absolute yield stress of the suspensions, defined at the stress where $G'=G''$, can also be collapsed in a similar manner as G_0'. Again for hard interactions, by plotting yield stress as a function of ϕ^* the data collapses onto a single line with a slope of four. Other ionic strengths can also be collapsed in this manner by using an ionic strength dependent ϕ_{max} in place of $\phi_{RCP.}$ ϕ_{max} is found to lie between ϕ_g and ϕ_{RCP} and shows the same nonmonotonic behavior as ϕ_g.

Suspensions of larger particles show similar dynamic rheological behavior as the small particles with ϕ_g larger for dicolloid particles than spheres. ϕ_g again shows reentrant behavior with increasing ionic strength with the maximum in ϕ_g occurring at $5x10^{-3}$M for spheres and $3x10^{-3}$M for dicolloids. G_0' is also found to depend on ϕ^{*4} where $\phi=1/(\phi_{max}-\phi)$ and ϕ_{max} is dependent on ionic strength (with a reentrant-like behavior) and particle shape. The absolute dynamic yield stress is a strong function of volume fraction and again follows a similar trend as G_0' with respect to ϕ^*. Continuous stress experiments yield a critical stress for the onset of discontinuous shear thickening that is constant with respect to particle shape and interaction, and occurs at a dimensionless stress of approximately 10^4. The volume fraction where the dynamic yield stress and the stress at thickening intersect is predicted to lie just below ϕ_{max} indicating that the system may thicken before flowing (or yielding) and therefore be jammed even before ϕ_{max} is reached.

8.2 Future Studies

Future studies of interest to this work would be those that succeed in synthesizing additional particle shapes. For example, by creating dicolloid particle with aspect ratios greater than 1.4, one would be able to see if the nonmonotonic behavior predicted by nMCT is confirmed. Furthermore, the multi-step emulsion polymerization process used to create the particles from this work could be hypothetically be extended to create particles with greater than three protrusions. Although there was significant difficulty in creating reproducible tricolloid particles in this work, the single successful reaction suggests that it is indeed possible.

While the rheological behavior of anisotropic particle suspensions has been extensively covered in this thesis, the structure of the suspensions both at rest and under flow has seen only limited attention. Future work that explores the structure of these suspensions would add value information to their understanding. For example, neutron scattering experiments were attempted using the small particles discussed here, but the results were inconclusive and therefore not included in the thesis. Similar experiments could be repeated in hopes of more conclusive results or various characteristics of the suspensions could be altered to better conform to the constraints of other experiments that yield structural information. For example, by index matching the particles to the solvent light or x-ray scattering experiments could yield useful information depending on the size of the particles. Rheo-NMR also shows potential for use with these suspensions. Although the polystyrene particles had no distinguishable NMR signal when these experiments were attempted, the solvent may provide another material more suitable for NMR.

Appendix

$$\frac{u_{VDW}(x)}{kT} = -\frac{A}{12kT}\left\{\frac{1}{x^2+2x} + \frac{1}{x^2+2x+1} + 2\ln\left(\frac{x^2+2x}{x^2+2x+1}\right)\right\}$$

Equation A.1. Equation for van der Waals force contribution to pair interaction potential where A is the Hamaker coefficient for particles in a continuous phase, and $x = (r/D - 1)$, with r the center to center separation.

$$U_{elect} = \pi\varepsilon_0\varepsilon_1 D\psi^2 \ln\left(1 + e^{-\kappa r}\right)$$

Equation A.2. The electrostatic contribution to the pair interaction potential where Where ε_0 and ε_1 are the permittivity of free space and water, ψ is the surface potential, taken here to be the zeta potential, and κ is the Debye-Huckel parameter. The Debye-Huckel length, $1/\kappa$, describes the distance at which the surface potential has decreased to ψ/e.

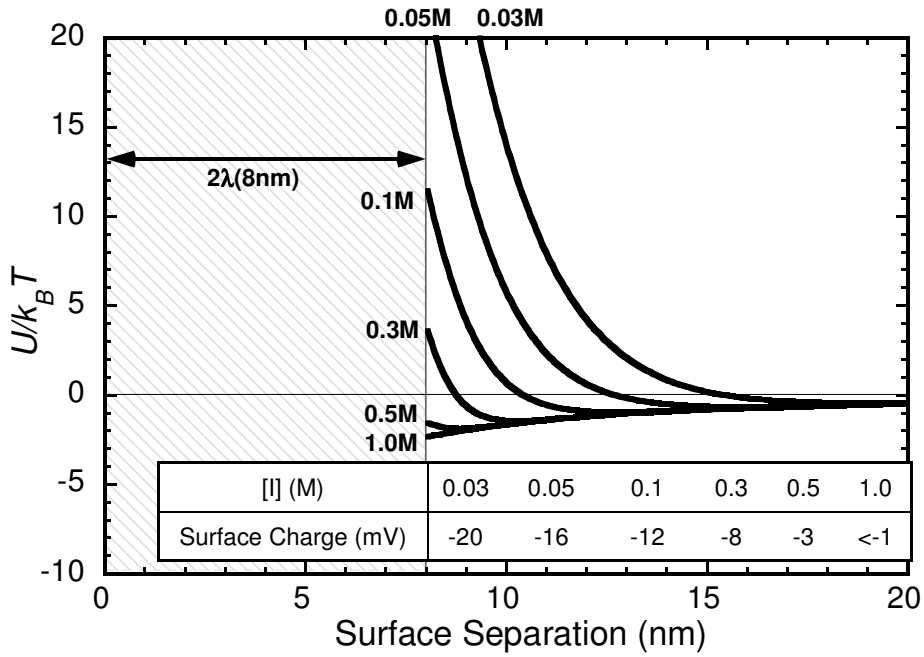

Figure A.1. Detailed interaction potential calculations for each ionic strength, including surface charge measurements from electrophoresis.

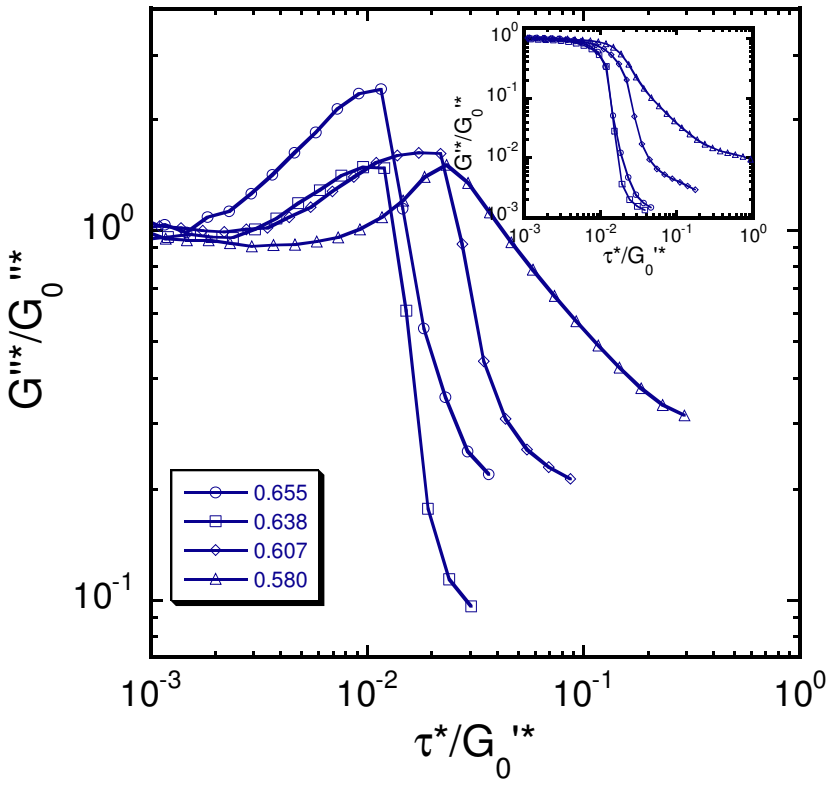

(a)

Figure A.2 (continued on next page)

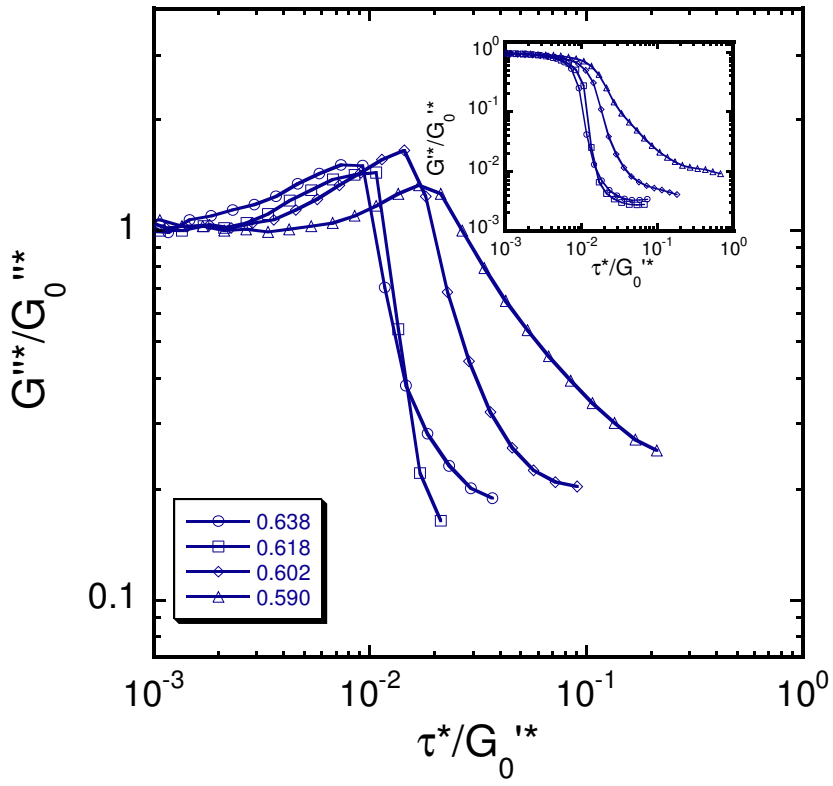

(b)

Figure A.2 (continued on next page)

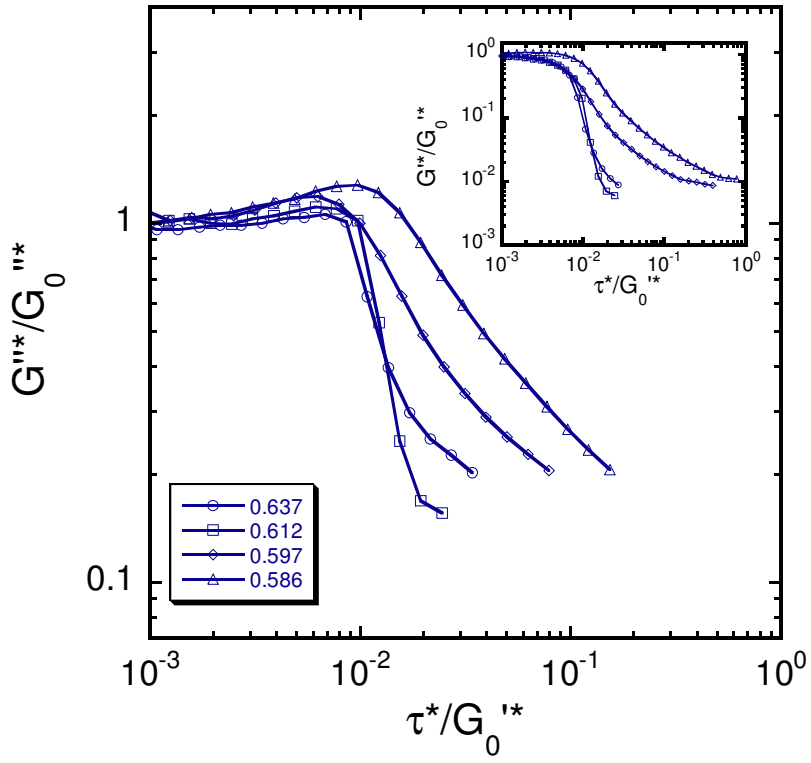

(c)

Figure A.2 (continued on next page)

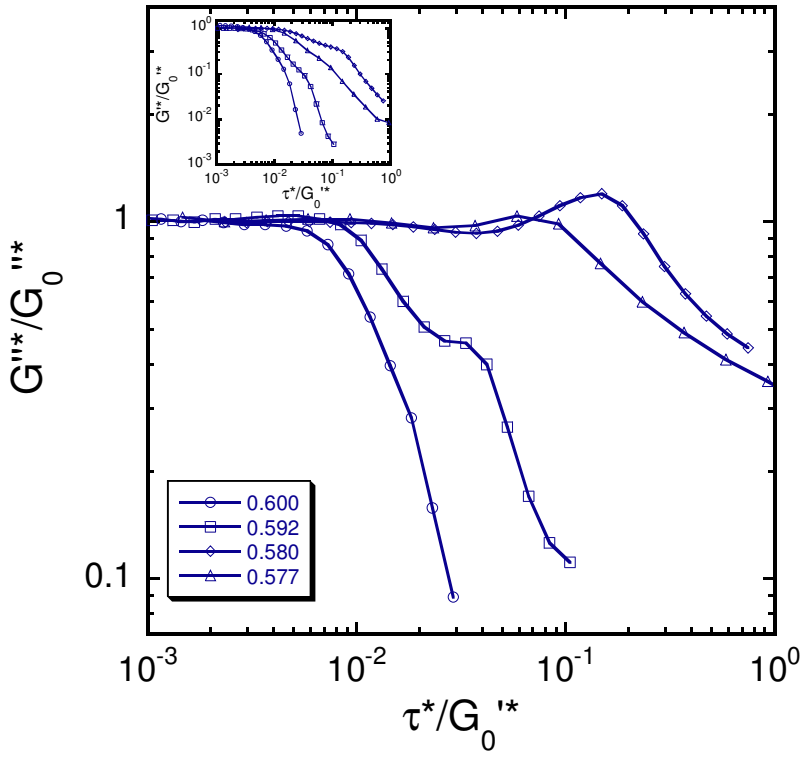

(d)

Figure A.2 (continued on next page)

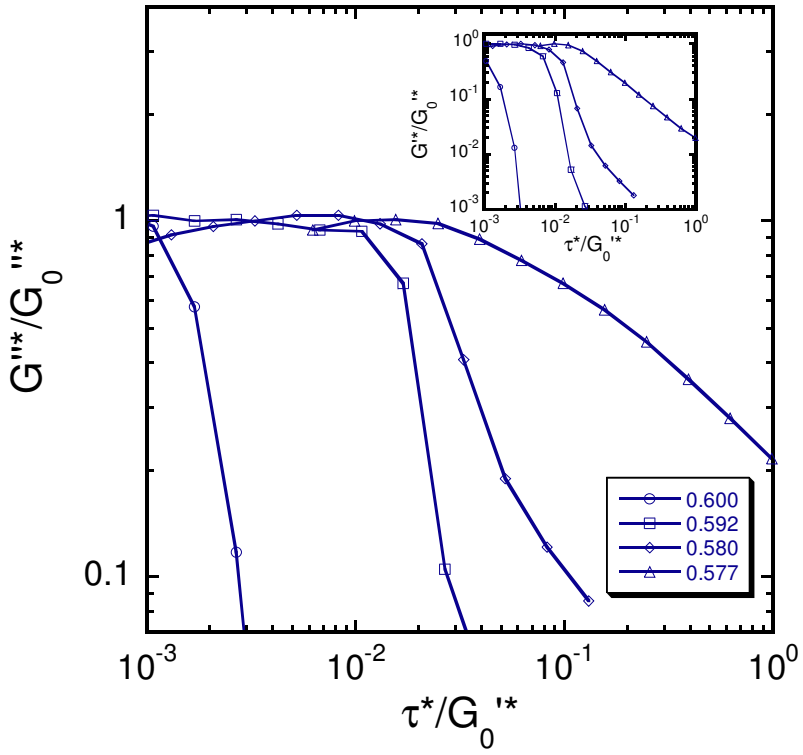

(e)

Figure A.2 (continued on next page)

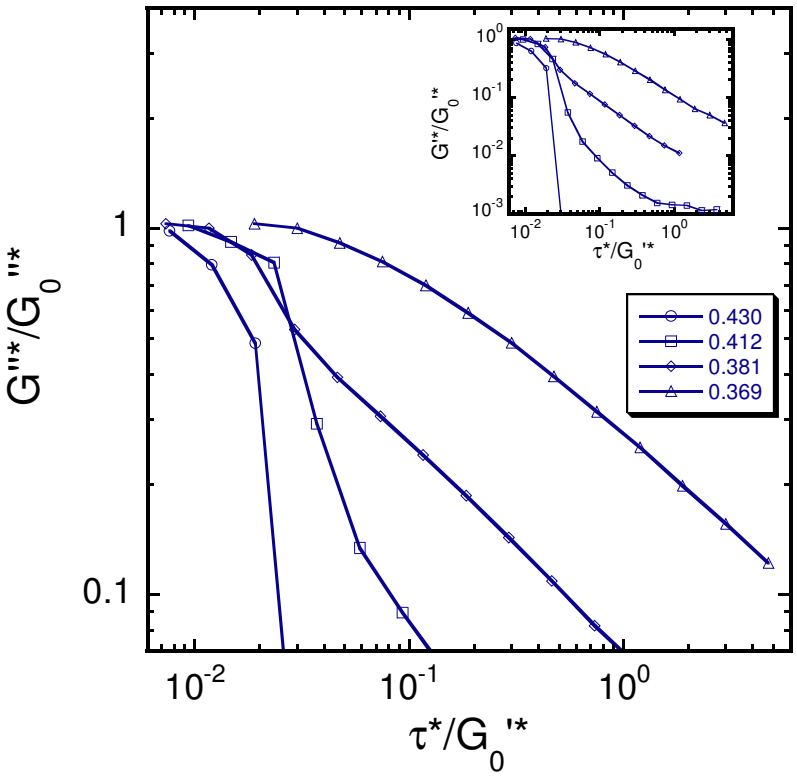

(f)

Figure A.2. Dynamic stress sweeps for four representative volume fractions for spheres at each ionic strength showing effects of changing volume fraction. *G"** (main panel) and *G'** (inset) have been scaled on the plateau values (G_0"*, G_0'*) and dimensionless stress τ^* has been scaled on the plateau value of G_0'*. Ionic strengths are 0.03M (a), 0.05M (b), 0.1M (c), 0.3M (d), 0.5M (e), and 1.0M (f).

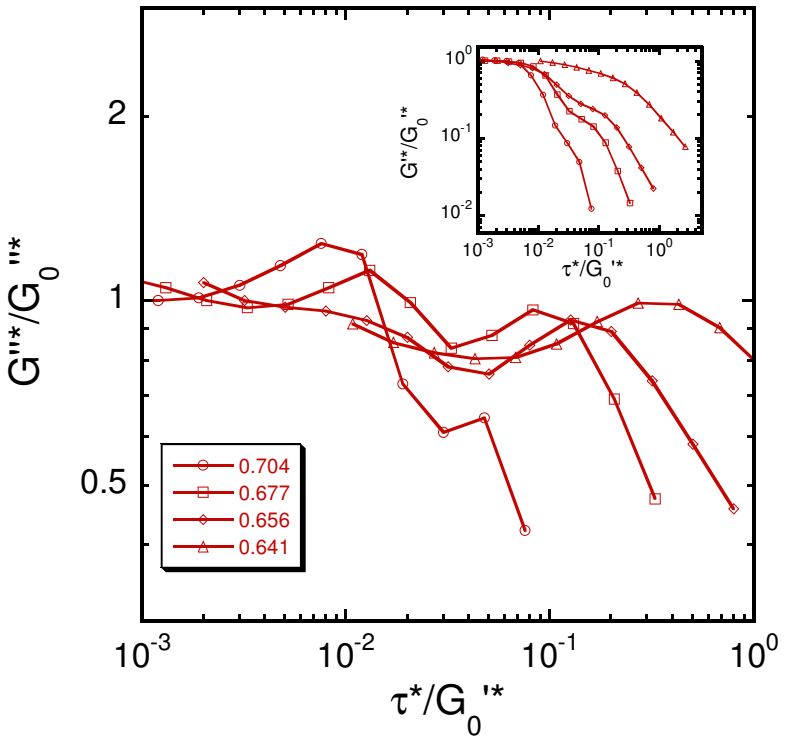

(a)

Figure A.3 (continued on next page)

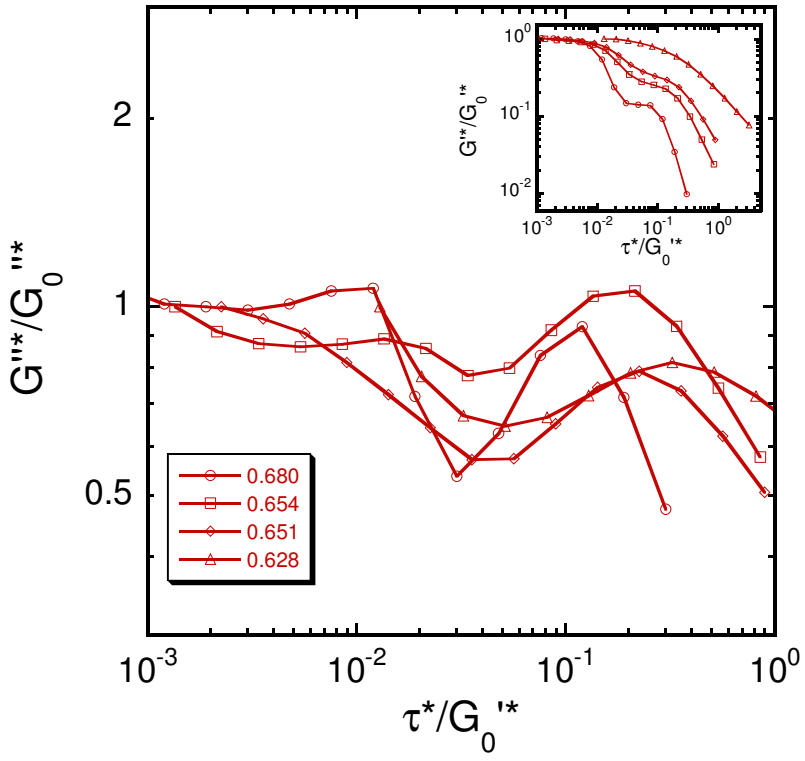

(b)

Figure A.3 (continued on next page)

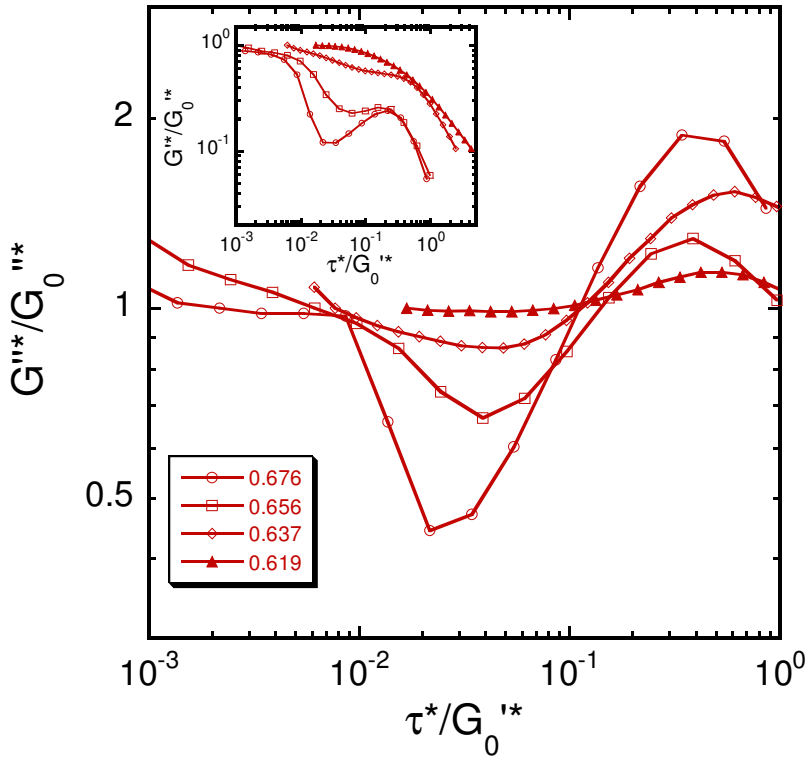

(c)

Figure A.3 (continued on next page)

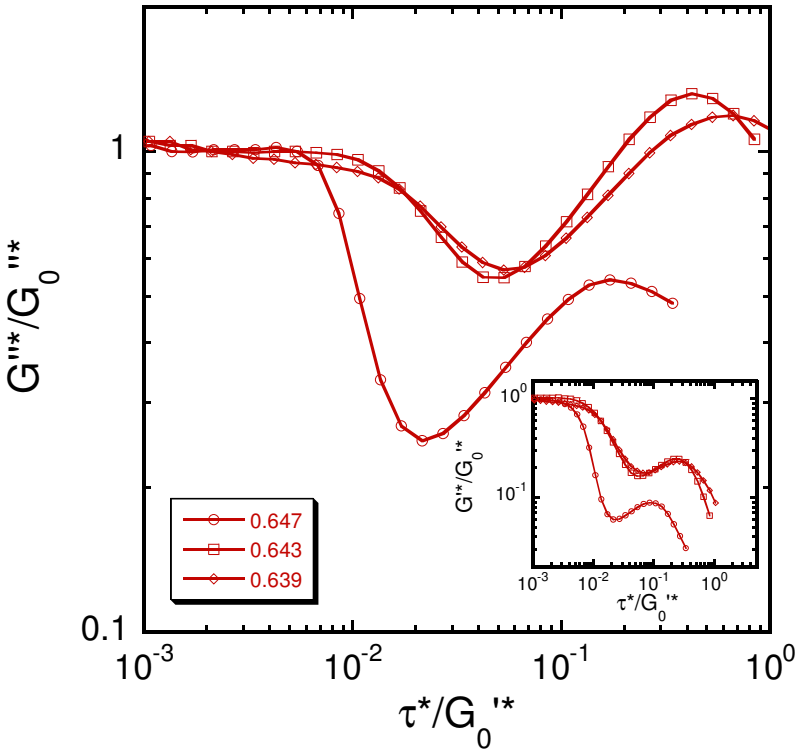

(d)

Figure A.3 (continued on next page)

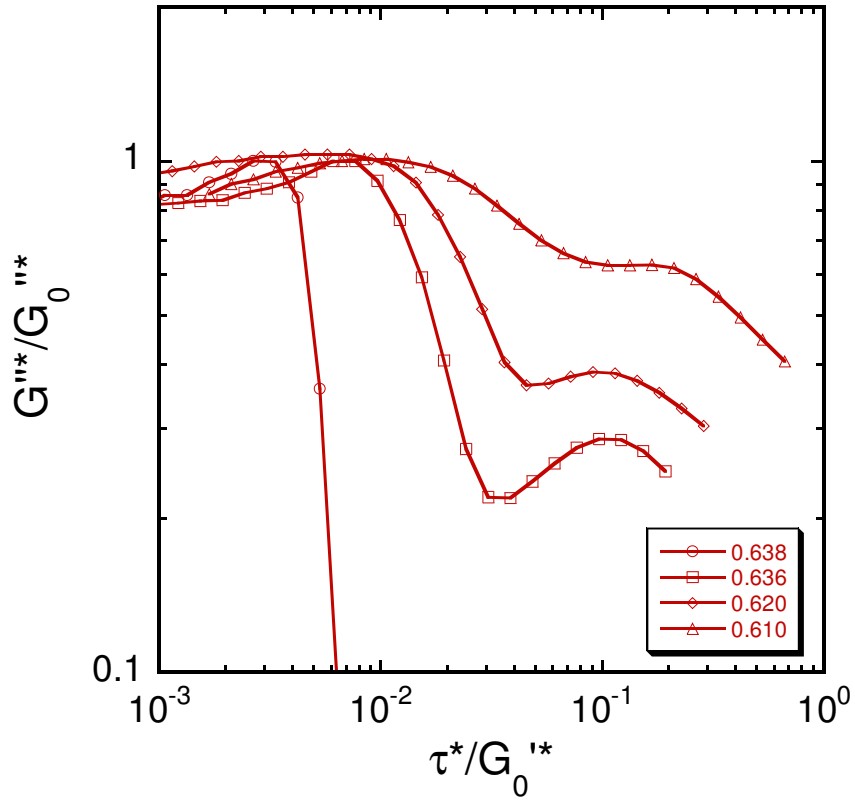

(e)

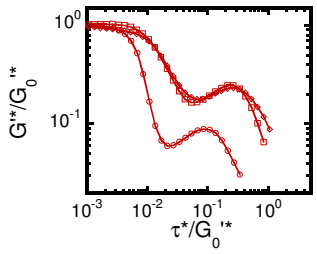

Figure A.3 (continued on next page)

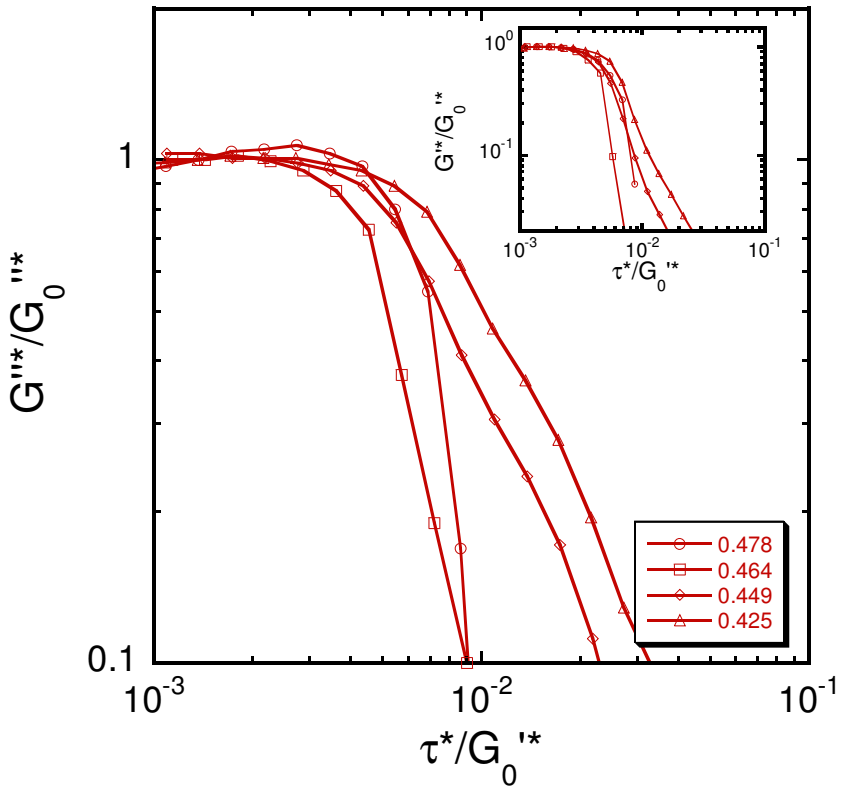

(f)

Figure A.3. Dynamic stress sweeps for four (or three) representative volume fractions for dicolloids at each ionic strength showing effects of changing volume fraction. *G"** (main panel) and *G'** (inset) have been scaled on the plateau values (G_0"*, G_0'*) and dimensionless stress τ^* has been scaled on the plateau value of G_0'*. Ionic strengths are 0.03M (a), 0.05M (b), 0.1M (c), 0.3M (d), 0.5M (e), and 1.0M (f). In panel (c), the only single yielding dicolloid sample is distinguished with solid points and (0.1M, ϕ_{eff}=0.619).